POLITECNICO
MILANO 1863

SCUOLA DI INGEGNERIA INDUSTRIALE
E DELL'INFORMAZIONE

Design and optimization of a point focus Beam-Down system

Tesi di Laurea Magistrale in
Energy Engineering - Ingegneria Energetica

Author: **Andrea Zanut**

Student ID: 10565992
Advisor: Prof. Andrea Giostri
Co-advisors: Prof. Marco Binotti
Academic Year: 2020-21

Abstract

In CSP applications, Beam-Down optics (BD) can play a major role in the future decarbonized energy scenario. The presence of a ground-mounted receiver avoids moving the working fluid from the tower up to the power block and therefore decreases the thermal and pumping losses. The thermal performances can be further boosted thanks to the installation of a tertiary concentrator, namely a Compund Parabolic Concentrator (CPC). The redirection of solar rays from the heliostat field toward the ground is guaranteed by the presence of a hyperbolic Secondary Reflector (SR).
The currently installed BD optic solar fields are made out of a circular surrounded pattern. This thesis aims at investigating the possibility of generating an asymmetrical solar field, so to exploit the most performing area of the site, in terms of cosine, at latitudes far from the equator. It was chosen to perform the analysis for a 50 MW_{th}, at receiver aperture, solar field at a latitude of 25 ° North. The generation of the heliostat field is of a radial staggered type and follows the procedure presented by Collado (code *campo*). Furthermore, it was shown that the most performing area of the solar site, in terms of cosine, is strongly influenced by the shadow of the hyperboloid and that the replacement of mirrors in that part of the field, with farther ones, less shaded, can increase the annual optical performance up to 3%.
On the other hand, the farther heliostat selection is strongly influenced by the geometry of the CPC, and therefore a matrix optimization method is presented, to maximize the annual optical-thermal performance of the system at different eccentricity values and aim point heights. The results are also assessed in terms of economic parameters and the best configuration was found for eccentricity equal to 3 and an aim point of 120 m. System annual efficiency is 59.49 % based on a clear sky DNI model, the product of 67.63 % optical and 87.96 % thermal efficiency, at receiver temperature of 750° C.
Moreover, a 1D thermal model is presented for different possible configurations of the SR. The cooling power required to maintain the temperature of the silver reflective surface at its limit value (65 °C) was found equal to 5.38 MW.

Keywords: CSP, Beam Down, Secondary reflector, Hyperboloid, Heliostats field, CPC

Abstract in lingua italiana

Negli impianti a CSP, specialmente le torri solari, l'ottica a Beam-Down può svolgere un ruolo importante nel futuro scenario energetico decarbonizzato. L'installazione del ricevitore a terra evita di movimentare il fluido di lavoro dalla torre fino al blocco di potenza, dimuinendo quindi, le perdite termiche e di pompaggio. Le prestazioni termiche possono essere ulteriormente incrementate grazie all'installazione, sopra al ricevitore, di un concentratore terziario, generalmente di tipo parabolico (CPC). Il reindirizzamento dei raggi solari dal campo di eliostati verso il suolo è garantito dalla presenza di un Riflettore Secondario (RS) iperbolico.

I campi solari a ottica BD attualmente installati sono costituiti da un campo circolare. Questa tesi ambisce a valutare la possibilità di generare un campo solare asimmetrico, così da sfruttare la zona di più performante del sito, in termini di coseno, a latitudini lontane dall'equatore. È stato scelto di performare l'analisi per un campo solare da 50 MW_{th} all'apertura del ricevitore, a 25° di latitudine Nord. La generazione del campo di eliostati è di tipo radiale sfalsato e segue la procedure presentata da Collado (codice *campo*). Inoltre, è stato dimostrato che la zona più performante del sito solare, in termini di coseno, è fortemente influenzata dall'ombra dell'iperboloide e che la sostituzione di specchi in quella parte di campo, con altri più lontani e meno ombreggiati, può incrementare le prestazioni annuali ottiche fino al 3%. La selezione degli eliostati più lontani è fortemente influenzata dalla geometria del CPC e quindi un metodo di ottimizzazione a matrici viene presentato, al fine di massimizzare le prestazioni annuali ottico-termiche del sistema a differenti valori di eccentricità e altezza del fuoco superiore. I risultati sono analizzati anche in termini di parametri economici e la configurazione migliore è stata trovata per eccentricità pari a 3 e fuoco superiore a 120 m. L'efficienza annuale del sistema è del 59.49% sulla base di un modello DNI a cielo sereno, prodotto del 67.63% di efficienza ottica e 87.96% termica, alla temperatura del ricevitore pari a 750 °C.

Inoltre, viene presentato un modello termico 1D per diverse possibili configurazioni del RS. La potenza di raffreddamento necessaria per mantenere la temperatura della superficie riflettente d'argento al suo valore limite (65 °C) è stata trovata pari a 5.38 MW.

Parole chiave: CSP, Beam Down, Riflettore secondario, Iperboloide, Eliostati, CPC

Contents

Introduction

The anthropogenic intensification of climate change, the need for energy security, and the depletion of fossil fuel reserves need an immediate global response.
Concentrating Solar Power (CSP) application can play an important role in the decarbonization of current thermal and electrical energy production.
The solar energy received by the worldwide desert regions within 6 hours is roughly estimated more than the energy consumed by humankind in a year. It's enough to cover the 1% of this area with solar thermal plants to satisfy the world annual power electric consumption.
In CSP applications, direct solar radiation is concentrated on a receiver in order to obtain high-temperature thermal energy that is generally utilized as a boiler for power generation cycles. With respect to direct electricity conversion technologies like wind and solar PV, CSP application favors high capacity factor guarantee by the presence of thermal energy storage. Moreover, the inter-hour operation management allows the possibility of providing ancillary services including voltage support, frequency response, and regulation.
The current installed worldwide CSP electric power is around 6 GW, consisting in a 0.2% share renewable energy market [1]. As presented by IEA, an annual averaged generation growth of 31% is needed from 2020 to 2030 to achieve Net Zero power generation, corresponding to around 6.7 GW of new capacity installed every year [20]. Actually, current high production and manufacturing costs are limiting the competitive advantage in the market in terms of Levelized Cost Of Electricity (LCOE), but an increase in the learning rate is expected to allow CSP to actively participate in the future decarbonized scenario.

This thesis aims at investigating a particular CSP optic, called Beam Down, where thanks to the installation of a secondary reflector, the solar radiation is redirected towards the ground. Heliostats field design has to take into account the derating efficiency caused by the secondary reflector shadow and reflectivity. So a solar field optimization will be proposed, aiming at increasing the annual system efficiencies.

0.1. CSP basic concept

Solar applications are continuously under the microscope of research. The main scope is looking for new technologies that guarantee high conversion efficiency of solar energy, that can be achieved utilizing higher receiver temperature (more than 1100 K) [43]. This goal can be reached only by increasing the concentration ratio of the solar field.
Let's consider a simplified optical analysis in which a collector of area A_c is facing a Direct Normal Irradiance (DNI). The radiation is then redirected towards a receiver of area A_{rec}.

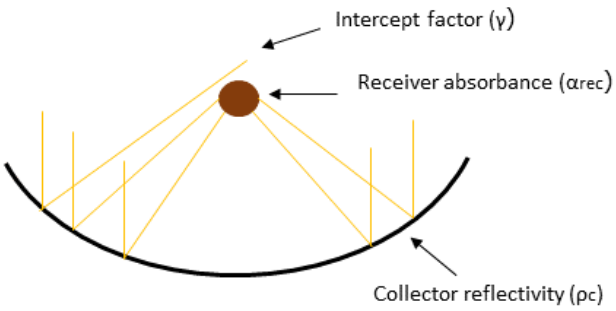

Figure 1: Simplified collector-absorber model.

Due to the cosine losses, the effective value of the sun radiation, DNI_{eff}, is lower.
The maximum power reflected by an ideal collector, $\dot{W}_{sun}$, can be expressed as Equation 1.

$$\dot{W}_{sun} = DNI_{eff} \cdot A_c \tag{1}$$

On the other hand, the final useful effect has to take into account various losses happening on the energy path from the sun source to the collector.
Not all the rays will be reflected towards the receiver due to reflectivity and intercept losses. The percentage of reflection is governed by the reflectivity ρ_c.
The intercept factor points out that not all the ray pointing the collector, considering optical error, will be captured due to finite receiver surface. Let's identify it with the letter γ.

$$\gamma = \frac{\int_{-D/2}^{D/2} \rho_c \cdot DNI_{eff}\ dx}{\int_{-\infty}^{\infty} \cdot DNI_{eff}\ dx} \tag{2}$$

Where D is the receiver diameter and ρ_c the reflectivity of the collector. Moreover, the receiver won't behave as a perfect black body ($\alpha_{rec}<1$), so not all the incident radiation

is absorbed.
The receiver at T_{rec} is facing the ambient temperature and a mechanism of radiative and convective heat transfer takes place. Let's simplify the system by considering a universal heat transfer coefficient U that takes into account both dissipating mechanism. The net heat absorbed $\dot{W}_u$ can be evaluated as Equation 3.

$$\dot{W}_u = \rho_c \cdot \alpha_{rec} \cdot \gamma \cdot DNI_{eff} \cdot A_c - U \cdot (T_{rec} - T_{amb}) \cdot A_{rec} \tag{3}$$

The optical-thermal efficiency η_{rec} can be then calculated as Equation 4.

$$\eta_{rec} = \frac{\dot{W}_u}{\dot{W}_{sun}} = \rho_c \cdot \alpha_{rec} \cdot \gamma \cdot -\frac{U \cdot (T_{rec} - T_{amb})}{DNI_{eff} \cdot \frac{A_c}{A_{rec}}} \tag{4}$$

The ratio A_c/A_{rec} is called concentration ratio and the higher it is, the lower thermal losses will be and so the higher the sun energy conversion. Moreover, a higher concentration ratio allows also to higher receiver temperature and so higher cycle efficiency.
The overall system efficiency can then be performed by multiplying the optic-thermal efficiency (η_{rec}) per the one of a thermodynamic cycle. By simplifying the concept, a Carnot cycle can be considered, whose efficiency can be evaluated as Equation 5.

$$\eta_{Carnot} = 1 - \frac{T_{amb}}{T_{abs}} \tag{5}$$

So the overall system efficiency is performed as $\eta_{sys} = \eta_{rec} \cdot \eta_{Carnot}$.
As shown Figure 2, it exists a receiver temperature that maximizes the overall system performance, for each value of concentration ratio and optical receiver properties.
For medium values of concentration ratio (CR=100), a low value of emissivity is needed to ensure high system efficiency at receiver temperature over 800K.
By pushing the concentration ratio up to 1000 and the absorber material emissivity close to zero, the thermal loss becomes negligible and the overall system efficiency follows the Carnot efficiency trend.
When the optical energy reaching the receivers equals the thermal loss, η_{rec} is null. In that condition, the receiver temperature reaches its maximum temperature, called stagnation temperature.

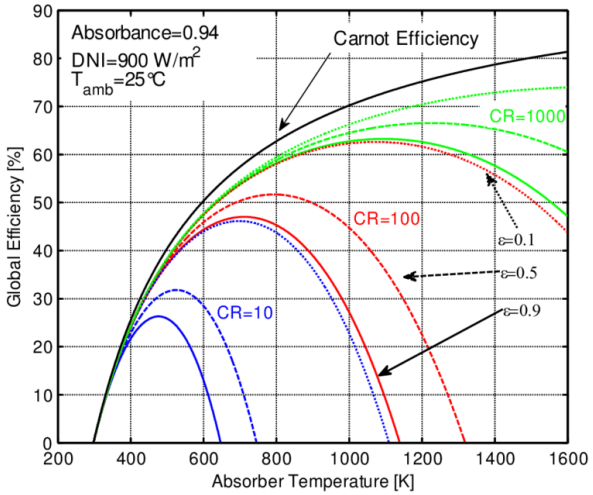

Figure 2: Overall system efficiency plot at different sola field concentration ratio and absorber emissivity values (ε) [19].

On the solar field application, point-focus concentrator are the ones that guarantee the highest concentration ratio. In this category, solar tower systems are the main character.

0.2. Beam down optic

The optic of a beam down system has been firstly introduced by Rabl et al. [47] and further investigated by various scientist. The system is composed mainly of the heliostat field, a secondary reflector, a possible tertiary reflector, and a receiver.
Two different foci characterize the system optic, an upper one which coincides with the aim point of the heliostat field, and a lower one that corresponds to the entrance of the tertiary concentrator, generally, a Compound Parabolic Concentrator (CPC), if present or directly with the receiver aperture, as shown in Figure 3.
A surface that can direct the heliostat reflected radiation into a single point, ideally, is of a Cartesian type. It's composed by two foci and it's generally represented by Equation 6.

$$z = f(x,y) = \frac{(x^2+y^2)/R}{1+[1-(1+k)(x^2+y^2)/R^2]^{1/2}} \tag{6}$$

Where R is the vertex curvature radius of the surface and k is the conic constant. When $k<1$ the equation speaks for a hyperboloid surface of two sheets [47]. The two foci correspond to the upper and lower focus of the solar system.

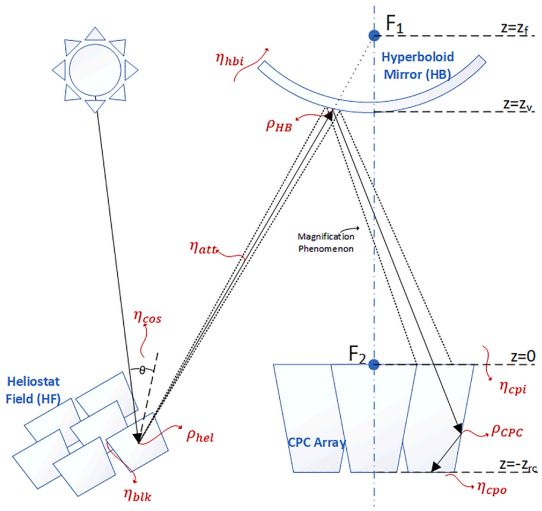

Figure 3: Beam down optic scheme [39].

Two different quadratic surfaces are possible: a hyperboloid or an ellipsoid. As shown in Figure 4, the hyperbolic shape guarantees a convex SR placed below the upper focus, while the elliptical one is concave and installed beyond the aim point and so requires a higher tower.

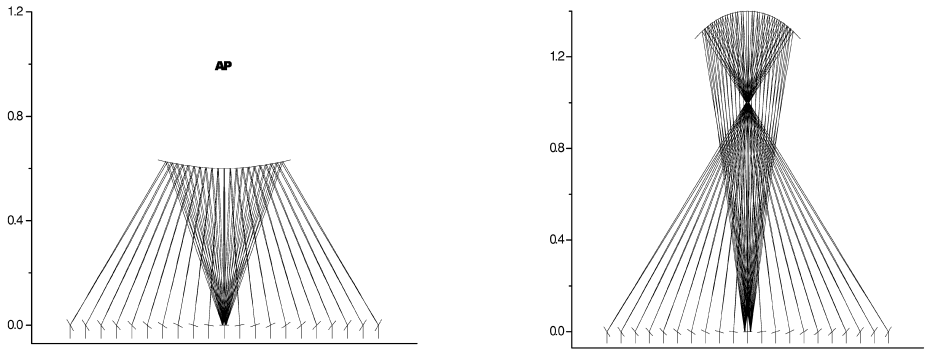

(a) Hyperbolic shape (b) Elliptical shape

Figure 4: Secondary reflector possible geometries [43].

The hyperbolic shape has been identified as the best trade-off between performance and tower cost. Segal and Eipstein found that the elliptical shape requires twice as much as the installation height and larger radius due to optical error amplification caused by higher optical path [43].

The main advantage of the beam down optic is the cost reduction generated by the installation of the receiver at ground level. Lower pumping losses affect the system and the

tower cost is diminished [16]. Moreover, a tertiary concentrator can be easily installed to make a uniform distributed receiver image and further reduce the thermal losses. Generally, a Compound Parabolic Concentrator (CPC) is utilized. It's a particular geometry composed of two parabolas. Precisely, the focal point of one parabola A lies on the end of the parabola B, as shown in Figure 5.

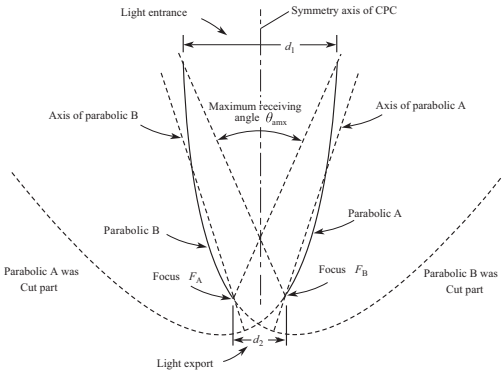

Figure 5: Geometry of CPC solar concentrator [52].

Moreover, the angle created by the longitudinal axis and the connection line of the tip of one parabola to the end of the other set the maximum incidence angle. Values higher than the latter one, will be reflected back and not collected by the receiver.
The lower is the maximum incidence angle, the higher will by its concentration ratio, the CPC is leaner but with sensible increased height. To limit the CPC longitudinal extension, the latter can be placed in array configuration as shown in Figure 3. Moreover, the shape can be circular or polygonal, based on techno-economical considerations.

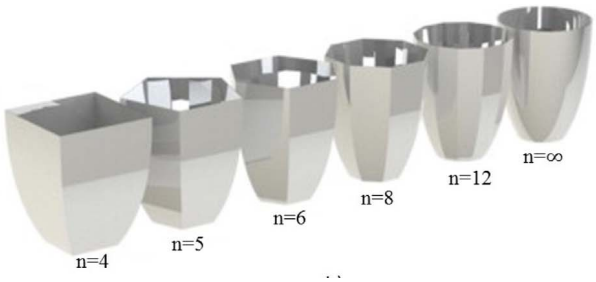

Figure 6: Possible CPC shape. n represents the number of faces [45].

On the other hand, the increased losses and maintenance costs caused by the presence of a secondary reflector can lower the performance and increase the LCOE of the system. Moreover, the hyperboloid affects negatively the heliostat field due to the shading effect and introduces another loss related to the absorbed or transmitted power due to nonideal mirror reflectivity properties.

0.3. Demonstration plant

Despite the difficulties encountered in designing beam down systems, the topic is getting a lot of interest in the research field and it will be expected that the technology will be commercialized in the coming few years [16].
Current installations are present in Japan, Israel, United Arab Emirates, China, and Italy and will be here presented briefly.

Solar site	**Miyazaki**	**Weizmann**	**Masdar**	**Magaldi**	**Yumen**
Thermal design power	113 kWth	650 kWth	100 kWth	2 MWth	17 MWth
Heliostat field type	Semi-surrounded	Polar	Surrounded	Surrounded	Surrounded
Heliostat number	88	64	33	786	2603
Mirror shape	10 Circular	Rectangular	Rectangular	Rectangular	Rectangular
Mirror dimension	D = 0.5 m each	7x8 m	3.21x2.64	-	-
SR type	Ellipsoid	Hyperboloid	Hyperboloid	Hyperboloid	Hyperboloid
SR height	14 m	45	16	-	60

Table 1: Beam-Down demonstration plants main parameters.

University of Miyazaki, Japan

The beam down facility was built by the University of Miyazaki and Mitaka Kohki CO. Ltd. as an R&D joint project for studying the feasibility of scaling up fluidized bed reactor with solar system. The system occupies a land of dimension 60x60 m and it is composed of 88 heliostats positioned at ground level and a 16 m central tower. Each mirror is composed of 10 units of 50 cm in diameter each. The upper focal point is positioned at 14 m while the lower one is at 10 m above the ground.
The system is able to concentrate on a 1.3x1.3 m CPC aperture, 113 kW_{th} at solar noon on the 12 October with a DNI close to 900 W/m^2 [23].

Figure 7: Beam down solar field at University of Miyazaki [23].

Weizmann Institute of Science, Israel

The solar tower system was built in 1988 at the Weizmann Institute of Science. It's composed of a tower of 56 m, 64 heliostats, and 54 m^2 of mirror reflective surface. The field is North-oriented and on the tower, there are installed 5 experimental levels. Bi-axial heliostat tracking system can reflect the lights to any of these testing stations.
The prototype was built mainly for research in thermo-chemical conversion fields, like methane cracking, hydrogen production, pressurized air heating for Brayton bottom cycle, and others, but overall solar driven.
At the beginning of 1999, a secondary reflector was built on one of the 5 testing spots. A hyperboloid shape of 75 m^2 was chosen and a ground CPC with 2.2 m diameter aperture and 5 m height capable of concentrating the incoming radiation by a factor of 25. The design thermal power was accounted as 650 kW with an overall field concentration ratio of 4000 [42].

Figure 8: Beam down solar field at Weizmann Institute of Science [42].

Masdar Institute, United Arab Emirates

The system, called Masdar Institute Solar Platform (MISP), was built in 2009 for R&D purposes in solar tower systems and thermal energy storage.
The beam technology includes 33 ganged-type heliostats of about 8.5 m^2 size. The mirrors are positioned in 3 equal circular sectors surrounding the tower and each of them is formed by 43 facets arranged in three banks.
The secondary reflector is installed at 16 m height on 3 pylons of 20 m height and composed of 45 mirrors disposed of in three multi-faceted rings. Each ring is related to a field row of heliostats.
The solar site is composed of an oil receiver at ground level, capable of reaching a maximum temperature of 393 °C to avoid degradation and a design power output of 100 kW. Furthermore, a Final Optical Element (FOE) was designed in order to increase efficiency by reducing the receiver aperture. It was proved that a conical FOE performed better than

a CPC and it also guarantee easy manufacturing. The prototype has an inlet diameter of 1.6 m, an outer one of 0.894 m and a 1.85 m height [10].

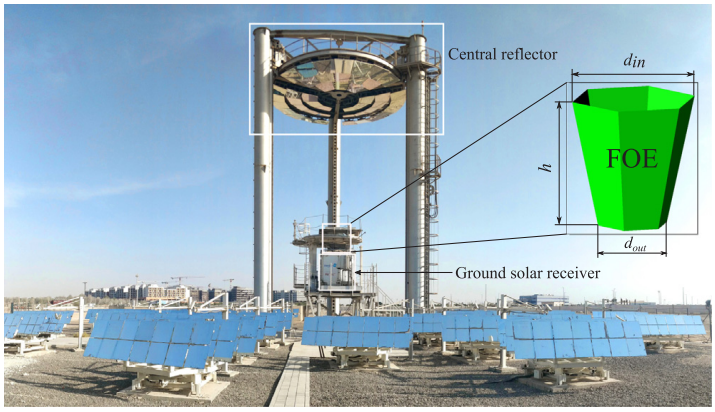

Figure 9: Beam down solar field at Masdar Institute [16].

Solar Thermo-Electric Magaldi, Italia

STEM-CSP is an innovative commercial product developed by Magaldi group. It's composed of a heliostats field, a secondary reflector, an integrated solar receiver, and a fluidizing air system.
The receiver is of a volumetric fluidized bed type able to let the storage up to 80 MWh of thermal energy in a range of 350 to 620 °C [31].
The first installation was made in San Filippo del Mela (ME), with the collaboration of A2A company. The solar system capacity is 2 MW_{th} thanks to 786 heliostats and 2 field hectares, capable of storing 550 kWh_e or a daily produce 20.5 tons of steam.
The system behaves like a battery and can store energy up to 8 hours [29].

Figure 10: Magaldi beam down solar field [31].

Yumen Xinneng, China

Yumen Xinneng 50 MW plant, signed in September 2016, is the world large-scale commercial beam down CSP project in the world. The capital cost of the project is valued at 75 million € with a payback time of 15 years.
The system is made of 15 mirror field modules, with a total of 624,720 m^2 reflective area and two tank 9-hour molten salt thermal system, reaching a maximum temperature of 570 °C [36]. Each field module can produce up to 17 MW_{th}. The hyperboloid shape was selected as a secondary reflector and its radius is around 60 m [15].

Figure 11: Yumen Xinneng beam down solar project [15].

0.4. Particle receiver

The particle receiver pathway has been identified by the National Renewable Energy Laboratory (NREL) as one of the most promising solutions for the next generation Concentrated Solar Power (CSP) application, namely Gen3 pathways [33]. Figure 12 summarized the technology upgrade, generation by generation, of solar tower CSP plants.
Different receiver configurations are possible that can be either down-flow, up-flow and horizontal flow types. The main design challenges are guaranteeing enough particles residence time and boosting the heat transfer performances [21].
The Heat Transfer Fluid (HTF) can be either enclosed or fluidized in tubes or directly facing the incoming radiation. The first particle receiver type introduces additional heat transfer resistance from irradiated walls to particles and moreover, if the mass flow and cooling system are not properly maintained may cause failure or deterioration. On the other hand, the main challenge on direct particle receivers is to reduce the convective and radiative losses and effective particles heat exchangers for possible bottoming power cycle. Suitable particles heat exchangers are still under investigation. Grains cause exponential erosion effect on the heat-transfer tubes based on grains velocity.

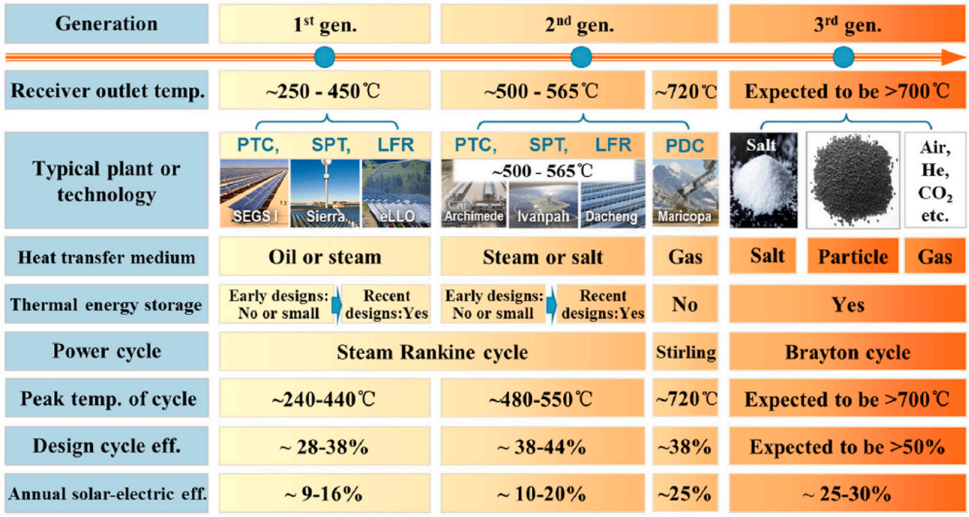

Figure 12: Solar CSP generation receiver temperature and technology [34].

Xie et al. proposed a novel downflow configuration in which particles flow is gravity-driven on an inclined plane, as shown in Figure 13. The residence time is controlled by a pneumatic control valve at the end of the inclined plate. The experimental shows that with a total incidence power of 8 kW and a particle mass flow rate of 7.5 g/s, the outlet temperature reaches 938 K. These performances are in line with the CSP Gen3 targets, and this type of configuration is well suited for beam down system. The receiver can be placed below the CPC and the hot particles directly stored in a silo.

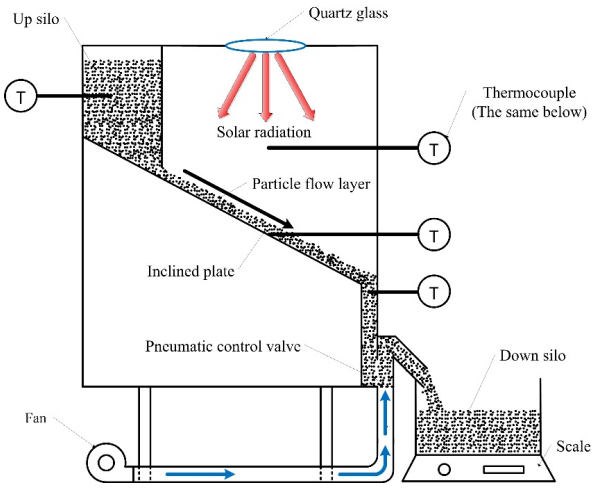

Figure 13: Promising down-flow particle receiver technology for beam down application [49].

Nevertheless, is difficult to analytically model the down-flow movement of particles. In a quasi-static regime, they can be patterned as using the soil plasticity model since the grain inertia is negligible. In a highly agitated regime particles act as a gaseous phase. In between the two regimes, the dense particles flow can be modeled as a liquid and the Bagnold avalanche theory holds [11].
A variety of particles material have been investigated by researchers where ceramic and silica-based ones are identified as the current most suitable solution due to high durability, high absorptance, and low cost.
On the other hand, particles receiver technology can sensibly increase the operational cost of the system due to material losses caused by wind gusts. Recent studies on a 100 MW_e CSP system measured a 0.01% rate of mass loss that requires a 10% inventory replacement every two years at a cost of around 1 million dollar [33].

1 | Methodology

This work aims to create a suitable Matlab program to design a generic Beam Down (BM) solar power plant at a specific latitude location.
Firstly, an ideal optical model is built considering randomly generated light points at ground level. The secondary reflector geometric properties like radius, area, and installation height at different eccentricities are presented. Furthermore, a real optic model is introduced and the error amplification eccentricity dependency is assessed.
In the second part, a novel 50 MW_{th} solar field creation program is presented. Following the field parameters and specifications utilized in designing solar power plants.
Subsequently, an optimization model is created to enhance the field performance considering the sensibly derating efficiency caused by the annual secondary reflector shadow. The best configurations found are analyzed also in terms of economic parameters.
In the third chapter, a 1D thermal model is constructed in order to assess the silver reflective surface temperature on the secondary reflector surface and find possible configurations to keep it under its maximum values.

Beam down optic

In this chapter, a secondary reflector of hyperboloid shape is considered due to better optical performance concerning the ellipsoid one. A randomly generated light point distribution is created and all the equations regarding the aiming direction, the reflection, and the ground receiver intersection are explained for an ideal optic model.
All the results are presented considering dimensionless, with respect to the aim point, quantities.
The concept of secondary reflector eccentricity is introduced to distinguish a specific hyperboloid shape among the infinite ones and the geometric quantities like SR radius, area, and installation height are presented.
Afterward, the Compound Parabolic Concentrator (CPC) geometry is presented aiming at boosting the field thermal performances. The concentration ratio and the inlet acceptance angles are assessed at different eccentricities and field radii considering a 2D ideal optic.

Subsequently, a bivariate normal distributed real optic model is considered in order to take into account sun, shape and slope errors. The aiming direction of each random light point is then disturbed and the error amplification effect is assessed at different eccentricities. The overall methodology is resumed in Figure 1.1.

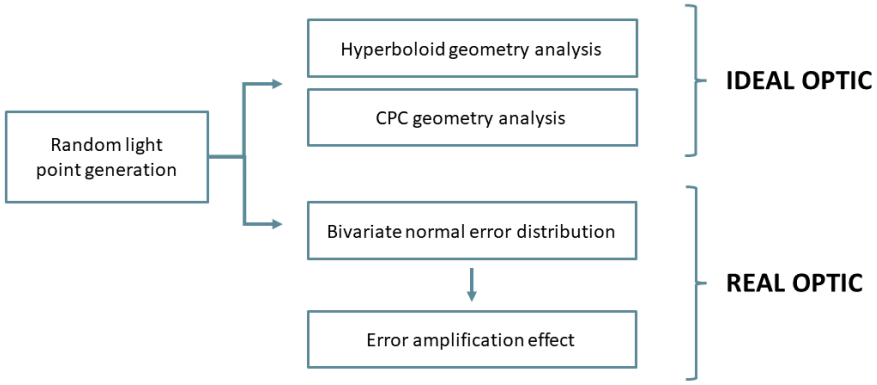

Figure 1.1: Flow chart of the Beam Down optic chapter.

Heliostat field creation

Beam down solar fields has been always built following a surrounded circular configuration. This thesis aimed to assess the possibility of asymmetric heliostats field pattern at latitude far from the equator to favor of better cosine effect.
So, a Matlab program was built starting from a radial staggered heliostats layout bounded between a minimum and maximum field radius. Furthermore, the shadowing and blocking performance were evaluated following the Sassi method. The intercept factor was assessed considering a randomly generated light point on the heliostats surface and optical errors. To unconstrain the hyperboloid shape from the normal circular model, the solar field was divided into sections of equal azimuth extension, so a sliced SR shape is created.
In BD optic, concerning solar tower, two other derating factors take place, namely the hyperboloid reflectivity and its shadow effect. The first one is pretty straightforward, just a few percent of the solar field radiation approaching the secondary reflector is reflected towards the receiver. The second one was evaluated by generating a random point light distribution on the free heliostats surface (neither shadowed nor blocked) and intersecting them with the SR with the direction given by the sun vector. The number of rays that don't cross the hyperboloid surface defines the SR shadow efficiency.
Results showed that the SR shadow effect is non-negligible, especially in the best cosine part of the field and at high eccentricity. So, an optimization model was built. Worst annual performing heliostats are deleted in favor of farther less shadowed ones.

Nevertheless, the selection of farther heliostats is limited by the CPC shape due to lower intercept performances. So, starting from a circular heliostats design, the first value of both the inlet radius and concentration ratio of the CPC is found and utilized as a first guess for the optimization procedure. An iterative process was built, varying both CPC parameters at a given eccentricity to find the best configuration possible.
Finally a techno-economic analysis is performed on the optimal fields found at different eccentricities and aim point height in order to find the best configuration in terms of minimum Levelized Cost Of Heat (LCOH). The overall methodology is resumed in Figure 1.2.

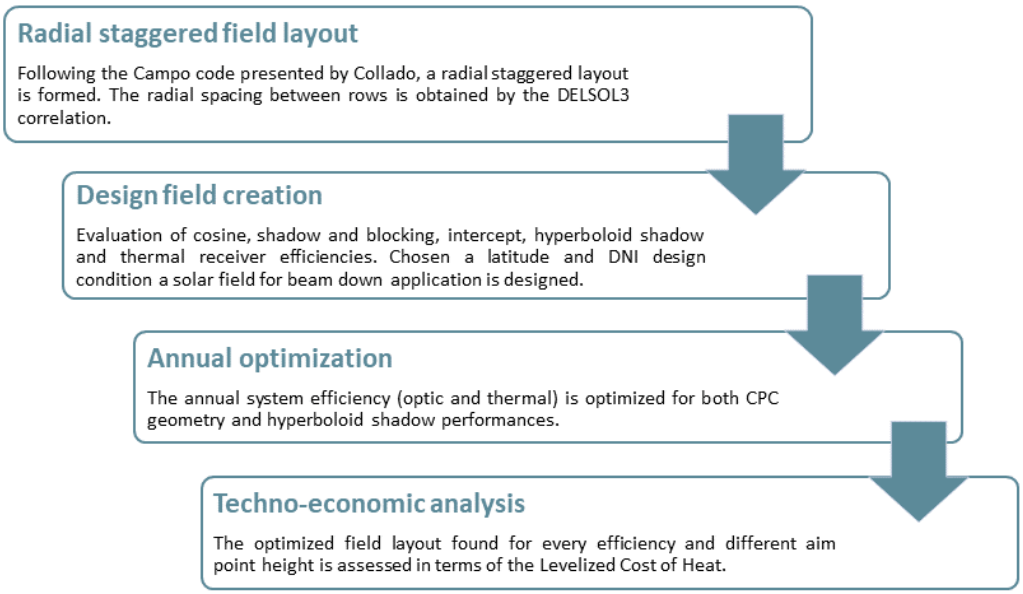

Figure 1.2: Flow chart of the Heliostats field creation chapter.

SR thermal model

In this chapter, a 1D thermal model of the hyperboloid was built to assess the temperature distribution on the SR. Different configurations were considered, like a sandwich, finned, not finned, and dry cooled one. In the first one, both hyperboloid surfaces are made out of a silver surface and a glass cover. In the second one, the upward-facing surface is substituted by an aluminum fin installed on the same material support. The last one considers the possibility of withdrawing a heat contribution from the upward-facing surface in the metal configuration without fin to limit the silver temperature.
In all cases, radiative, convective, and conductive heat is deeply analyzed and the silver temperature, namely the bottleneck one, is evaluated at different wind velocities.

2 | Beam Down optic

In this chapter, a simplified beam down model is presented where point light sources randomly distributed on the field are considered as energy sources. The objective is to introduce a simplified theory for a point-focus Beam-Down system both in term of ideal and real optic behaviour.
Starting from an ideal optic the geometry of the secondary reflector is analyzed in terms of radius and area variation at different eccentricities. Subsequently, optic errors are considered and the error amplification effect is assessed at different eccentricities.
To generalize the analysis all the calculus and results that will be shown are adimensionalized by the aim point length.

2.1. Secondary reflector geometry

The secondary reflector is the main character in a beam-down configuration. As presented before, a surface that can reflect a bunch of rays pointing an upper focus toward a lower focus is of a Cartesian type, precisely in this work, a hyperboloid. In order to do so, the two solar field foci correspond to one of the surface.
The secondary reflector considered in this work is of hyperbolic shape due to better optic performances concerning the elliptical one. It's generally expressed by the simplified canonic form in Equation 2.1.

$$\frac{x^2}{a^2} + \frac{y^2}{b^2} - \frac{z^2}{c^2} = -1 \tag{2.1}$$

If $a = b$ the surface is a hyperboloid of revolution. The surface defined by Equation 2.1 is called also two-sheet hyperboloid since the surface is convex.
Considering a two-sheet hyperboloid, an important parameter utilized in a beam-down system to identify one specific surface among the infinite ones is the eccentricity, defined as Equation 2.2.

$$e = \frac{FocDist/2 + c}{FocDist} \tag{2.2}$$

Where $FocDist$ is the distance between the upper and the lower focus and c is the semi-minor axis, as shown in Figure 2.1.

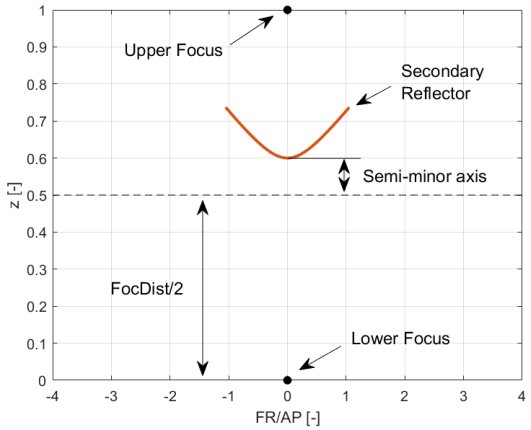

Figure 2.1: 2D representation of geometry parameters for a hyperbolic secondary reflector. FR is the Field Radius and AP the Aim Point height.

The value of eccentricity for a two-sheet hyperboloid is always greater than one. As the eccentricity increases, as shown in Figure 2.2, the hyperboloid becomes more squeezed to half of the focal distance, and its radius increase to catch the same amount of ray lights coming for the ground.

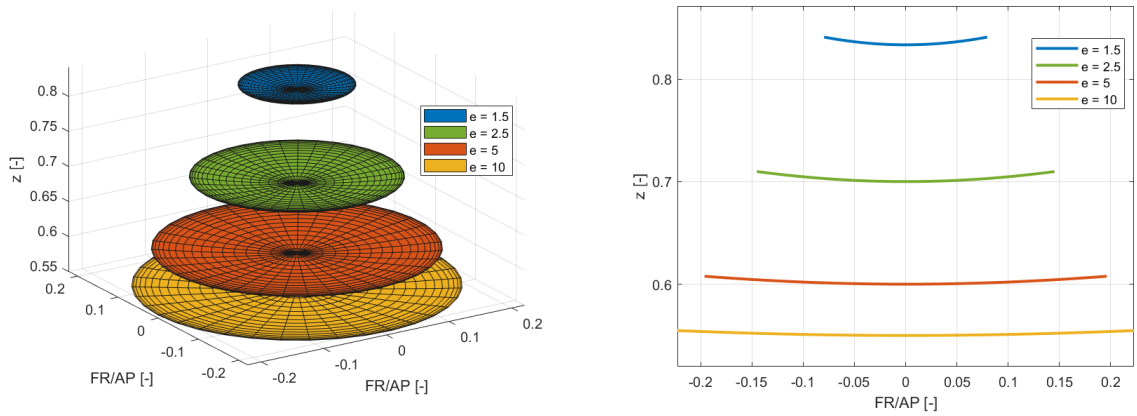

Figure 2.2: 3D (left) and 2D (right) representation of hyperboloid at different eccentricity. The surface radius is defined by an ideal optic, considering Field Radius (FR) over Aim Point (AP) equal to 0.5, upper focus at z = 1 and lower at z = 0.

2.2. Random light point distribution

In this preliminary analysis, the solar field is made by randomly distributed light point sources along a circular field radius. The polar coordinates of a random i-ray origin in a circle are created following Equation 2.3.

$$r_i = R \cdot \sqrt{rand}, \qquad \theta_i = rand \cdot 2\pi \tag{2.3}$$

Where R is the dimensionless (by the aim point) field radius and $rand$ is a normally distributed random number between 0 and 1. The polar coordinates are then translated into Cartesian ones and a random light point sources distribution is created, as shown in Figure 2.3.

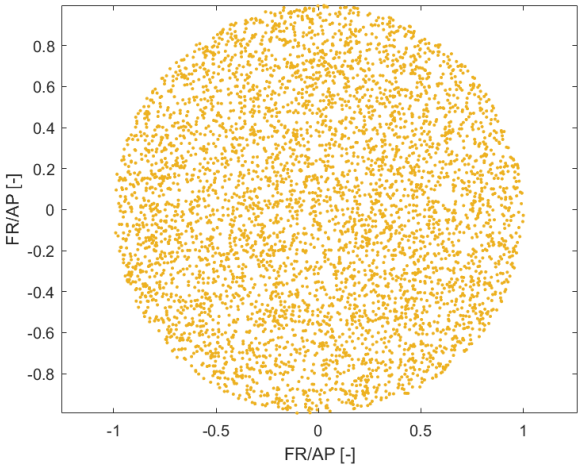

Figure 2.3: Circular random point distribution for Field Radius (FR) over Aim Point (AP) equal to 1.

2.3. Ideal optic model

The generic position of a point belonging to the i-ray, $[x_i, y_i, z_i]$, can be evaluated with the ray origin position $[x_{ray,i}, y_{ray,i}, z_{ray,i}]$ and a direction pointing towards the upper focal point defined by $[u^a_{x,i}, u^a_{y,i}, u^a_{z,i}]$.

$$x_i = x_{ray,i} + k \cdot u^a_{x,i}; \quad y_i = y_{ray,i} + k \cdot u^a_{y,i}; \quad z = z_{ray,i} + k \cdot u^a_{z,i} \tag{2.4}$$

In order to obtain the coordinates of intersection between the i-ray and the secondary reflector, the system including Equation 2.1 and Equation 2.4 has to be solved for the

parameter k and the coordinates of intersection $[x_{int,i}, y_{int,i}, z_{int,i}]$ are found.
The reflection at the hyperboloid intersection point is performed with the law of specularity. Given the surface normal vector $\hat{\mathbf{n}}$, an incident versor $\hat{\mathbf{i}}$ and a reflected versor $\hat{\mathbf{r}}$, the following two equation hold.

$$\hat{i} \cdot \hat{n} = \hat{r} \cdot \hat{n} \tag{2.5}$$

$$\left(\hat{i} \times \hat{r}\right) \cdot \hat{n} = 0 \tag{2.6}$$

In ideal condition Equation 2.5 states that the angle between the normal vector and the reflected one will be the same as the one between the normal and the incidence vector. Equation 2.6 guarantee that all the vectors lay on the same plane.
Given a i-ray incidence direction expressed by the aim versor and the normal secondary reflector versor evaluated as Equation 2.7, the reflected direction $[u^r_{x,i}, u^r_{y,i}, u^r_{z,i}]$ can be found solving Equation 2.5 and Equation 2.6, as shown in Equation 2.8.

$$n_{x,i} = \left.\frac{\partial f/\partial x}{\|n\|}\right|_{x_{int,i},y_{int,i}}; \quad n_{y,i} = \left.\frac{\partial f/\partial y}{\|n\|}\right|_{x_{int,i},y_{int,i}}; \quad n_z = -1; \tag{2.7}$$

$$\begin{gathered} u^r_{x,i} = u^a_{x,i} - 2sc \cdot n_{x,i}; \qquad u^r_{y,i} = u^a_{y,i} - 2sc \cdot n_{y,i}; \qquad u^r_{z,i} = u^a_{z,i} - 2sc \cdot n_z; \\ sc = n_{x,i} \cdot u^a_{x,i} + n_{y,i} \cdot u^a_{y,i} + n_z \cdot u^a_{z,i} \end{gathered} \tag{2.8}$$

Then, the ground image can be found knowing the position of intersection with the hyperboloid and the reflected direction. So another k value exists, connecting the surface intersection with a horizontal flat plane positioned at the lower focus and facing the aim point. However, in the case of ideal optic behavior, the ground image collapses into a point.

2.3.1. Geometrical consideration

Secondary reflector

As anticipated before, the more the eccentricity increases, the more the secondary reflector will be crushed to half of the focal distance and that will cause a higher hyperboloid radius as presented in Figure 2.4.

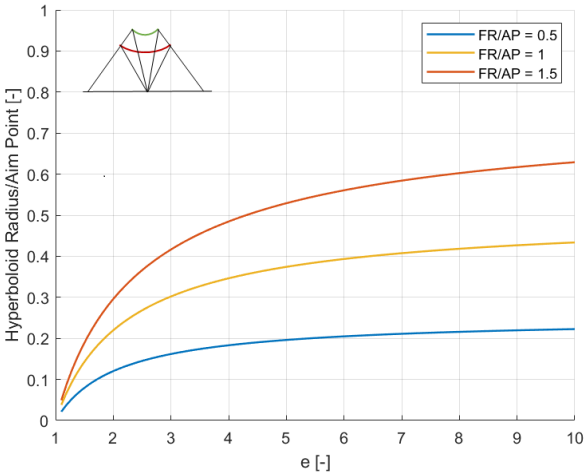

Figure 2.4: Hyperboloid radius variation at different eccentricity. The surface radius is defined by an ideal optic, considering Field Radius (FR) over Aim Point (AP) equal to 0.5, 1 and 1.5. Upper focus at z = 1 and lower at z = 0.

At a given eccentricity the hyperboloid radius follows the increase of the field one to catch the farthermost light point. To have a sensibility on the dimension of the secondary reflector in ideal optic, if we consider an aim point equal to 100 m and a field radius of 150 m, the hyperboloid radius will be 40 m for an eccentricity equal to 3, approximately half of the field.
The radius trend can lead to thinking that the secondary reflector area increase as the eccentricity increase. As shown in Figure 2.5, this reasoning is confirmed for an eccentricity value lower than 2.5, but then the hyperboloid area decreases as the eccentricity increase. The area value, A_{hyp}, can performed by integrating Equation 2.1 in polar coordinates along a circumference, between zero and the hyperboloid maximum radius, R_{hyp}, as shown in Equation 2.9.

$$A_{hyp} = \int_0^{2\pi} \int_0^{R_{hyp}} f(r\cos(\theta), r\sin(\theta))\ r\, dr\, d\theta \tag{2.9}$$

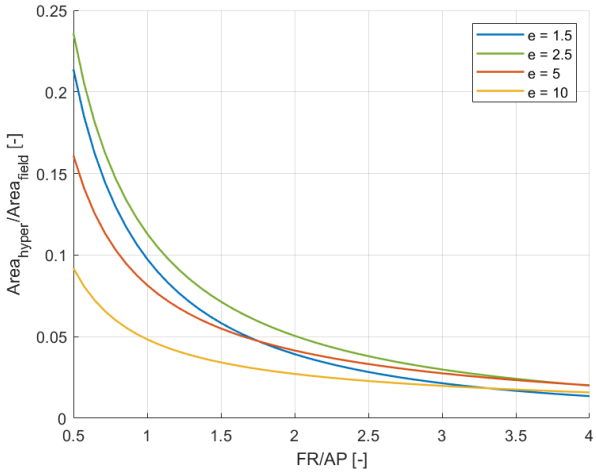

Figure 2.5: Hyperboloid-field area ratio. The surface radius is defined by an ideal optic, considering Field Radius (FR) over Aim Point (AP) varying from 0.5 to 4. Upper focus at z = 1 and lower at z = 0.

Again if we consider the same field as before, FR/AP equal to 1.5, the area of the hyperboloid is almost 7% of the field one. The trend tends to flatten out for a bigger field radius or lower aim point. At eccentricity equal to 1.5, the hyperboloid radius sensibly reduces and so its area.
Moreover, as anticipated before, as eccentricity increases the secondary reflector squeezes to half the focal distance. Therefore the center height, as shown in Figure 2.6, decreases and so does the relative tower cost at the same weight.
At value of eccentricity over 10, the hyperboloid becomes a flat surface at half of the focal point distance.

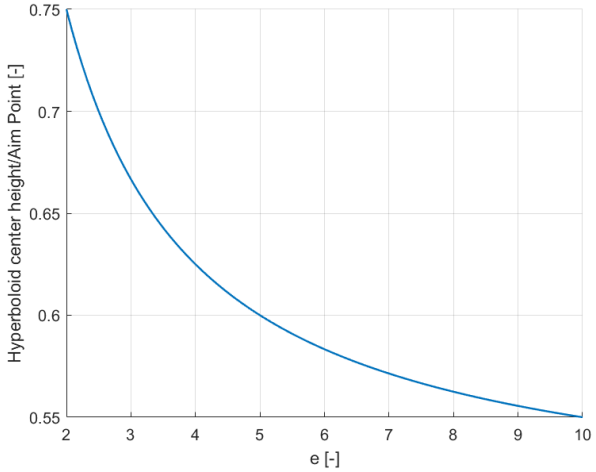

Figure 2.6: Hyperboloid vertex point height at eccentricities varying from 2 to 10.

Compound Parabolic Concentrator

Another important geometric parameter to consider in designing a beam-down optic is the Compound Parabolic Concentrator (CPC) entrance acceptance angle.
In the next paragraphs will be explained how the real optic causes error amplification on the ground image and a concentrator is generally needed to decrease and homogenize the receiver image in order to boost the thermal receiver performances.
As anticipated before the CPC is a particular concentrator in which the focal point of one parabola coincide with the end of the other one.
Following Figure 2.7, if the inlet angle θ_i of the ray coming from the secondary reflector is higher than the maximum one allowed by the CPC, θ_{max}, the ray will be rejected out and so it cannot be collected by the receiver. This angle is also defined as the half of the angle between the connection lines of the upper and lower ends of the two parabolas.

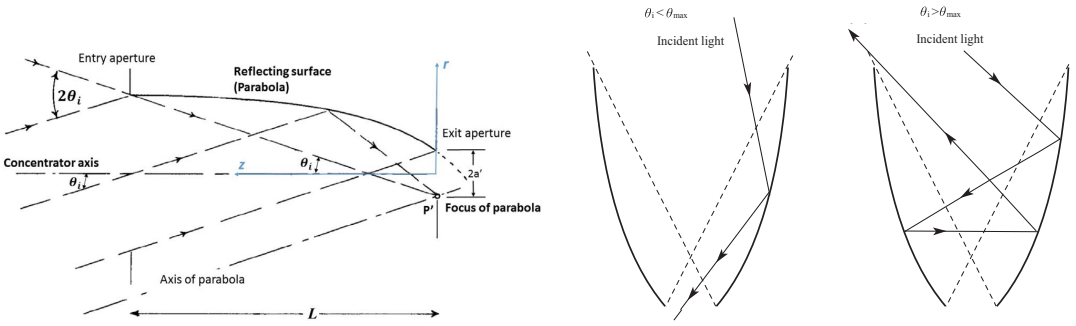

Figure 2.7: 2D representation of a Compound Parabolic Concentrator (CPC) [45][52].

The theoretical 2D concentration ratio of the CPC can be evaluated as Equation 2.10.

$$CR_{cpc,2D} = \frac{1}{sin(\theta_{max})} \tag{2.10}$$

Where θ_{max} is the maximum value of incidence angle measured from the longitudinal axis of the CPC. The theoretical value of the CR presented, is strictly true in 2D optic. Each ray entering with an angle lower than the admissible one will be transmitted. That's can be also the case for a 3D shape only if all the incidence rays intercept the longitudinal axis at the CPC entrance.
The higher will be the secondary reflector eccentricity, the higher will be the maximum entrance angle into the CPC aperture, so the lower the concentration ratio. This is mainly caused by an increase of the zenith angle of the hyperboloid normal vector as eccentricity increases and by Snell law, a higher angle of reflection.

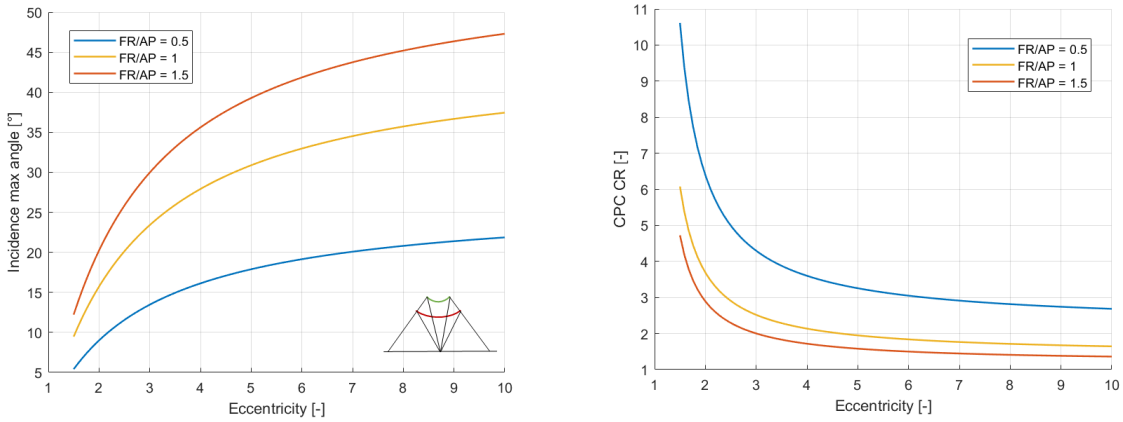

(a) Acceptance angle

(b) 2D concentration ratio

Figure 2.8: 2D variation of CPC entrance acceptance angle (left) and CPC concentration rario (CR) (right). Ideal optic, considering Field Radius (FR) over Aim Point (AP) equal to 0.5,1 and 1.5, upper focus at z = 1 and lower at z = 0.

As presented in Figure 2.8, the bigger the field radius at the same aim point height, the higher will be the acceptance angle.
This effect is caused by an increased incidence angle on the hyperboloid surface of the farthermost field light point, and so a related bigger reflected angle.
The 2D concentration ratio of the CPC ranges from 5 at eccentricity equal to 1.5 and FR/AP equal to 1.5, till almost 1.5 at eccentricity equal to 10. The trend for a bigger field is flattened out at eccentricity higher than 5.
The higher the CR of the CPC the smaller will be the outer image at the same inlet radius. On the other hand, this is at the expense of the CPC height. The higher is the CR the higher will be the CPC height. This value may reach a sensibly high number for high CR. If we consider 1 m receiver aperture radius, for 2D CPC concentration ratio equal to 3.5, the height of the tertiary concentrator reaches values around 15 m.
For that reason, generally, an array pattern is utilized. The same CR can be kept but partitioning the receiver aperture can reduce the height of the tertiary concentrator.
Another possibility can be the truncation of the CPC. It consists of a height reduction because in the upper half of the CPC, the increase in height along the longitudinal axis, H_T, is not followed by a sensibly increase in width, a_T, as shown by the almost vertical curve of Figure 2.9. Practise shows that even if the upper part of the CPC is deleted, the CR doesn't decrease so much.

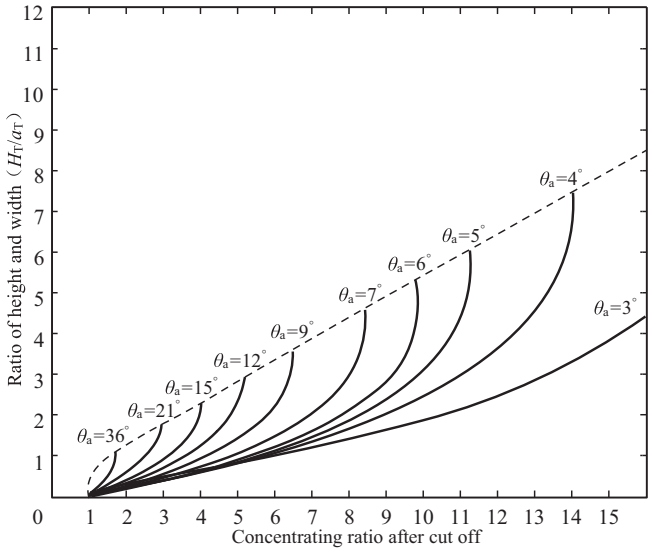

Figure 2.9: 2D CPC truncation curves at different maximum acceptance angle. The dashed line represents the full CPC geometry. θ_a is the maximum acceptance angle [52].

A complete 3D CPC is then obtained by the surface of the revolution of the 2D CPC along its longitudinal axis and its concentration ratio will be the square of the 2D one.

$$CR_{cpc,3D} = \frac{1}{(sin\ \theta_{max})^2} \tag{2.11}$$

2.4. Real optic

2.4.1. Optical errors

In the real optic model, the ray is affected by deviation from the ideality of Snell's law. A general ray due to sun shape, material defects, and imperfections is scattered and not perfectly reflected.
These types of errors can be divided into sun shape errors, slope errors, specularity errors, tracking errors, and shape errors.

Sunshape errors

The sun viewed from the Earth appears as a disk, not as a point source. The sun shape can be described by the normalized radiance profile $\hat{L}(\theta)$ of the solar radiation that represents the energy rate per unit of normal projected area and per unit of solid angle in a specific direction.

Considering a generic parabolic collector, normal to the sun and casting the rays towards a solar concentrator with direction defined by (θ, ϕ), the radiant power transmitted can be evaluated by Equation 2.12.

$$d\hat{q} = \hat{L}(\theta) sin\theta d\theta d\phi cos\theta dA \tag{2.12}$$

Where $sin\theta d\theta d\phi$ is the solid angle and $cos\theta dA$ is the area of the areola in perpendicular direction to θ and ϕ, as figured in Figure 2.10.

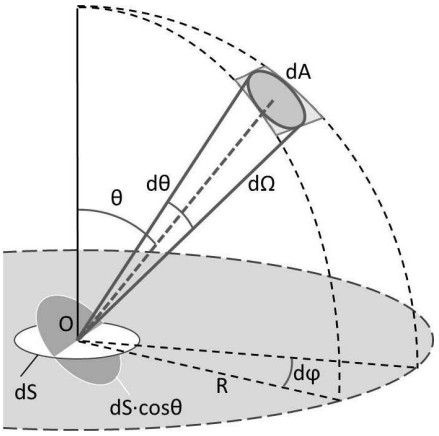

Figure 2.10: Solid angle definition for a reflected direction identified by θ and ϕ [32].

The overall hemispherical radiant power can be then calculated by integrating Equation 2.12 in $\theta = [0, 2\pi]$ and $\phi = [0, \pi/2]$.
The ratio between the radiant power in a specific direction and the overall hemispherical contribution, as expressed in Equation 2.13, express the probability of a ray leaving the collector surface in a certain (θ,ϕ) direction [24].

$$P(\theta, \phi) = \frac{\hat{L}(\theta) sin\theta cos\theta d\theta d\phi}{\int_0^{2\pi} \int_0^{\pi/2} \hat{L}(\theta) sin\theta cos\theta d\theta d\phi} \tag{2.13}$$

Slope errors

If we deepen our look at the surface of a generic object, we can detect some irregularities caused by the process of fabrication. The specific industrial procedure can minimize this effect but is nearly impossible to delete them or in general, will be a trade-off between cost and performance of the object considered.
Slope errors, as shown in Figure 2.11, represent ideal surface deviation on a larger scale

(local ripples or distortions) than specularity ones, which refer to the micro-surface aberration effect.

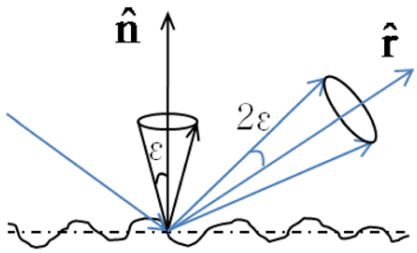

Figure 2.11: Slope errors [9].

These irregularities can be modeled considering a statistically correlated perturbation, $\hat{p}(\theta)$, of the ideal normal surface so that the real reflection will differ from the ideal one. Therefore the probability of a generic normal vector pointing in a generic direction (θ, ϕ) is given by Equation 2.14.

$$P(\theta,\phi) = \frac{\hat{p}(\theta) sin\theta d\theta d\phi}{\int_0^{2\pi}\int_0^{\pi/2} \hat{p}(\theta) sin\theta d\theta d\phi} \tag{2.14}$$

Specularity errors

We have seen as slope errors affect the surface scattering effect caused by deviation from the ideal surface at a slightly larger scale. On the other hand, specularity errors, as shown in Figure 2.12, are caused by the microscopy non-ideality of a surface.

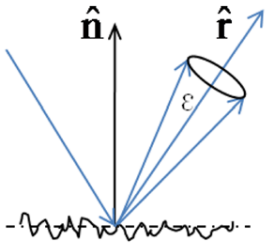

Figure 2.12: Specularity error [9].

A general deviation from the specular reflection is again statistically correlated and the probability can be evaluated with Equation 2.14. The only difference is that, while the slope error affects the normal surface vector, the specularity error is generally defined as a reflected ray variation.

Shape errors

The last error that can be identified on a reflector geometry is the shape error. As shown in Figure 2.13, heliostats are built by different facets and these facets may be oriented incorrectly caused by, for example, thermal expansion and wind loads that can bend the structure. This causes a scattering effect of the reflector that can be statistically as Equation 2.14.

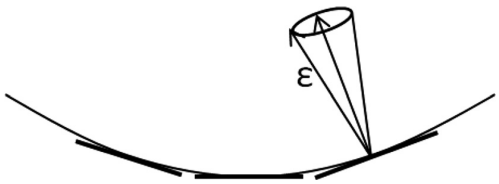

Figure 2.13: Shape error [9].

Tracking errors

In CSP application, heliostats have to change orientation systematically in order to follow the sun's movement and reflect the incident lights towards the aim point.
In order to attain these results, a motor-controlled tracking system is necessary. This type of system is not perfect and causes angular offset.
Again this type of error can be modeled as the geometrical defection errors explained before.

2.4.2. Combination of errors

In this work, was decided to neglect the contributions given by tracking error and shape error. It's really difficult to select individually the error value of each factor and we can simplify the problem by considering the shape and tracking error as a part of the slope error. This is a reasonable assumption because, despite the different mechanism that creates the error, they behave equally as a scattered surface, and thereby the slope error can be directly seen as the overall interference [24].
The probability function described in the previous sections for sun-shape model (Equation 2.13) and for geometrical distorsion (Equation 2.14) can be represented by a multivariate normal distribution.
Two angles θ and ϕ, representing the azimuth and zenith of a vector, can uniquely characterize an ideal direction. Therefore, their value of disturbance $\delta\theta$ and $\delta\phi$ can be modeled by a bivariate normal distribution.

The probability distribution can be simplified by considering the disturbances independent one to each other. The distribution is represented by Equation 2.15.

$$f(\delta\theta, \delta\phi) = \frac{1}{2\pi\sigma_i^2} \exp\left(-\frac{1}{2}\left[\left(\frac{\delta\theta - \mu}{\sigma_i}\right)^2 + \left(\frac{\delta\phi - \mu}{\sigma_i}\right)^2\right]\right) \tag{2.15}$$

Where μ is the mean value and is equal to 0. σ_i is the standard deviation of the i-error considered. The bi-variate normal distribution trend is highlighted in Figure 2.14.

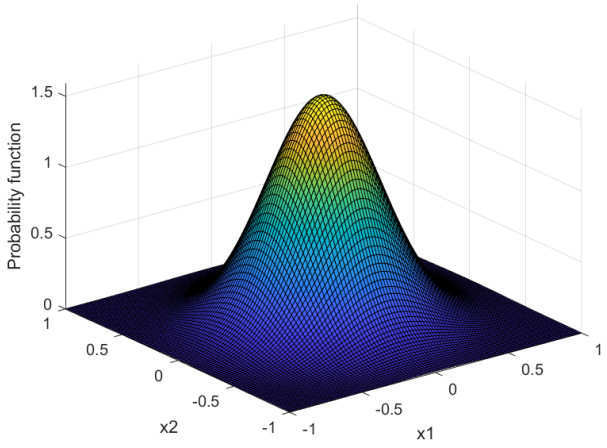

Figure 2.14: Bi-variate normal probability function.

In a ray-tracing program, each disturbance is applied in the stage in which it occurs, namely sunray and heliostat surface perturbation. On the other hand, a common method is the convolution of the sun, slope, and shape errors on the heliostat aiming direction. This method was firstly introduced in 1979 by the U.S. Department of Energy and it states that an overall standard deviation, for each angular i-disturbance, can be evaluated following Equation 2.16 [6].

$$\sigma_i = \sqrt{\sigma_{sun}^2 + 4\sigma_{slope,i}^2 + \sigma_{spec,i}^2} \tag{2.16}$$

Where σ_{slope} is multiplied by a factor 4 because a disturbation on the normal direction causes a double error on the reflected one. The method guarantees reasonable accuracy [30]. Given a reflected direction, a perturbation $(\delta\theta, \delta\phi)$ is applied on the ideal versor defined by (θ, ϕ) and the new vector cosines are evaluated.
The convolution is being considered only for the heliostat's geometric imperfection and the sun shape. The hyperboloid optic error is directly applied at the secondary reflector.

2.4.3. Error amplification effect

Ideally, all the field rays aimed at the upper focal point are concentrated in an infinitesimal ground image. This effect is guaranteed by the hyperboloid surface properties.
In real optic behavior, a ray won't reach perfectly the aim point due to optical disturbances and its intersection with the secondary reflector is not the ideal one. For this reason, the secondary reflector radius increases in order to catch the scattered rays.
Moreover, the optic error on the hyperboloid causes further aiming displacement and so the ground image will be again bi-normal statistically correlated, as shown in Figure 2.15.

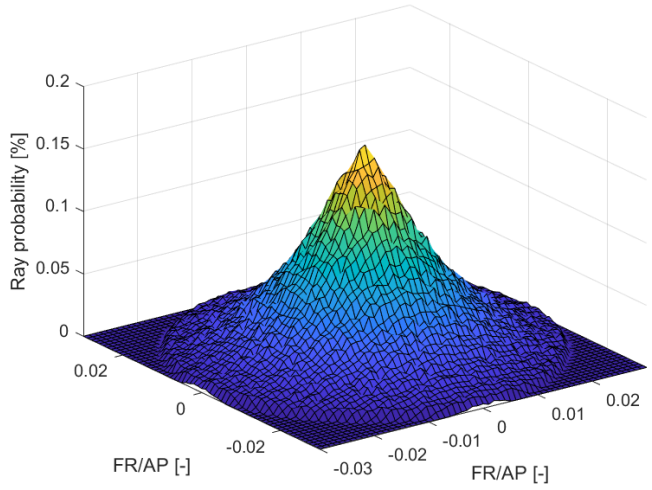

Figure 2.15: Ground image rays probability distribution. Simulation perform with 1 million rays.

Table 2.1 reports the value of optical errors considered.

Property	Value [mrad]	Description
σ_{sun}	4.1	Sun shape error
σ_{slope_f}	1.53	Heliostats field slope error
σ_{spec_f}	0.2	Heliostats field specularity error
σ_{slope_h}	1.53	Hyperboloid slope error
σ_{spec_h}	0.2	Hyperboloid specularity error

Table 2.1: Values of sun shape, slope and specularity errors considered. Values from default SolarPILOT configuration.

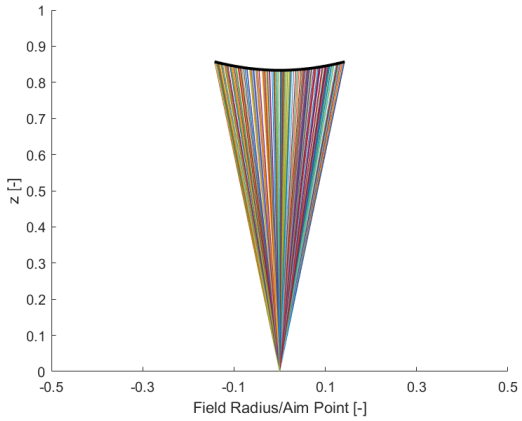

(a) Ideal Optic: e = 1.5

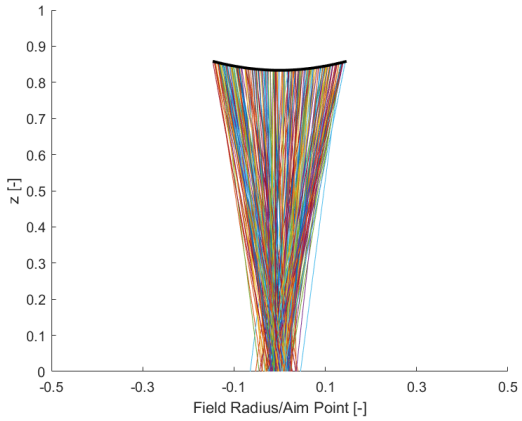

(b) Real Optic: e = 1.5

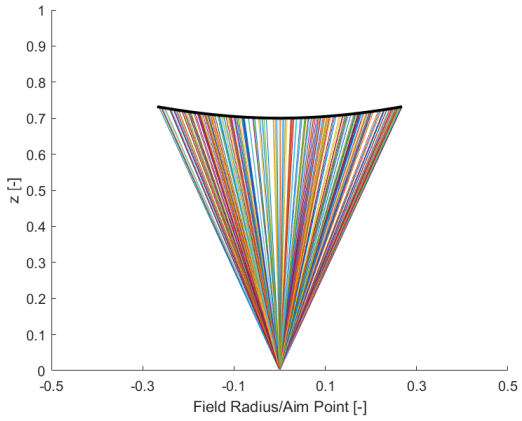

(c) Ideal Optic: e = 2.5

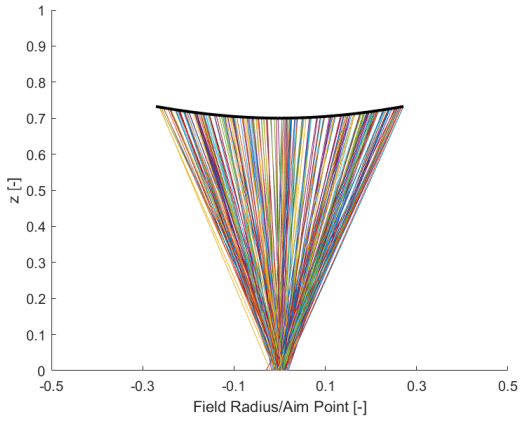

(d) Real Optic: e = 2.5

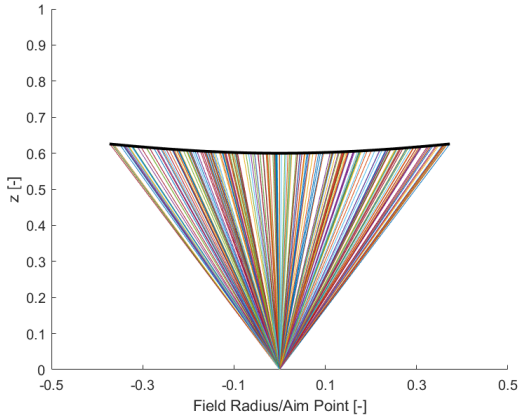

(e) Ideal Optic: e = 10

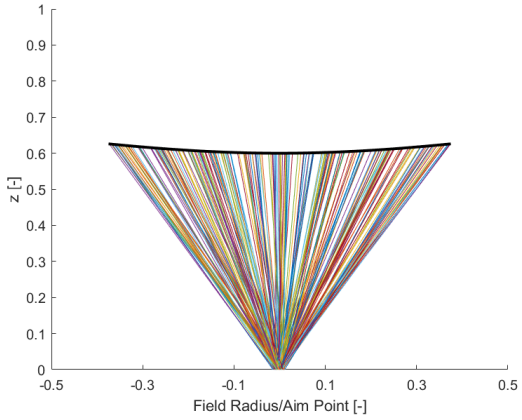

(f) Real Optic: e = 10

Figure 2.16: Hyperboloid 2D rays reflection. FR/AP equal to 1. Upper focus at z = 1 and lower at z = 0.

If the same values of optical errors are considered, namely the ones of Table 2.1, the bigger the distances between the ray ground position and the hyperboloid intersection, the higher error will cause on the ground image, simply because the distances between the ideal crossing and the real one in the secondary reflector is higher.
The error amplification effect at different eccentricity values is shown in Figure 2.16 and Figure 2.17.

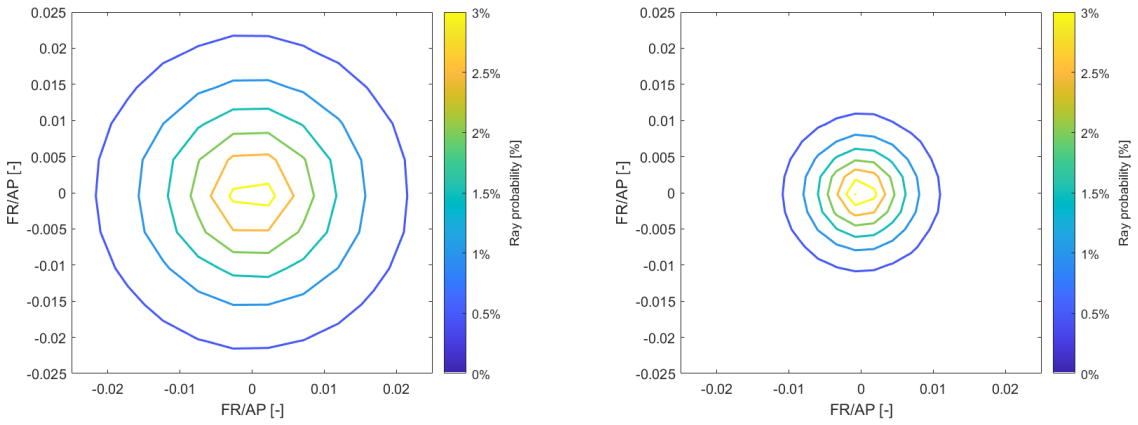

(a) e = 1.5 (b) e = 2.5

Figure 2.17: Ground image ray probability distribution. Bins 30x30. FR/AP equal to 1. Upper focus at z = 1 and lower at z = 0. Simulation perform with 1 million rays.

Translating these arguments into eccentricity consideration, the lower will be the eccentricity (bigger hyperboloid squeezed to the half of the focal point, so less ray path distances), the smaller will be the ground image, as shown in Figure 2.18. The scattering effect on the results is caused by the number of rays considered.
Nevertheless, a ray count over a million is generally sufficient to properly analyze the receiver flux [48]. A spillage factor of 1% was considered in order to avoid outlier values on the ground image radius.
At a given field radius over the aim point, the trend of the ground image radius is flattened out at an eccentricity higher than 4. By taking the same field example of before, FR/AP equal to 1.5 and eccentricity equal to 3, the CPC inlet radius, if present, or the receiver one is almost 5 m.

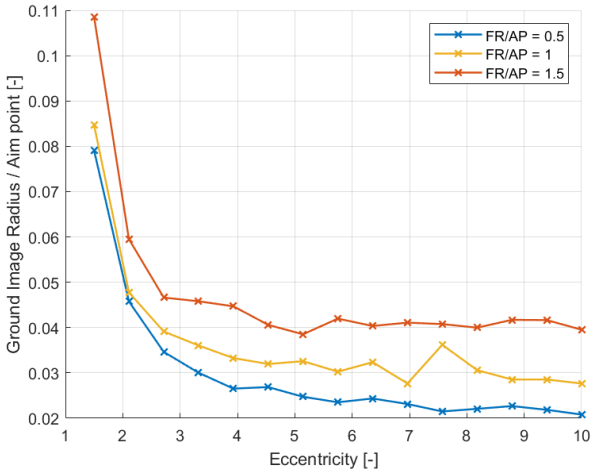

Figure 2.18: Ground image radius at eccentricity varying from 1.5 to 10 and Field Radius (FR) over Aim Point (AP) equal to 0.5, 1 and 1.5. 1 million ray simulation. Ground image spillage equal to 1%.

Furthermore, if we consider a real flat heliostat and not a single light point source coming from the ground, the aberration effect plays another big role in the ground image amplification effect. Given a sun position, the mirror rotates in order to cast the ray coming towards the aim point. The movement is identified by the displacement of the normal vector of the mirror and so the same normal direction is applied to every point of the mirror, as figured in Figure 2.19. This causes a spread image at the upper focus and so an even higher ground one.

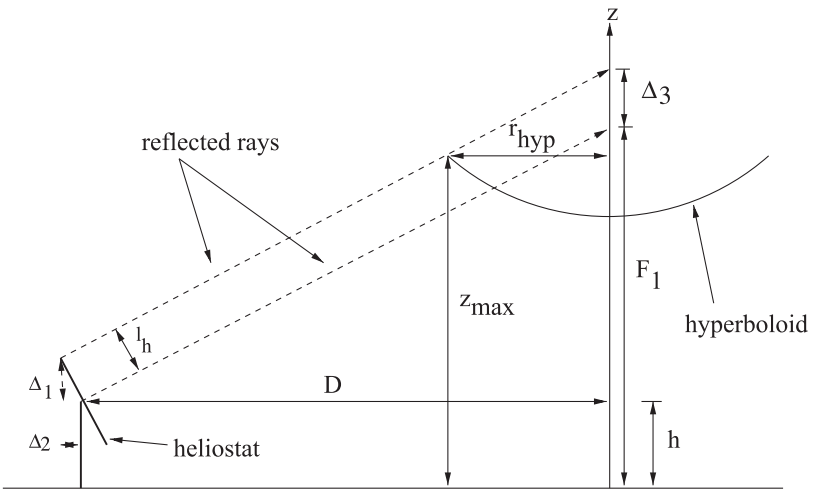

Figure 2.19: Aberration effect [25].

3 | Heliostat field creation

In this chapter, the methodology utilized to build a 50 MW_{th} beam-down solar field is presented. Starting from the implementation of the radial staggered field method for solar towers introduced by Collado et al. [13], the optical performance of each mirror are evaluated considering the presence of a secondary reflector.
The intercept factor is assessed by a randomly generated rays distribution on the heliostats surface. Shadow and blocking performance are calculated thanks to Sassi projection [40]. As anticipated before, current beam-down installations are composed of a surrounded circular field. In this work, a possible asymmetric field pattern is presented to favor the increased cosine efficiency at latitudes far from the equator. To do so, the secondary reflector shape was unconstrained making use of a sliced surface.
The optic of a solar tower system is sensibly affected by various derating factors. Following the sun rays' path, not all of them will be redirected towards the upper focal point by the heliostat's surface due to the reflectivity effect. Moreover, neighbor mirrors can shadow or block each other, diminishing the mirror's effective surface. Shadows performance refers to the sun vector while blocking ones take into account that a reflected sun ray from the mirror surface can be blocked by another interfering heliostat.
Moreover, Beam-Down system introduces two other optical losses, namely the shadow of the secondary reflector and its reflectivity effect. In this sense, it was found that the hyperboloid shadow effect sensibly affects the best cosine part of the field, especially at high eccentricity values (bigger secondary reflector). An annual optimization method will then be presented where farther, less shadowed, heliostats are inserted in favor of deleted inner worst performing ones.
Finally, an overall optimization considering the CPC geometry and the annual secondary reflector shadow is introduced at different eccentricities and aim point values and the best field configurations found are assessed also in terms of techno-economic parameters.
The mirrors will be considered rectangular and made by one facet.

3.1. Radial staggered pattern

A possible heliostats field configuration can be the one of a radial staggered. This mirrors pattern has been firstly introduced by the University of Houston and utilized in the software for designing solar towers called DELSOL3 [22].
As shown in Figure 3.1, two main parameters identify the disposition of the mirrors, the azimuthal distance ΔAz and the radial displacement ΔR.

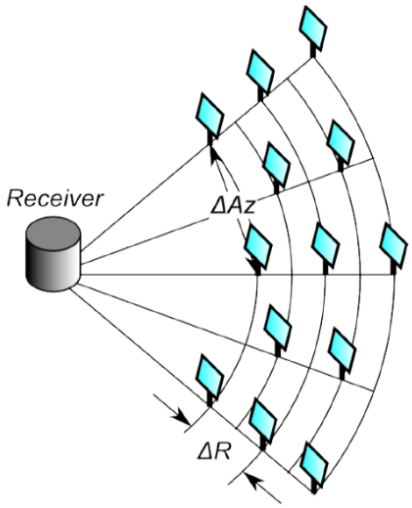

Figure 3.1: Radial staggered layout [37].

The design considered has the main advantage of easy blocking heliostat individuation. Considering a generic heliostat, three blocking mirrors can be identified: two in the outer next row at both sides of the radial axis of the heliostat considered, named shoulder, and one just in front in the outer second row, named nose.
In order to generate the heliostats field in Matlab, the *campo* code developed by Collado et al. [13] were utilized and here presented.
Mirror rotates along two axes to displace their normal vector in the right position such that the reflected ray is directed towards the aim point. However, this movement is confined into a sphere of diameter equal to the heliostat diagonal DM. Moreover, a further security displacement can be added equal to *dsep*. By saying that, as shown in Figure 3.2, the densest heliostats configuration is the one that separates the center of each mirror, one to another, by $DM + dsep$.

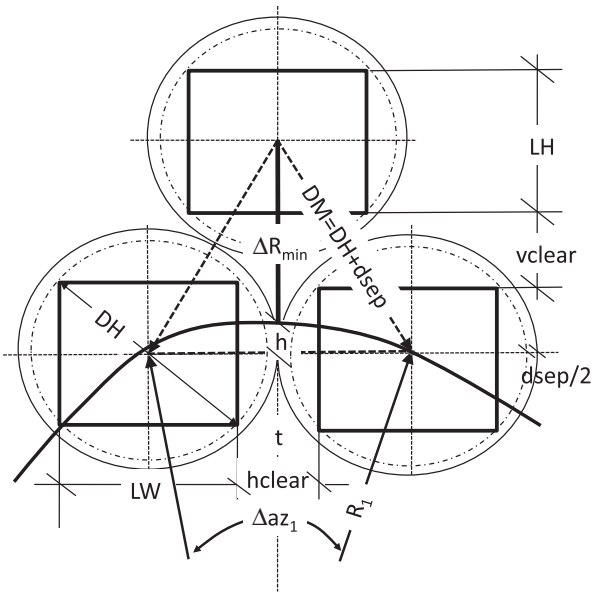

Figure 3.2: Densest field layout configuration for radial staggered pattern [13].

Let's consider a Cartesian plane where the X-axis is pointing East and Y-axis to North and a minimum field radius $R1$ selected by the user. The azimuthal separation between mirrors in the first row can be found with Equation 3.1. So the number of heliostats in the first row, considering *dsep* equal to zero, is given by Equation 3.2.

$$\Delta az_1 = 2 \cdot asin\left[DM/\left(2R_1\right)\right] \cong DM/R1 \tag{3.1}$$

$$Nhel_1 = 2\pi/\Delta az_1 \tag{3.2}$$

In order to insert an integer number of mirrors, the result from Equation 3.2 is rounded and a new azimuth distance is found.
The first row can now be placed. Field rows, are divided into even and odd rows.
The first heliostat of an odd row, for example the first one, is placed at $\Delta az_1/2$ counter-clockwise from the north, while the first one of an even row, for example the second one, is placed at North, as presented in Figure 3.3.
The DELSOL3 correlation is utilized for the radial spacing between rows. As anticipated before, the equation is a curve fitting to optimized field layout by the University of Houston [22].

Given a generic row, the outer next one will be displaced by ΔR, expressed as Equation 3.3.

$$\Delta R = \left(1.1442 \cdot cotan\ \theta_l - 1.0935 + 3.0684 \cdot \theta_l^2\right) \cdot HM \tag{3.3}$$

Where:

- $\theta_l = \frac{\pi}{2} - \theta_t$.
- θ_t is the zenith angle of the heliostat aiming vector.
- HM is heliostat mirror height.

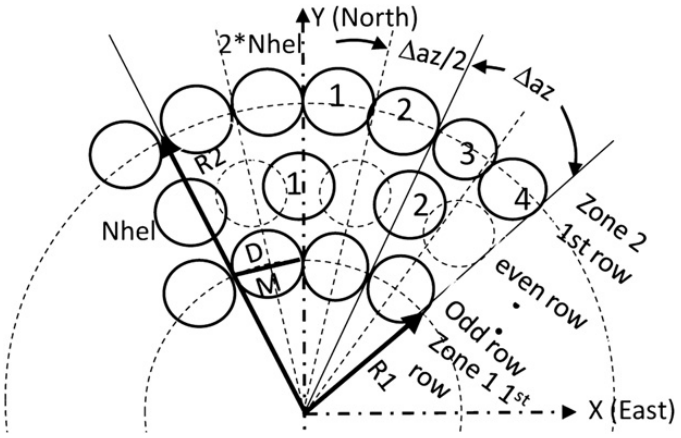

Figure 3.3: Generation of radial staggered layout [13].

Furthermore, the field is divided into zones. Rows of mirrors that share the same azimuth distance belong to the same zone.
Starting from the minimum radius selected and building row by row the field, at a certain radius, the azimuth distance allows for the insertion of the double amount of heliostat of a previous row, as shown in Figure 3.3. The azimuth distance Δaz_2 become half of Δaz_1 and a new zone is formed.
Normally, the threshold between the azimuth distance ratio of two neighbor zones can be set a priori. In the case presented before where a new compressed row is started when the ratio of $\Delta az_1/\Delta az_2$ is equal to 2, the number of mirrors in the new zone will be double of the previous ones.
Following SolarPILOT default configuration for radial staggered DELSOL3 heliostat field creation setting, a new compressed row is started when $\Delta az_1/\Delta az_2 = 1.33$, as shown in

Figure 3.4. This lower threshold guarantees lower azimuth spacing at a higher radius, and so a denser field layout.

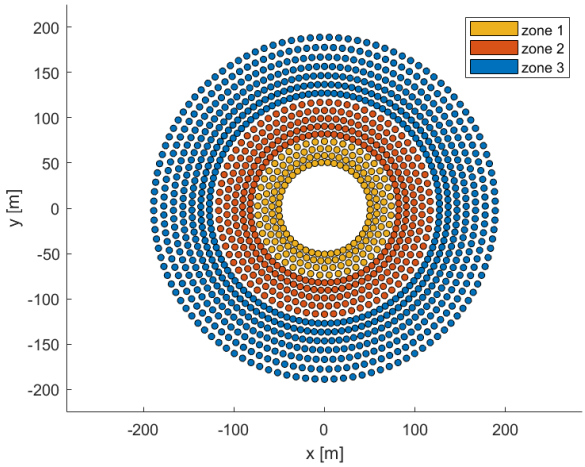

Figure 3.4: Radial staggered layout zone identification. Minimum field radius equal to 50 m, maximum equal to 200 m. Rectangular heliostat 5x5 m.

Each i-heliostats in the field is then identified by its position x_i, y_i, and its installation height z_i and its aiming vector cosines $[u^a_{x,i}, u^a_{y,i}, u^a_{z,i}]$.
In order to rapidly access the heliostat variables, all the field is grouped into a Matlab cell called *campo*. The cell is divided into K cells where each k-cell represents one zone of the field. For each zone there are J-rows cells belonging to the k-zone and each j-row is composed by I cells where each i-cell represent one heliostat of the considered zone and row.
Moreover, every i-cell is composed of two other cells. In the first are inserted data regarding the position of the mirror in the field and the cosine of the aiming vector, and, as will be explained later on, the subsection belonging to that mirror. In the second cell are present information regarding the heliostat design performance (design optical efficiency and secondary reflector geometry), the minimum and maximum radius, and azimuth extension of the circular sector hyperboloid belonging to the i-mirror. The evaluation of the specifications regarding the second cell of the i-heliostat will be explained in the section 3.3.

3.2. Optical field efficiency

Ideally, in Concentrating Solar Plants (CSP), a generic surface can redirect the Direct Normal Incidence radiation (DNI) towards the receiver. By saying that the ideal power reflected by the i-mirror toward an infinite receiver can be evaluated as Equation 3.4.

$$\dot{W}_{sun} = DNI \cdot A_{helio,i} \tag{3.4}$$

Where $A_{helio,i}$ is the area of the heliostat surface. In reality, different types of losses take place in the ray path from the energy source towards the receiver and so an optical efficiency is defined. The latter, in the case of a Beam Down system, is presented as Equation 3.5.

$$\eta_{opt} = \rho_{helio} \cdot \rho_{SR} \cdot \eta_{cos} \cdot \eta_{sb} \cdot \eta_{int} \cdot \eta_{s,SR} \tag{3.5}$$

Where:

- ρ_{helio} is the reflectivity of the mirror surfaces.
- ρ_{SR} is the reflectivity of the secondary reflector.
- η_{cos} is the cosine efficiency.
- η_{sb} is the shadowing and blocking efficiency.
- η_{int} is the intercept efficiency.
- $\eta_{s,SR}$ is the shadow efficiency caused by the presence of a secondary reflector.

New terms like ρ_{SR} and $\eta_{s,SR}$ appear in the beam-down application, concerning solar tower, due to the presence of a secondary reflector. Each of these terms will be presented in the following subsections.

3.2.1. Reflectivity

Taking into consideration a radiation source and a surface, reflectivity is defined as the percentage of the reflected wave to that of the incidence wave. It's generally a function of the wavelength.
In beam-down system with respect to the solar tower, also the reflectivity, and so the wasted energy, of the secondary reflector has to be considered.

3.2.2. Cosine effect

It represents the most significant loss in solar tower technology. If we consider Snell's law, an incidence ray, ideally, is reflected in a specular direction with respect to the normal of the surface considered. By saying that, the heliostat normal has to rotate to bounce the reflected vector towards the aim point. As shown in Figure 3.5, the mirror won't be perpendicular to the source of radiation and the effective reflective area is the one represented by the cosine of the ray incidence angle with respect to the mirror normal surface.

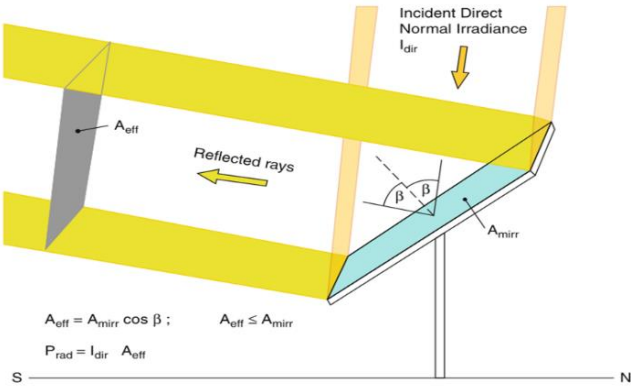

Figure 3.5: Cosine effect [50]

Considering a generic sun ray versor $\hat{\mathbf{s}}_\mathbf{i}$, hitting the i-heliostat and its correspondent specular reflection versor $\hat{\mathbf{r}}_\mathbf{i}$, the cosine efficiency can be evaluated as Equation 3.6.

$$\eta_{cos,i} = \cos\left[\arccos\left(\hat{\mathbf{s}}_\mathbf{i} \cdot \hat{\mathbf{r}}_\mathbf{i}\right)/2\right] \tag{3.6}$$

In solar power technologies, the cosine effect can give a first field shape. In the northern hemisphere, where the sun is mainly in the South throughout the year, the heliostat positioned on the North part of the field will perform better than the ones at the South. If we consider a generic latitude and a maximum field radius, a annual cosine map can be built, as shown in Figure 3.6. The cosine efficiency of each point is evaluated on a DNI clear sky basis.
The cosine map can be utilized as the first field shape. However as it will be shown later on, the other performance factor plays their role as well in the final configuration.

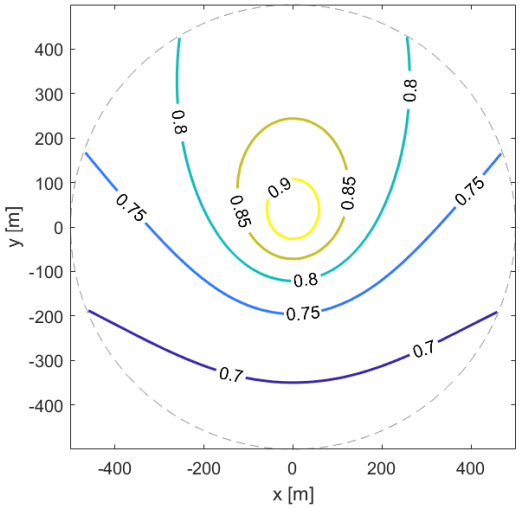

Figure 3.6: Annual clear sky DNI weighted cosine efficiency at ground level. Latitude equal to 25° N, aim point equal to 100 m. Field radius equal to 500 m.

3.2.3. Shadowing and Blocking

Shadowing loss takes place when the incidence radiation targeting a generic i-heliostat, hits another interfering k-heliostat. On the other hand, blocking refers to the part of radiation reflected by the i-mirror that doesn't reach the receiver because it's blocked by an interfering k-heliostat. In practice, shadowing is defined on the sun vector pointing the i-heliostat considered, while blocking refers to the reflected rays.
This loss can be both expressed as a number of rays of the i-heliostat that ideally reach the receiver over the ones coming from the sun that were supposed to hit it or in terms of area of the heliostat obscured by the interfering K-neighbour heliostats over the overall one.
This type of loss, as the cosine one, is sun position-dependent and related to the reciprocal position of the i-mirror over the one of the K-neighbours. For this reason, the Shadowing and Blocking (S&B) efficiency is the most energivourous in terms of computational time when a ray-tracing method is not utilized. The most time-consuming part result in the individuation of the k-interfering heliostats over the i-heliostat analyzed at a given sun position and a solar field.
The radial staggered configuration, as expressed before guarantees easy blocking individuation, as shown in Figure 3.7. Taken into consideration a generic i-heliostat in the field, three blocking k-heliostat can be easily found, two in front on the first inner row, named shoulders, and one directly in front in the second inner row, named nose.

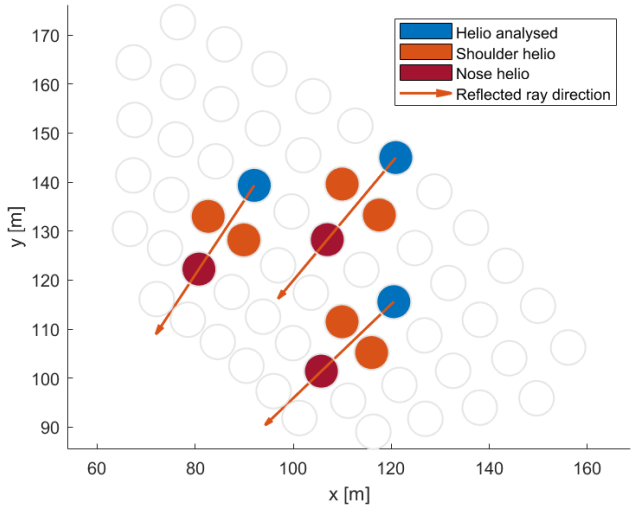

Figure 3.7: Blocking heliostats identification for a radial staggered field pattern.

This is not strictly true for heliostat living in the first row (missing direct nose and shoulder association) or second row of a new zone (missing the nose), so where a new compressed row is started. The arrangement of the mirrors is changed and the identification of the interfering heliostat has to be made by distances consideration.
The same procedure is utilized for possible shadow candidates. The only difference is that, blocking selection is based on the aiming vector of i-heliostat $\overrightarrow{\mathbf{a_i}}$ while for shadowing the sun vector pointing at the i-heliostat at a given sun position, $\overrightarrow{\mathbf{s_i}}$, is considered.
Let's consider a vector $\overrightarrow{\mathbf{t_i}}$, that can be either $\overrightarrow{\mathbf{a_i}}$ for blocking performance or $\overrightarrow{\mathbf{s_i}}$ and a i-heliostat defined by its normal vector $\overrightarrow{\mathbf{n_i}}$ such that $\overrightarrow{\mathbf{s_i}} + \overrightarrow{\mathbf{a_i}} = \overrightarrow{\mathbf{n_i}}$.
It's possible to calculate a length of interaction for the i-heliostat that represents the farthest mirror projection point onto the ground in a 2D plane by solving the system of a straight line passing from the highest point of the heliostat and a plane at $z = 0$, as presented in Figure 3.8.

$$L_{int} = \frac{\left(h_i + \frac{DM}{2}\sin\theta\right) \cdot \sqrt{t_x^2 + t_y^2}}{t_z} + DM\cos\theta_z \tag{3.7}$$

Where DM is the mirror diagonal, h_i the installation height and θ_z the zenit angle of $\overrightarrow{\mathbf{n_i}}$.

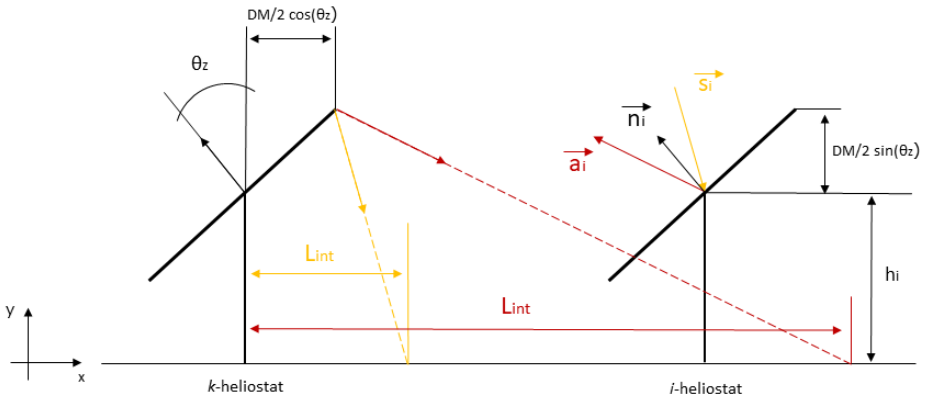

Figure 3.8: Shadowing and blocking length of interaction.

Equation 3.7 assumes that both mirrors have the same normal vector, namely the one of the i-mirror analyzed, and that the worst-case condition is considered, the one in which the highest point is defined by $DM/2 \cdot \cos\theta$. The heliostat that has a distance from the i-heliostat higher than L_{int} cannot interfere with shadowing or blocking.
All the mirrors that could be potentially individuated as blocking ones live in the inner rows with respect to the i-heliostat considered, since $\overrightarrow{\mathbf{a_i}}$ is always pointing to the upper focus. On the other hand, shadowing mirrors could be likely all around the heliostat considered. Nevertheless, these mirrors have always a positive distance from a straight line with normal $\overrightarrow{\mathbf{s_i}}$ and pass through the center of the heliostat, so they are in front of the i-heliostat at a given sun position, as shown in Figure 3.9.

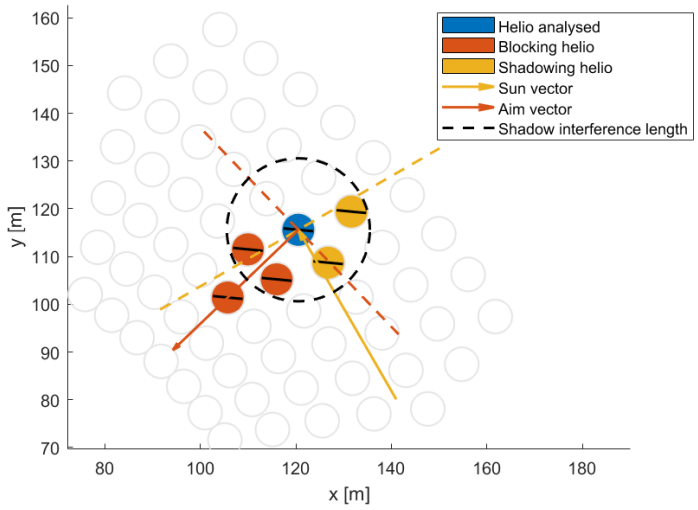

Figure 3.9: Shading and blocking heliostats individuation. Sun elevation and azimuth equal to 15° and -30°.

The S&B performance was implemented in Matlab utilizing the Sassi method [40] which is explained in detail in Appendix A. Briefly, the method first projects the center point of the k-interfering heliostat onto a plane defined by the normal vector of the i-heliostat $\overrightarrow{\mathbf{n_i}}$. Moreover, given the projection, the k-mirror is overlapped to the mirror considered. The i-mirror of width (WM) and height (HM) is divided into two halves of equal geometry WM and HM/2. Each half is discretized among WM in R-interval. For each step, if the k-heliostat covers the overall interval r-extension, the area covered by that mirror will be $WM/R \cdot h_k$, where h_k is the height of the overlapping projection. Performing the same method for all the K-heliostats, the S&B efficiency is evaluated as the "free" surface over the overall one.
The main assumption of the procedure are that:

- All the interfering K-heliostat have the same normal vector as the i-mirror.
- The overlapping area of the k-mirror onto the i-heliostat is limited in height by half of the mirror height (HM/2).

These two assumptions are reasonable since interfering heliostat live in the neighbor of the i-mirror considered and the radial and azimuth distance between them guarantee limited overlapping.

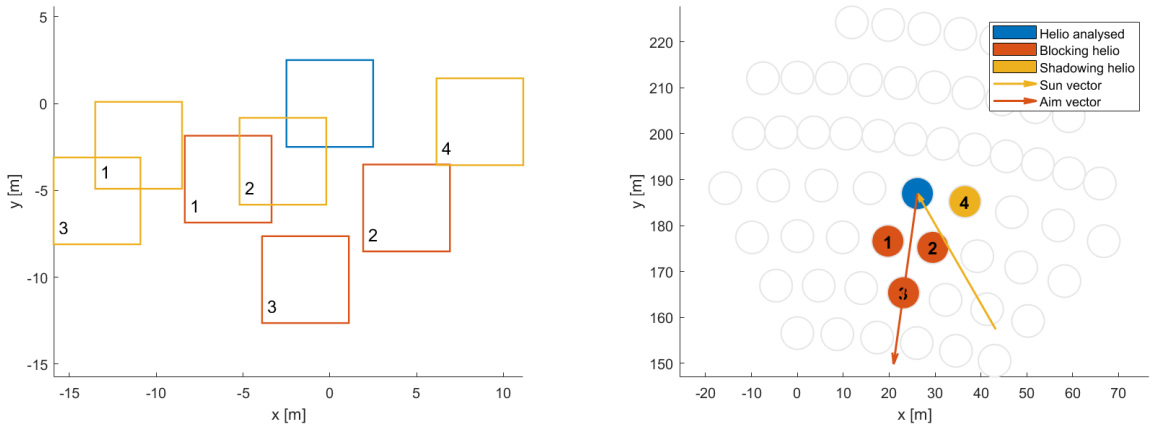

(a) Sassi projection method.

(b) Interfering heliostats individuation.

Figure 3.10: Shadowing and Blocking performance calculation. η_{sb} evaluated equal to 84.93%. Sun elevation and azimuth equal to 15° and -30°. Rectangular heliostats 5x5 m size.

3.2.4. Intercept factor

The intercept factor represents the percentage of the heliostat reflected image that reaches the receiver over the overall one. This problem emerges from optic errors, as presented in the previous chapter.
Ideally, every reflected ray will fall into an infinitesimal ground image. Actually, sun, shape, and slope errors cause a ground image's rays probability distribution.
A normal ray tracing will generate a probabilistic disturbance at every point where it takes place. So the sun vector is affected by the sun shape error and so on. With sufficient accuracy, the problem can be simplified by the convolution of the heliostat and sun error on the mirror surface.
Considering a bunch of rays that leave the i-mirror, $N_{ray,i}$, that are not blocked by any other k-heliostat and that reach a perfect secondary reflector surface ($\rho_{SR} = 1$), the intercept efficiency can be evaluated as Equation 3.8.

$$\eta_{int,i} = \frac{N_{rec,i}}{N_{ray,i}} \tag{3.8}$$

Where $N_{rec,i}$ are the number of rays falling inside a specific dimension of the receiver from the i-heliostat.
However, in beam down system, the ground image can be represented as a bivariate normal distribution and so its boundary can be approximated to the one of a circumference.
Considering a generic i-heliostat, the intercept factor is assessed by generating a random number of rays on the mirror surface, intersecting them with the secondary reflector, and bouncing them on a selected receiver dimension.
In order to generate a random positioned bunch of rays inside a surface defined by its normal vector $\overrightarrow{\mathbf{n_i}}$, the light points are first randomly generated inside a horizontal plane bounded by the geometric mirror dimension, width (WM) and height (HM), and then rotated along the X-axis and Z-axis by respectively the zenith and azimuth angle of $\overrightarrow{\mathbf{n_i}}$.
More precisely, the generation of a random point with coordinates $[x_j, y_j, 0]$ inside a rectangle centered in a XYZ plane, is governed by Equation 3.9.

$$x_j = WM \cdot rand - WM/2; \qquad y_j = HM \cdot rand - HM/2; \tag{3.9}$$

Where $rand$ is a uniform probabilistic distributed random number between 0 and 1.
Moreover, the point is rotated along X and Z axis, thanks to Equation 3.10.

$$\begin{bmatrix} x_j^r \\ y_j^r \\ z_j^r \end{bmatrix} = \mathbf{R_x} \cdot \mathbf{R_z} \cdot \begin{bmatrix} x_j \\ y_j \\ 0 \end{bmatrix} \tag{3.10}$$

Where $\mathbf{R_x}$ and $\mathbf{R_z}$ are the two rotation matrixes expressed as Equation 3.11. ϕ and θ are respectively the zenith and azimuth angle of the heliostat normal vector.

$$\mathbf{R_x} = \begin{bmatrix} 1 & 0 & 0 \\ 0 & \cos(\phi) & -\sin(\phi) \\ 0 & \sin(\phi) & \cos(\phi) \end{bmatrix}; \qquad \mathbf{R_z} = \begin{bmatrix} \cos(\theta) & -\sin(\theta) & 0 \\ \sin(\theta) & \cos(\theta) & 0 \\ 0 & 0 & 1 \end{bmatrix} \tag{3.11}$$

As shown in Figure 3.11, each point is then translated by the i-heliostat field coordinates $[x_i, y_i, z_i]$, where z_i is the installation height. The procedure explained assumes an azimuth-elevation sun-tracking method.

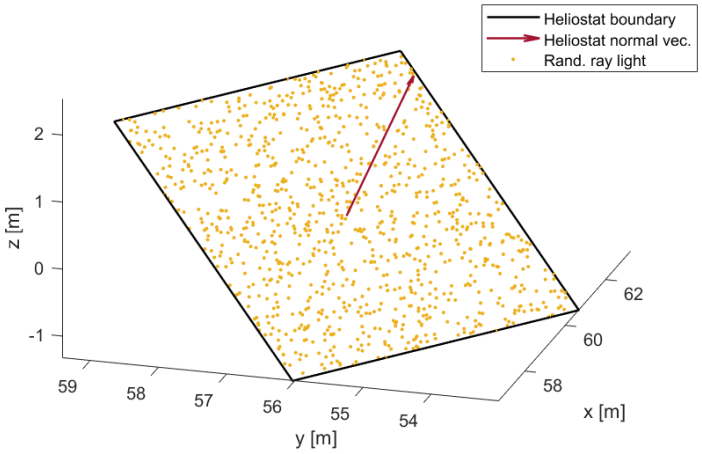

Figure 3.11: Random ray distribution on heliostats surface. Ray number equal to 300. Rectangular mirror 5x5 m.

The number of randomly generated rays defines the system's accuracy. However, this value depends on the solar field size. Intercept error on heliostats close to the aim point will be sensibly lower concerning mirrors positioned farther, at the same CPC geometry. Moreover, too high rays number can sensibly increase the computational time without any improvement in accuracy.
Furthermore, another CPC important characteristic, if present, is the maximum acceptance angle. Rays that fall inside a specific tertiary concentrator radius dimension with an incidence angle higher than the acceptance one, will be rejected by the CPC.

Precisely, this concept is strictly true of a ray that crosses the longitudinal axis of the CPC at the inlet. Other rays, can still be collected by the receiver even if their incidence angle is slightly different than the maximum one.
The overall intercept factor of each heliostat is represented by the bunch of rays that leave the i-mirror, that is not blocked by any other k-heliostat, that reach a perfect secondary reflector surface ($\rho_{SR} = 1$) and are reflected onto a specified receiver aperture. Among these rays, the ones collected by the receiver, have an incidence angle lower than the maximum one defined by the concentration ratio of the CPC and define the intercept performance.

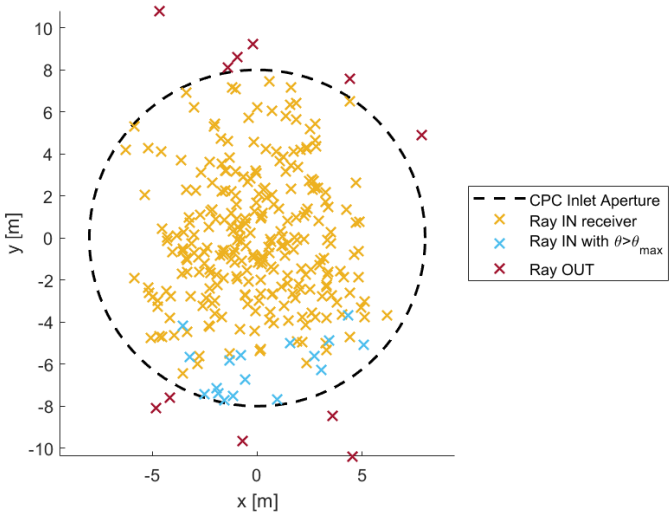

Figure 3.12: Intercept efficiency evaluation. Red cross fall outside of the CPC inlet radius. Light blue cross are rejected due to incidence angle higher than maximum one set by the CR of the CPC. Number of ray equal to 300.

3.2.5. Secondary reflector shadow

Another loss introduced by a beam down system with respect to a solar tower is the one relative to the shadow formed by the presence of a secondary reflector. This effect cannot be neglected, especially for a high value of eccentricity.
Defined a hyperboloid shape, the shadow performance of each i-heliostat has to be assessed to calculate the effective instant power of the field at a given sun position.
Given a solar position and a i-mirror with normal $\hat{\mathbf{n}}_\mathbf{i}$ such that the incidence sun vector, $\hat{\mathbf{s}}_\mathbf{i}$, is reflected towards the upper focal point, several rays are generated onto the inclined heliostat surface as presented before for the calculation of the intercept efficiency. Nevertheless, in this case, a part of the heliostats can be already shadowed or blocked

by other interfering heliostats. To do not overestimate the SR shadow performance, the random rays considered are only the ones laying on the free mirror surface, as shown in Figure 3.13.

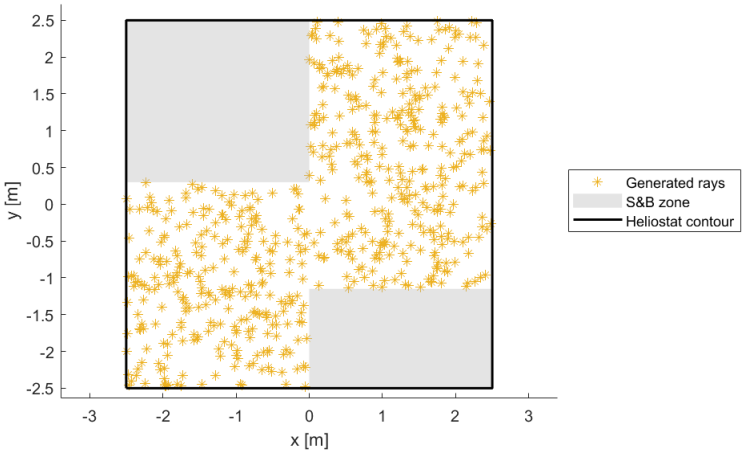

Figure 3.13: Random rays generation on heliostat free surface.

The randomly generated rays, with direction defined by $\hat{\mathbf{s}}_\mathbf{i}$ are then intersected with an infinite hyperboloid. The shadow performance is then evaluated as Equation 3.12.

$$\eta_{s,SR,i} = 1 - \frac{N_{in}}{N_{tot}} \tag{3.12}$$

Where N_{in} is the number of rays that fall inside the given hyperboloid shape while N_{tot} is the total number of rays generated on the heliostat surface.
In this case, with respect to intercept efficiency calculation, too high values of generated rays can sensibly increase the computational time without any accuracy improvement. Given a sun position, most of the field mirrors are either completely shadowed or not. Just a few of them have an efficiency which falls in a value between 0 and 1.
Nevertheless, in the selection of the number of rays, also the heliostat size is an important parameter. Even if the rays are generated randomly to follow a more probabilistic approach, the mirror area can divide into the same number of pieces and so the value of each ray can be directly referred to as a percentage of the heliostat surface obscured.

3.3. SR section creation

Nowadays existent beam down solar application makes us of a circular field of heliostat and so circular secondary reflector. To unconstrain the shape of the hyperboloid, the field is divided into sections.
A section is defined as a circular sector of the field bounded by two angles. Every k-section is then formed by J-rows that are the maximum number of rows present in a field bounded by a minimum and maximum radius. Every row of the field will be called a j-row, so every subsection can be defined by a combination (k, j).

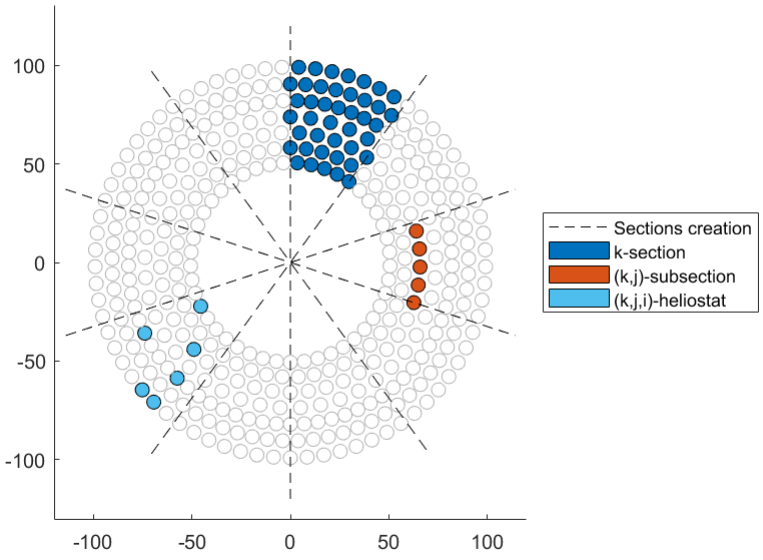

Figure 3.14: Section division methodology. Number of sections equal to 10.

The hyperboloid shape is difficult and computational expensive if it would be created considering heliostat by heliostat. This is mainly because neighbor mirrors share the same secondary reflector area, as shown in Figure 3.15. Following the circular approach, the section division allows to easily select circular sector of the field and so identify the relative secondary reflector radius and azimuth boundaries.
The user can then select the number of sections preferred. This number has to be even for field symmetry reason and, at maximum, the one that guarantees an azimuth difference equal to the one between two generic heliostats in the first row. The field is then divided into K-sections of equal azimuth range $360°/K$, starting from the north.
Each (k, j)-subsection has an efficiency equal to the mean one of the mirrors present in that subsection. A common j-row hyperboloid shape is considered, defined by a mini-

mum and maximum radius, r_j and R_j and azimuth angle extension, ΔAz. These three characteristics are obtained by the intercept factor calculation presented before. For each i-heliostat it's possible to assess a circular sector of the hyperboloid based on the minimum and maximum radius, $r_{k,j,i}$ and $R_{k,j,i}$, and the azimuth angle extension $\Delta Az_{k,j,i}$, from a random bunch of ray generated at the inclined heliostat surface. The $\Delta Az_{k,j,i}$ is evaluated considering an intercept of 99% at each side in order to avoid unjustified secondary reflector azimuthal extension.
For each (k, j)-subsection is then possible to evaluate $r_{k,j}$, $R_{k,j}$ and a $\Delta Az_{k,j}$ of the hyperboloid as the minimum and maximum values among all the I-heliostat present in the (k, j)-subsection.

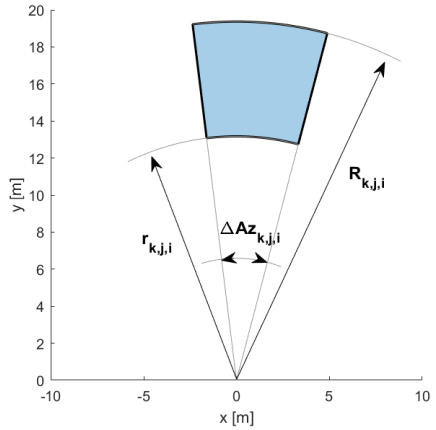

(a) Hyperboloid relative to the (k, j, i)-heliostat

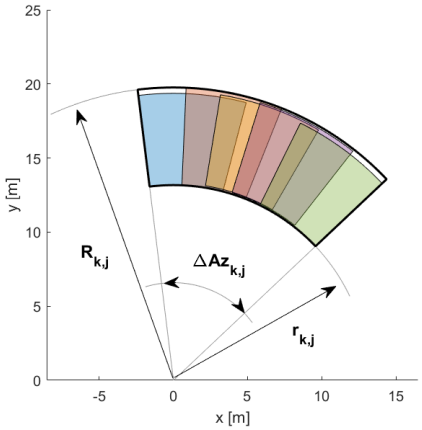

(b) Hyperboloid relative to the (k, j)-subsection

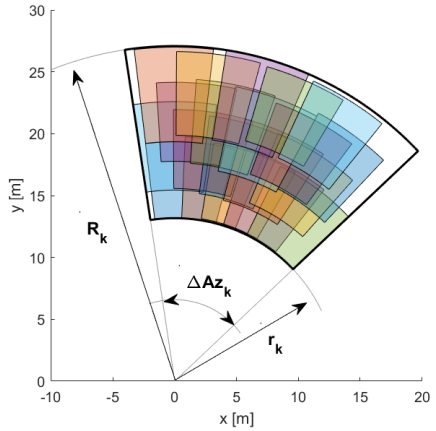

(c) Hyperboloid relative to the k-section

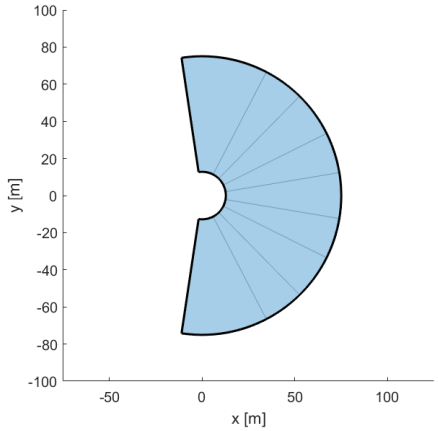

(d) Hyperboloid relative to the all $K/2$-sections

Figure 3.15: Secondary reflector construction methodology.

A common value of r_j and R_j is selected as the minimum and maximum radius found among all the K-section of a certain j-row of the field. The angle extension, on the other hand, is selected as the maximum one between all the $(K \cdot J)$-subsections.
The hyperboloid for each section is then defined by a circular sector bounded between two angles and with the radial extension defined by the rows present in the field.
The final secondary reflector shape is then the union of all the K circular sectors.
Selecting the right number of sections it's strictly related to the secondary reflector shape, but moreover to the heliostats related to that circular sector.
Let's consider a solar field of a minimum radius of 50 m and a maximum one equal to 800 m. As anticipated before the minimum number of sections will be equal to the number of heliostats in the first row, rounded to the lower even integer, while the minimum one is equal to two. In the ideal condition, the hyperboloid azimuth extension for each section will be $360/K$, with K the total number of sections.
In real optic behavior, sun, shape, and slope errors distort the aiming direction. Therefore, the real hyperboloid circular sector will be bigger, both in radius and azimuth extension. Nevertheless, the section division is completely useless if the hyperboloid found for one section overlaps completely with the one of the narrow section. In this case, the real azimuth extension will be 3 times the ideal one.
Figure 3.16 represent the ideal and real azimuth extension over the number of sections selected. The eccentricity is considered equal to 2, namely close to the minimum value of 1. The solution is conservative, since as eccentricity decreases the hyperboloid will be smaller but close to the aim point, so affected by higher optical error amplification.

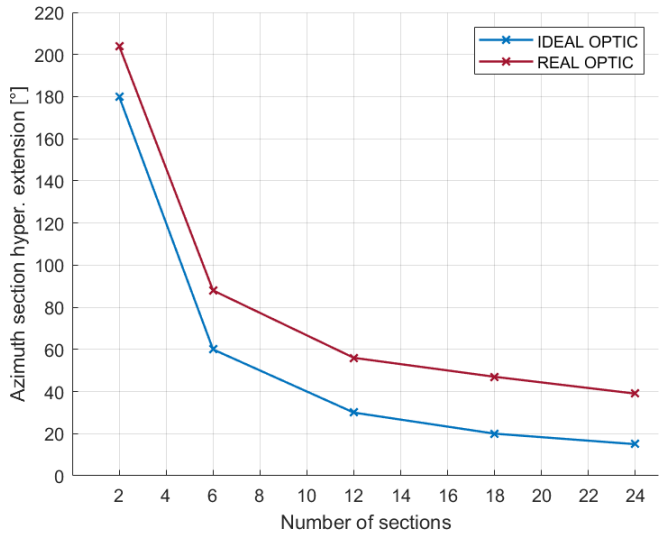

Figure 3.16: Secondary reflector real and ideal optic azimuth extension. Maximum field radius equal to 800 m. Eccentricity equal to 2.

At number of sections equal to 12, the real azimuth extension is almost double the ideal one. In this case, the azimuth of one section extends to the axis of symmetry of the narrow field section. At a higher number of sections, the hyperboloid of each section covers more than 50% the narrow one. As a good rule, the division in 12 slices can be a good compromise between secondary reflector heliostats density and accuracy of the simulation in terms of the number of heliostats selected, as it will be shown in section 3.4. Moreover, the azimuth extension found is strictly dependent from the minimum field radius chosen. Too low values, can sensibly reduce the possible number of sections, due to increased secondary reflector slice overlapping.

3.4. Design field performance

In the following paragraphs will be presented in detail how a beam down optic solar field at a given latitude and design condition is generated in Matlab.
The different inputs that the user can choose to obtain a specific solar field configuration are:

- **Latitude:** expressed in degree (North positive), represent the geographic location of the selected solar site.
- **Minimum and maximum field radius:** based on the available space of the selected solar site.
- **Design power:** instant power produced at solar noon by the solar field at the design day selected.
- **Design data:** expressed as design day chosen (summer solstice, equinox, winter solstice) and Direct Normal Irradiance (DNI).
- **Eccentricity:** secondary reflector geometric parameter.
- **Compound Parabolic Concentrator (CPC) geometry:** defined by a inlet radius (R_{cpc}) and a Concentration Ratio ($CR_{cpc,3D}$), if present.
- **Number of sections:** the field is divided into K even sections with azimuth extension equal to $360/K$.
- **Heliostat geometry:** dimension of rectangular heliostats in terms of width (WM) and height (HM).
- **Optical properties:** optical error considered for each stage (sun, slope and shape for heliostat, slope and shape for the secondary reflector).

The first task computed by the program is the radial staggered field layout between the minimum and maximum radius of the field selected. The sun position model utilized is presented in Appendix B.
It was decided to base the heliostats selection criteria on the annual DNI cosine efficiency multiplied by the intercept performance, considered constant along the year. Precisely, the annual cosine efficiency is DNI weighted on four days, namely the two equinox and the two solstices.
A more precise approach has to consider also the shadowing and blocking performance along the year of every mirror. Nevertheless, the S&B procedure is computational expensive and the use of DELSOLS3 radial spacing correlation guarantees to keep this value high, almost 95% at equinox noon, 99 % at summer noon [12].
The mirrors are then separated into subsections, so the mean heliostats efficiency (annual cosine and intercept) living in that subsection is utilized as a design criterion.
Moreover, the hyperboloid shape, as described before is found from the minimum and maximum secondary reflector radius found at each field row and the azimuth range equal to the maximum one found among all sections.
The first best efficient subsection is considered and inserted into the field. The subsection selection considers half of the field to obtain regularity on the final field layout and faster computational time. The efficiency of every subsection is homogenized with the correspondent mirrored one, for more accurate intercept performance evaluation.
Afterward, a while loop starts, selecting at every iteration the best efficient subsection till the design power is reached. Subsequently, the secondary reflector shape is created and the shadow efficiency for the pre-selected N-mirrors is performed, so a new field instant power as Equation 3.13.

$$\dot{W}_u = \sum_{i=1}^{N} \eta_{opt.i} \cdot A_{helio,i} \cdot DNI_{design} \tag{3.13}$$

If the latter is higher than the design one, the program performs the shadowing and blocking efficiency for each mirror, otherwise, the subsection selection continues.
Again, the new power is compared to the selected one and if the target is reached the program stop, otherwise the subsection selection continues. All the steps are summarized in Figure 3.18.
The selection of the number of sections used in the simulation directly affects the model accuracy. The minimum limit is defined by two sections, representing the two half of the solar site. The simulation proceeds row by row till the design power is exceeded.
Generally, more heliostats than the ones needed to reach the design target are selected,

worsening the model accuracy. On the other hand, the most precise configuration is the one that divides the field into the maximum number of sectors possible.
Nevertheless, as anticipated before in the section 3.3, a good sections division in terms of hyperboloid heliostats density can be the one of which its extension falls into the axis of symmetry of the neighbor section. However, the model correctness is strictly related to the nominal field power. At higher values, the field will be bigger, and also the number of heliostats placed at the latest iteration.

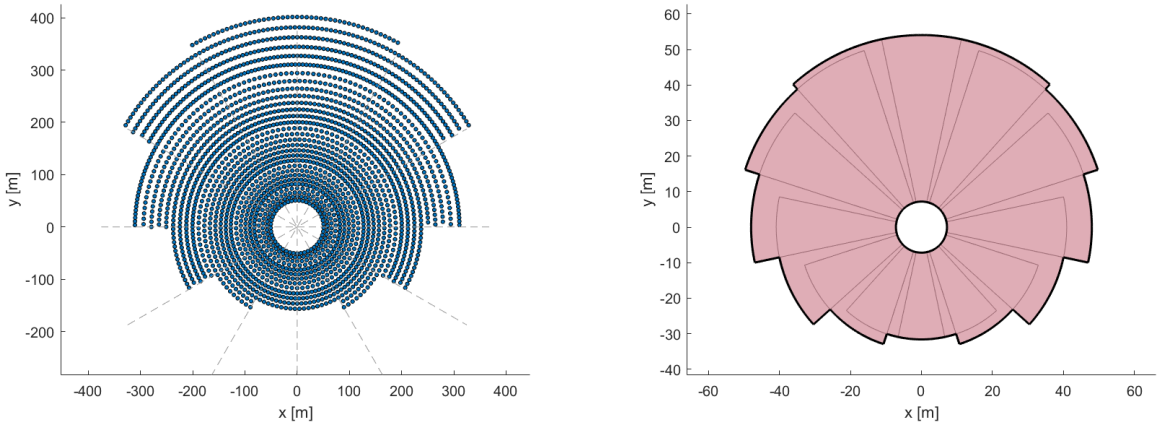

(a) Heliostats field

(b) Secondary reflector

Figure 3.17: 12 sections heliostats field creation. Latitude equal to 25°. Nominal power equal to 50 MW_{th} at the receiver aperture. Eccentricity equal to 2.

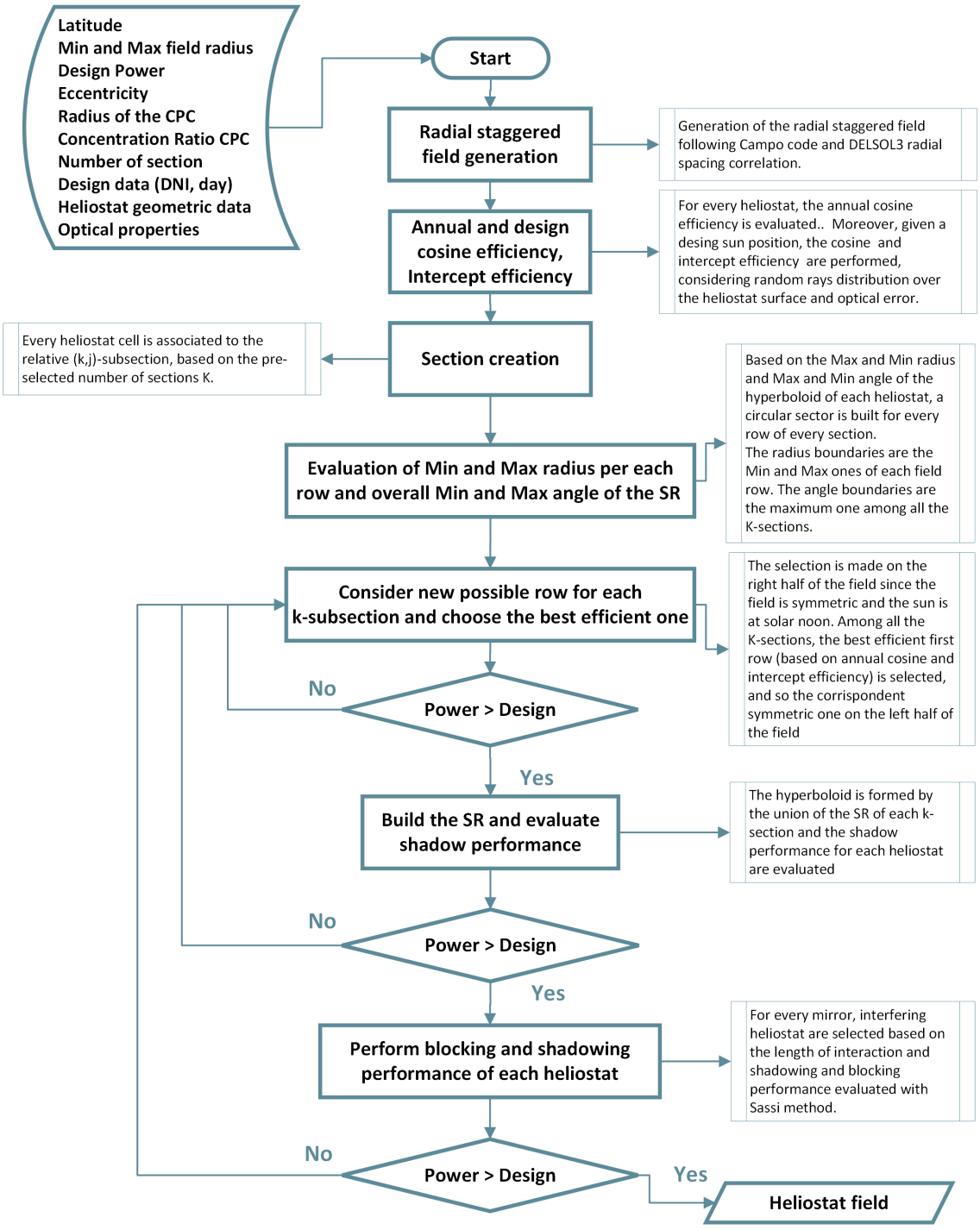

Figure 3.18: Flow chart of the field creation procedure.

3.5. Receiver thermal losses

In this section, a simplified receiver thermal model is presented. The ray path concludes at the receiver aperture where a Heat Transfer Fluid (HTF) is heated up and either stored or used as a hot source of a bottom power cycle.
The absorbed net flux at the receiver aperture is then the difference between the intercepted incoming radiation from the secondary reflector and the radiative and convective losses.

$$\dot{Q}_{net} = \dot{Q}_{sun} - \dot{Q}_{loss} \tag{3.14}$$

Where $\dot{Q}_{sun}$ is the intercepted radiation coming from the secondary reflector.
The Compound Parabolic Concentrator (CPC), if present, is considered a perfect reflector. If is not the case, a mutual receiver-CPC heat transfer takes place.
So, the radiative transfer will only consider the particles absorbed power, their emission, and reflection. It is assumed that the HTF act as a grey opaque body, with hemispherical emissivity and so absorptivity equal to 0.9 [51]. The radiative losses can be then evaluated as Equation 3.15.

$$\dot{Q}_{rad} = \varepsilon\sigma_{SB}(T_{rec}^4 - T_{sky}^4)A_{rec} + \rho\dot{Q}_{sun} \tag{3.15}$$

Where σ_{SB} is the Stefan-Boltzmann constant, A_{rec} the receiver area, T_{sky} the sky temperature which is assumed equal to the ambient one, and ρ the HTF reflectivity.
The convective loss is mainly gravity-driven since the wind is limited to reduce particle loss. The heat transfer coefficient is then proportional to the Grashof and Prandtl number product, so Rayleigh (Ra). For the upper side of hot horizontal plates, the averaged Nusselt can be found as Equation 3.16 [28].

$$\overline{Nu}_L = 0.14\ Ra_L^{1/3} \tag{3.16}$$

Where in this case the choice of the characteristic length L is indifferent since both Nu and $Ra^{1/3}$ are proportional to it. The convective loss is then evaluated as Equation 3.17.

$$\dot{Q}_{conv} = h(T_{rec} - T_{amb})A_{rec} \tag{3.17}$$

Where T_{amb} is the ambient temperature. Precisely, the receiver is generally positioned at the bottom of the CPC. Its shape won't be perfectly horizontal to guarantee particle flow.

Moreover, this approach is conservative since the buoyancy gravity-driven effect will be limited by the CPC quadratic cone shape. Furthermore, this model assumes that if the CPC is built on an array configuration, each tertiary concentrator has its receiver.
Finally, the thermal efficiency of the receiver is performed as Equation 3.18.

$$\eta_{th,rec} = \frac{\dot{Q}_{sun} - \dot{Q}_{rad} - \dot{Q}_{conv}}{\dot{Q}_{sun}} \tag{3.18}$$

At receiver temperature close to particles receiver (750 °C) applications, the radiative heat exchange dominates the thermal loss as shown in Figure 3.19. At constant receiver and ambient temperature the convective and the thermal loss increase quadratically with the CPC inlet radius. The convective heat transfer coefficient settles around values of 10 W/m^{2}K.

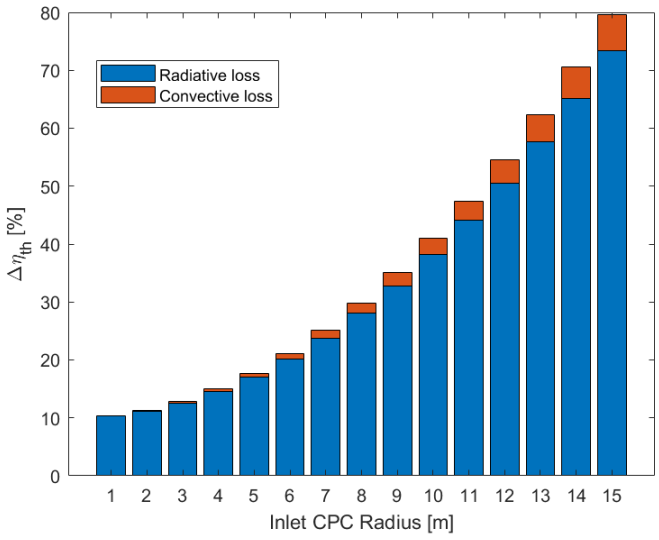

Figure 3.19: Thermal efficiency loss for a receiver temperature of 750 °C and ambient one equal to 25 °C. Inlet CPC radius varying from 1 to 15. CPC concentration ratio equal to 1.5. Particles emissivity equal to 0.9.

3.6. Annual system performance

A simple clear sky model is utilized to evaluate annual performances of a solar field. The DNI data are obtained thanks to Equation 3.19 [8].

$$DNI = I_0 \cdot 0.7^{AM^{0.678}} \tag{3.19}$$

Where $AM = 1/cos(\theta_z)$ is the Air Mass ratio with θ_z the zenith angle.
I_0 is the extraterrestrial radiation computed as:

$$I_0 = 1367.7 \cdot \left(1 + 0.033 \cdot \cos\left(\frac{360 \cdot D}{365}\right)\right) \tag{3.20}$$

With D the Julian day number of the year. Figure 3.20 represents the DNI distribution for three representative annual days.

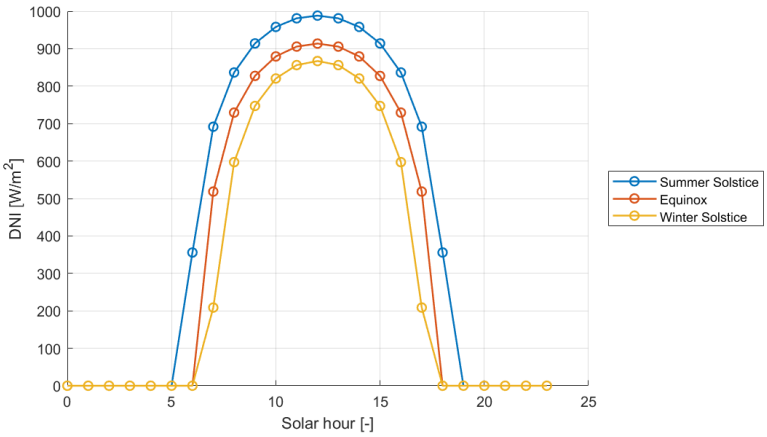

Figure 3.20: Clear sky DNI values at latitude equal to 25° N.

Considering every hour of the year, the annual field performance evaluation can be computationally expensive. Instead just a subset of hours can be simulated with sufficient accuracy [46]. For that reason, it was decided to simulate the field at every 15$^{\text{th}}$ of each month of the year. The day hours are selected such that the sun elevation (El) is higher than 15° [26].
The optical energy collected by the receiver at the 15$^{\text{th}}$ of the m-month is expressed as Equation 3.21.

$$W_m = \sum\nolimits_{t,El_t \geq 15°} \sum_{i=1}^{N} \left[\eta_{opt.i} \cdot A_{helio,i} \cdot DNI_t - \dot{Q}_{th,loss}\right] \tag{3.21}$$

Where t is the hour of the D-day, varying from 1 to 24, but considering only the ones with $El_t \geq 15°$.
Then the system annual efficiency $\eta_{ann,opt}$ can be evaluated as equation below.

$$\eta_{sys,ann} = \frac{\sum_{m=1}^{12} W_m}{\sum_{m=1}^{12} \sum_{t,El_t \geq 15°} DNI_t} \tag{3.22}$$

Same reasoning holds for a single heliostat, where the same procedure can be followed considering $W_{m,i}$ as the optical energy produced by the single mirror instead of W_m and so $\eta_{ann,opt,i}$ as Equation 3.22. Thermal loss is again neglected.
To obtain faster performance, the annual efficiency is evaluated over half of the field considering full secondary reflector shape. Since solar angles and DNI are symmetric along the day. The efficiency or the power at a certain hour, for half of the field, can be found as the average between the morning hour (a generic hour from midnight to noon) and its mirrored one in the afternoon, namely the one with the same elevation and opposite sign azimuth.
Moreover, following the ray path, each specific optical annual contribution can be found. Starting from the reflective losses, to the thermal ones, every specific optical efficiency is evaluated following Equation 3.22 but considering at the denominator the available energy at each step, as presented in Figure 3.21, so the product of each efficiency contribution will give the overall system efficiency.

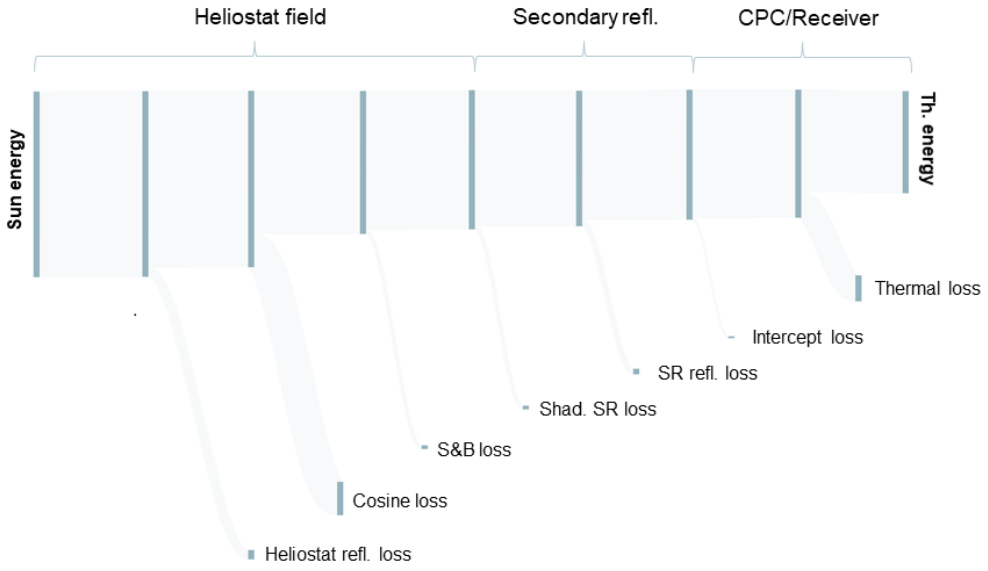

Figure 3.21: Sankey diagram of the optical and thermal energy path for point focus Beam-Down application.

3.7. Annual SR shadow optimization

In solar tower applications, different optimization can be made in terms of heliostats position in the field, tower height, or receiver size. Collado et al., proposed an annual optimized radial staggered field layout where a constant value of the radial distances between rows of the same zone is step by step increased till the maximum of annual efficiency is reached [14]. The main objective of the work is based on the consideration that, starting from a compressed field (no radial expansion between rows and zone), as the distance between two neighbor row is increased the shadowing and blocking efficiency will improve at the expense of lower cosine and attenuation ones.
The same consideration were utilized by Li et al., but the main objective of the optimization was the energy produced over the solar field cost at the design day chosen [26].
Besarati et al. proposed an annually optimized spiral heliostats field patterns inspired by the phyllotaxis disc following the same optimization methodology of Collado et al. [7].
Let's consider a surrounded solar field placed at 25° N of latitude, with a hyperboloid of eccentricity equal to 4 and maximum radius defined by an ideal optic.
The annual field hyperboloid shadow ($\eta_{s,SR,ann}$) and cosine ($\eta_{cos,ann}$) clear sky DNI weighted efficiency at ground level is presented in Figure 3.22.

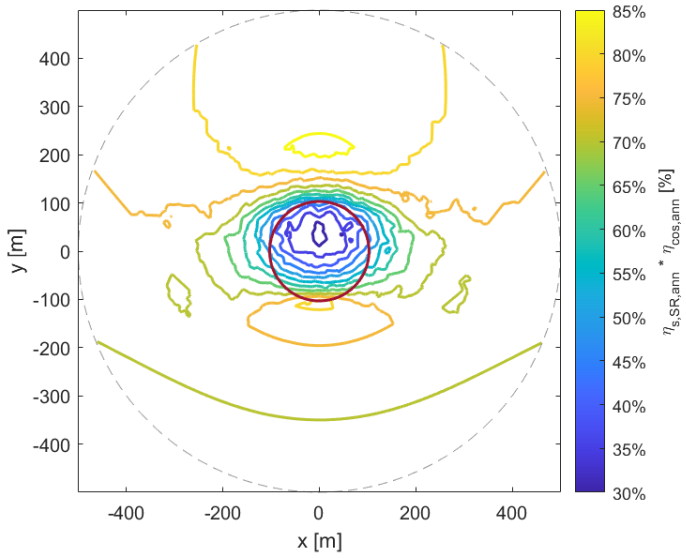

Figure 3.22: Annual clear sky DNI weighted cosine and secondary reflector shadow efficiency at ground level. Hyperboloid (red line) with eccentricity equal to 4 and radius equal to 100 m. Latitude of 25° N, aim point equal to 100 m, lower focus at ground level. Field radius equal to 500 m.

The inner field part reaches annual cosine and secondary reflector shadow efficiency below 40%. In this direction, a Matlab optimization procedure was built.
Starting from the design solar field created following the procedure explained section 3.4, the annual performance η_{ann} is evaluated. Subsequently, the best design efficient new possible (j, k)-subsection is considered. The selection is again made on the best averaged annual cosine and intercept performances.
Adding another subsection into the field can either increase or decrease the design power. The latter condition happens when the design power given by the new subsection does not compensate for the decreased one caused by the presence of a bigger secondary reflector. However, this condition is pretty rare. A new possible subsection slightly increases the secondary reflector radius in the direction of the section considered because neighbor heliostats share the same secondary reflector area. Moreover, heliostats are placed subsection by subsection, so the number of mirrors in farther rows is higher than the ones in the inner part of the field. Therefore, generally, the increased power brought by the new subsection is higher than the decreased one created by the bigger shadow effect.
Subsequently, the field is step by step thinned out, from the inner rows to the outward ones, of the worst annual efficient subsection till again the design power is reached.
The simulation is performed on half of the field for faster performances and symmetry in the final field pattern. The overall procedure is presented in Figure 3.23.
For every subsection elimination, the new heliostats field annual performance ($\eta_{ann,new}$) are evaluated and if its value is higher than the one of the base case (η_{ann}), a new optimum configuration is found. The latter is again analyzed for new possible subsections. The optimization stops when the best possible heliostat field is found.
Precisely, every new possible row of a section of the field has to be performed, because is not strictly true that adding the best design efficient one will improve the annual field performance. Every new insertion increases the hyperboloid size in the direction of the section chosen. The new circular sector can still get worse field performance if its shadow projection affects an existent good performing part of the field.
Nevertheless, after many simulations, it was found that even performing every new possible row of each section, the best design efficient ones will be selected.
As said before, building a new possible subsection, slightly increases the hyperboloid maximum radius in that direction and so the annual field performance is governed by the cosine and intercept effect.
The number of field sections division can sensibly affect the annual optimization outcome. A too high number can potentially increase the computational time without any accuracy improvement. On the other hand, a small value can immediately stop the optimization since the farthermost subsection introduces too high power.

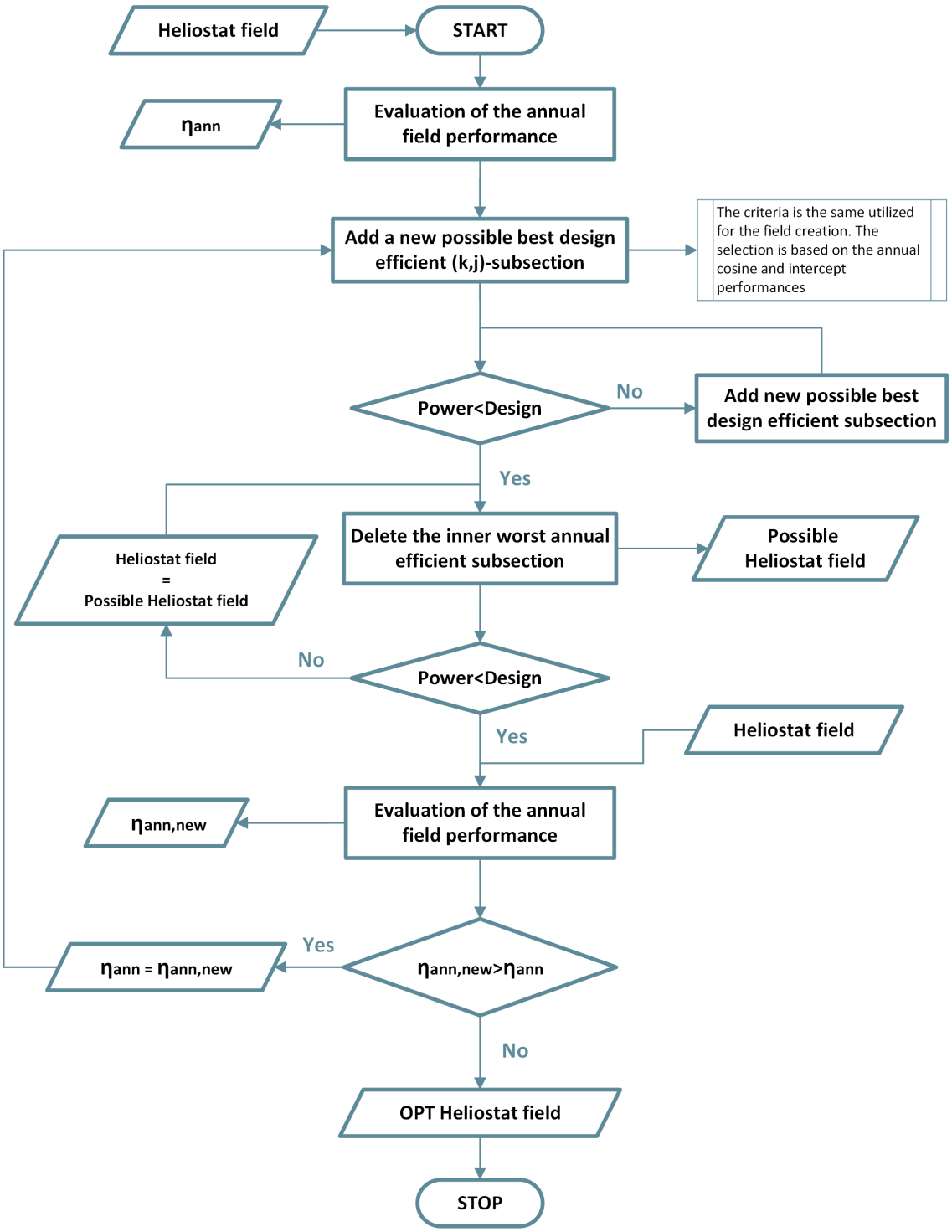

Figure 3.23: Flow chart of the field optimization procedure.

3.8. Design parameter sensitivity analysis

Selected the latitude of the solar site, the design condition (DNI, day, power), the optical and geometrical properties of each component, multiple parameters have to be considered in designing the best field configuration.
Aim point height, CPC geometry (if present or the receiver one), and receiver temperature cause efficiency variation of the solar system. The latter one is independent of the field shape, but it has a huge impact on the possible receiver aperture.
In the following section, it will be assumed that a CPC is present and so defined by its inlet radius, R_{cpc}, and its Concentration Ratio, $CR_{cpc,3D}$.
A first value for the latter two parameters has to be set to build a plausible solar field. Conceptually, the highest concentration ratio that can be reached, fixed an eccentricity, an aim point, and a lower focus, is the one of a circular field. Values higher than the latter cause very small intercept efficiency and so worse-performing field. These arguments are not strictly true when also the thermal efficiency of the receiver is considered. Lower inlet radius and higher $CR_{cpc,3D}$, and so higher thermal efficiencies, can govern the field performance.
In order to obtain a fast first value for the $CR_{cpc,3D}$ and the inlet radius of the CPC, a simplified version of the field creation was designed.

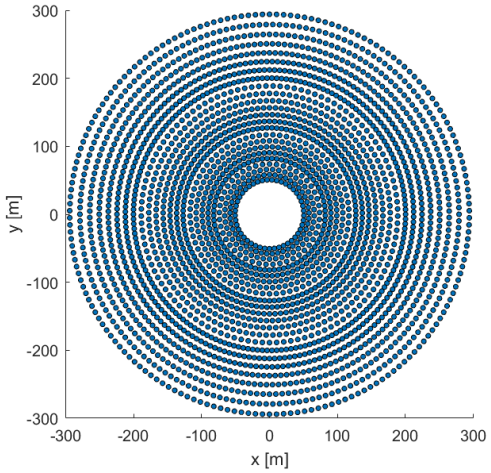

Figure 3.24: Simplified surrounded heliostats field. Solar site characteristic as Table 3.1.

The solar field is built row by row, as shown in Figure 3.24, till the design power is reached, considering the hyperboloid shadow effect. A surrounded field is then obtained following the solar site characteristic of Table 3.1.
The rays of each heliostat are then projected at the lower focus and the ground image

radius is found considering an intercept equal to 99 %. The value of spillage selected seems a reasonable assumption in terms of power collected since, as shown in Figure 3.25, the increased cumulative probability tends to flatten out after the identified radius, so limiting the thermal performances of the receiver without sensibly increasing the power collected.

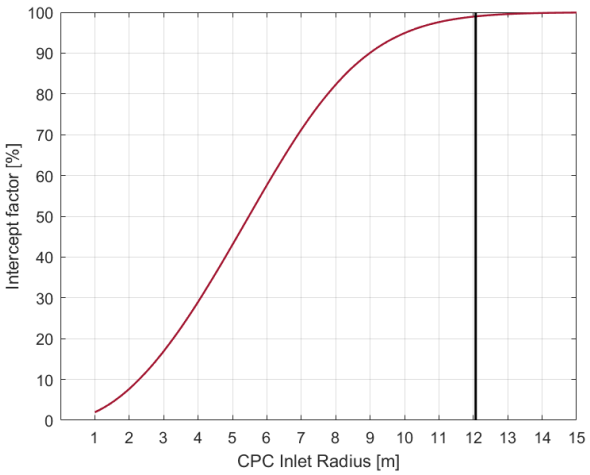

Figure 3.25: Intercept factor (red line) at CPC inlet radius varying from 1 to 15. Simulation with 2 million rays. Black line represents the identified radius (99% of intercept). Solar site parameters as Table 3.1.

Moreover, the CPC inlet radius is analysed also in terms of incidence ray inclination, as shown in Figure 3.26.

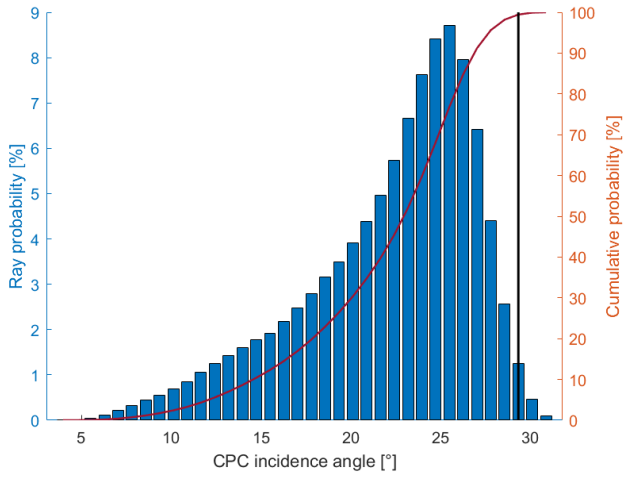

Figure 3.26: Rays incidence angle on receiver aperture. Simulation with 2 million rays. Incidence angle is defined from the longitudinal axis of the CPC. Black line represents the identified maximum acceptance angle. Solar site parameters as Table 3.1.

Just a few percentages of rays enter with the uppermost angle and so it was decided to set the maximum concentration ratio of the CPC as the one that intercepts the 99 % of total rays entering into the receiver aperture selected. The $CR_{cpc,3D}$ found was equal to 4.15 and the ground image radius equal to 11.2 m.

In the following subsection, the contribution of the geometry of the CPC, the aim point, and the eccentricity to the field shape and performance is assessed. Annual efficiencies are DNI weighted on 12 days, precisely the 15th of each month.
In Table 3.1, all the constant parameters utilized in the following considerations and their values, are summarized.

Latitude	25° N
Design Power	50 MW at the receiver aperture
Min. Field Radius	50 m
Max. Field Radius	800 m
Aim point height	100 m
Lower focus height	15 m
Number of sections	12
Design DNI	1 kW/m^{2}K
Heliostat	Rectangular 5x5 m Reflectivity = 0.95
Secondary reflector	Hyperbolic shape Eccentricity = 2 Reflectivity = 0.9
CPC	Reflectivity = 1
Optical error	Sun error = 4.1 mrad Slope error = 0.95 mrad Spec. error = 0.2 mrad
Receiver	Grey body Emissivity = 0.85 Conv. HT coeff = 10 W/m^{2}K
Ambient temperature	30 °C
Intercept rays number	300 per heliostat
SR shadow rays number	100 per heliostat

Table 3.1: Solar site input parameters.

CPC Concentration ratio

The tertiary concentrator geometry sensibly affects the field shape and performance. More precisely, the most influenced factors are the intercept, the cosines effect, and the thermal efficiency of the receiver at a given temperature.
We have seen as annual cosine efficiency influence the field shape based on the solar site location. Heliostats fields placed at the northern hemisphere generally have a more asymmetric, North oriented, shape, mainly caused by better cosines. On the other hand, the farther will be the mirror distance from the aim point, the higher will be its incidence angle on the receiver aperture.
Let's now consider two different receiver temperatures: 600 °C and 1000 °C and three different Concentration Ratio ($CR_{cpc,3D}$) of the CPC, 3.9, 4.15 (base case), and 4.40. The receiver temperatures are selected as two different limiting values, respectively for molten salts and particle heat transfer fluid [33].
The radius of the CPC is selected equal to 11.2 m, namely the one found in the surrounded simplified configuration.
The annual optical field efficiencies obtained and the number of heliostats (#Helio) selected, are presented in Table 3.2.

$CR_{cpc,3D}$ [-]	θ_{max} [°]	$\eta_{opt,ann}$ [%]	$\eta_{cos,ann}$ [%]	$\eta_{sb,ann}$ [%]	$\eta_{s,SR,ann}$ [%]	η_{int} [%]	#Helio
3.90	30.42	68.84	82.00	97.91	96.70	98.26	2650
4.15	29.40	68.19	81.28	97.95	96.79	97.93	2644
4.40	28.47	66.51	80.90	97.98	96.84	96.01	2687

Table 3.2: Annual optical efficiency for CPC inlet radius of 11.2 m and $CR_{cpc,3D}$ of 3.90, 4.15 and 4.40. Solar field parameters as Table 3.1.

The receiver temperature does not change the field shape, since the design power is considered at the receiver aperture.
On the other hand, the CR variation, as presented before, influences the solar site arrangement, as shown in Figure 3.27. At a lower $CR_{cpc,3D}$ value the field creation script pushes for more cosine efficient mirrors selection and the field shape becomes more asymmetric. The annual DNI weighted cosine effect slightly increase, passing from 81.28% to 82%. On the other hand, the number of heliostats follows the same trend due to farther positioning, passing from 2650 to 2644.

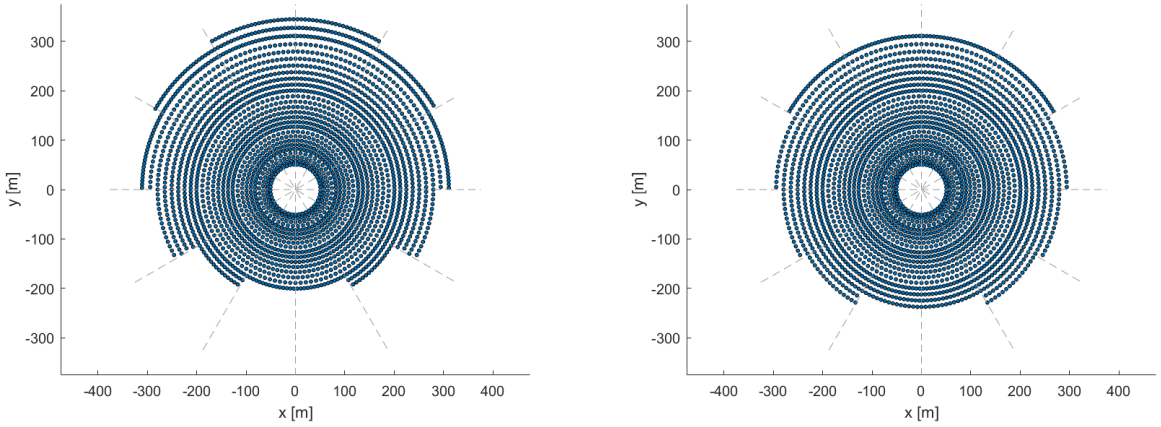

(a) $CR_{cpc,3D}$ = 3.90, R_{cpc} = 11.2 m (b) $CR_{cpc,3D}$ = 4.15, R_{cpc} = 11.2 m

Figure 3.27: Field shape for CPC $CR_{cpc,3D}$ equal to 3.9 (left) and 4.15 (right) and same inlet radius of 11.2 m. Solar site parameter as Table 3.1.

The intercept follows the same trend, slightly increasing from 97.92% to 98.26%. Although, as presented in Table 3.3, the annual thermal efficiency slightly decreases, passing from 91.88% to 91.48% at T_{rec} = 600 °C.

$\eta_{th,ann}$ [%]	$CR_{cpc,3D}$ [-]		
	3.90	**4.15**	**4.40**
T_{rec} = **600 °C**	91.48	91.88	92.98
T_{rec} = **1000 °C**	65.29	66.92	68.62

$\eta_{sys,ann}$ [%]	$CR_{cpc,3D}$ [-]		
	3.90	**4.15**	**4.40**
T_{rec} = **600 °C**	62.98	62.57	61.37
T_{rec} = **1000 °C**	44.95	45.57	45.64

Table 3.3: Annual thermal and system efficiency for CPC inlet radius of 11.2 m and $CR_{cpc,3D}$ of 3.90, 4.15 and 4.40. $\eta_{sys,ann}$ is the product between $\eta_{opt,ann}$ and $\eta_{th,ann}$. Solar field parameters as Table 3.1.

On the other hand, at higher receiver temperature, T_{rec} = 1000 °C, the higher optical performance are not compensated by a decrease in the thermal efficiency, that pass and from 66.92% to 65.29%, lowering the overall solar site annual η_{ann} performance of 0.7 % relative, as presented in Table 3.3.
An increase in the $CR_{cpc,3D}$, from 4.15 to 4.40, directly affects the intercept efficiency that moves from 97.93% to 96.01%. At T_{rec} = 600 °C, the lower intercept does not compensate the 1.2% relative thermal efficiency increase. That's not the case for higher receiver temperature where the annual system performance is almost constant, passing from 45.57% to 45.64%, as a trade-off between the lower cosine efficiency and increased thermal efficiency that passes from 66.92% to 68.62%. Nevertheless, a higher concentration ratio slightly

increases the number of heliostats, due to lower intercept efficiency.
The annual secondary reflector shadow performances and the heliostats shading and blocking ones reach values higher than 95% in every configuration.

CPC Inlet Radius

The CPC inlet radius is the second parameter that completely defines a CPC geometry. Lowering the inlet radius of the CPC follows the same consideration made in the previous subsection for higher $CR_{cpc,3D}$. The performance of the field decreases in favor of better thermal behavior.
On the other hand, pushing for a bigger inlet radius, increase the intercept and cosine efficiency of the field. The first one is of pretty easy understating, higher radius can collect more rays at a given field. The second is strictly related to the heliostat's position.
As explained before, asymmetrically oriented configuration favors better cosine efficiency. Nevertheless, the heliostats are placed farther from the aim point and the intercept factor will diminish at the same receiver aperture due to optic error amplification.
The main constraint regarding the minimum possible receiver aperture radius, namely the outlet CPC radius, is governed by the maximum heat flux. Due to the degradation effect, for particle receiver technology, a maximum value of 3 MW/m^2 has been set for ceramic material. However the thermal flux distribution is not uniform and so a maximum peak flux of 2 MW/m^2 is considered [39]. So, the minimum inlet aperture radius R_{min} of the CPC, is related to the minimum exit one $r_{flux,lim}$, namely the one of the receiver, by Equation 3.23.

$$R_{cpc,min} = r_{flux,lim} \cdot \sqrt{CR_{cpc,3D}} \tag{3.23}$$

Let's consider again two receivers at different temperatures, a fixed concentration ratio of the CPC equal to the one of the simplified circular surrounded field ($CR_{cpc,3D} = 4.15$) and inlet aperture radius equal to 10.7 m, 11.2 m (base case), and 11.7 m.
Results regarding the annual optical efficiencies and the number of heliostats (#Helio) selected are presented in Table 3.4. The annual thermal and system efficiencies at different receiver temperatures is presented in Table 3.5.

$\mathbf{R_{cpc}}$ [m]	$\eta_{\mathbf{opt,ann}}$ [%]	$\eta_{\mathbf{cos,ann}}$ [%]	$\eta_{\mathbf{sb,ann}}$ [%]	$\eta_{\mathbf{s,SR,ann}}$ [%]	$\eta_{\mathbf{int}}$ [%]	#Helio
10.7	67.85	81.27	97.94	96.84	97.55	2644
11.2	68.19	81.28	97.95	96.79	97.93	2644
11.7	68.39	81.40	97.94	96.80	98.20	2614

Table 3.4: Annual optical efficiencies for $CR_{cpc,3D}$ of 4.15 and R_{cpc} of 10.7, 11.2 and 11.7 m. Solar field parameters as Table 3.1.

$\eta_{\mathbf{th,ann}}$ [%]	$\mathbf{R_{cpc}}$ [m]		
	10.7	**11.2**	**11.7**
$\mathbf{T_{rec}}$ **= 600 °C**	92.56	91.88	91.07
$\mathbf{T_{rec}}$ **= 1000 °C**	69.68	66.92	63.63

$\eta_{\mathbf{sys,ann}}$ [%]	$\mathbf{R_{cpc}}$ [m]		
	10.7	**11.2**	**11.7**
$\mathbf{T_{rec}}$ **= 600 °C**	62.80	62.57	62.28
$\mathbf{T_{rec}}$ **= 1000 °C**	47.28	45.57	43.52

Table 3.5: Annual thermal and system efficiency for $CR_{cpc,3D}$ of 4.15 and R_{cpc} of 10.7, 11.2 and 11.7 m. $\eta_{sys,ann}$ is the product between $\eta_{opt,ann}$ and $\eta_{th,ann}$. Solar field parameters as Table 3.1.

At the same concentration ratio of the CPC, decreasing the radius at a constant temperature, slightly affect the intercept performance. This value passes from 97.93% at a radius equal to 11.2 m, to 97.55% at a radius equal to 10.7 m. Nevertheless the annual system efficiency marginally increases, from 62.57% to 62.80%, governed by a 0.7% relative thermal performance growth at T_{rec} = 600 °C. At higher receiver temperature this trend is even marked, with a relative increase of 3.8% in the annual field performances concerning the 11.2 m configuration, mainly governed by a 4.5% relative increase in the thermal efficiency.
Actually, in both configurations, the same heliostats field is selected, namely the one in Figure 3.27a. This can be related to a relatively small inlet radius variation into the simulation and loss of accuracy caused by the field section division methodology.
Higher CPC inlet radius slightly increases the intercept and cosine efficiency. On the other hand, the thermal performances decrease and govern the system's annual performance. Moreover, the field shape doesn't change with respect to the one of Figure 3.27b, but fewer heliostats are selected due to slightly higher intercept performance.

Aim point

Aim point increases favors of better field cosines and so higher efficiency. Following the simplified surrounded field approach, for every aim point will exist a starting value for the concentration ratio and the inlet radius of the CPC, as represented in Table 3.6.

Aim Point [m]	**80**	**100**	**120**
R_{cpc} [m]	11.2	11.2	11.5
$CR_{cpc,3D}$ [-]	3.50	4.15	4.95

Table 3.6: Simplified surrounded field configuration CPC geometry at different aim point height. Solar field parameters as Table 3.1.

Lowering the aim point, reduces the system focal distance and so the one of the secondary reflector. The hyperboloid will be squeezed to a lower altitude and the average ray incidence angle on the CPC aperture will increase. For that reason, the CR of the CPC decreases to a value of 3.50 for an aim point equal to 80 m. The inlet radius of the CPC doesn't change, even if the ray path slightly decreases due to lower aim point height.
Same, but opposite, reasoning can be made for an aim point equal to 120 m. In this case, the inlet radius of the CPC slightly increase to 11.5 m, due to optical error amplification. Their value will be here utilized to study how the aim point variation affects the field shape and performances. Moreover, the analysis is performed considering a receiver temperature of T_{rec} = 750°C, namely the current technology limit for particle receivers [33].

AP [m]	$\eta_{opt,ann}$ [%]	$\eta_{sys,ann}$ [%]	$\eta_{cos,ann}$ [%]	$\eta_{sb,ann}$ [%]	$\eta_{s,SR,ann}$ [%]	η_{int} [%]	**#Helio [-]**
80	66.57	55.21	79.19	97.90	97.50	97.58	2733
100	68.10	58.21	81.28	97.95	96.79	97.93	2644
120	69.23	60.23	82.84	97.84	96.40	98.17	2557

Table 3.7: Annual optical efficiencies for aim point (AP) equal to 80 m, 100 m and 120 m. CPC geometry defined by the simplified surrounded configuration. Solar field parameters as Table 3.1.

Lowering or increasing the aim point from the configuration selected affect also the heliostat position in the field. As shown in Figure 3.28, at lower aim point, heliostats are more affected by shadowing and blocking losses and so the DELSOL3 correlation tends to increases the radial distance between rows.

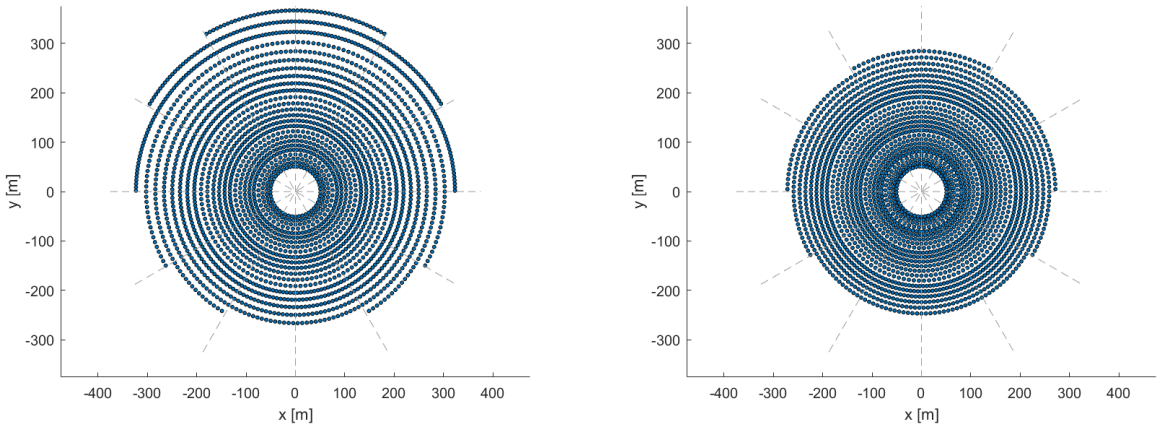

(a) Aim point = 80 m (b) Aim point = 120 m

Figure 3.28: Field shape for aim point equal to 80 m (left) and 120 m (right). CPC geometry as Table 3.6. Solar site parameter as Table 3.1.

Moreover, pushing for higher aim points increases the annual DNI weighted cosine efficiency that passes from 81.28% at aim point equal to 100 m to 82.84% at aim point equal to 120 m. The higher concentration ratio of the CPC of the latter configuration also helps reach higher thermal performance. Overall the annual field efficiency increased by almost 3.5% in relative terms with respect to the base configuration.
The hyperboloid shadow efficiency slightly decrease caused by a more compact field pattern at an almost constant hyperboloid radius.
The opposite trend is followed by a decrease in the aim point height. Moving from 100 m to 80 m, the cosine annual efficiency reduces by 2.6% in relative terms and even higher variation is attained by the thermal efficiency that passes from 85.48% to 82.94% at same receiver temperature, mainly governed by a lower CR of the CPC.

Eccentricity

The previous section has analyzed how the geometry of the CPC and the aim point affect the field shape and the performance of a solar site. The eccentricity was kept constant and equal to 2, for every configuration.
As described in the first chapter, the value that can uniquely characterize a hyperboloid shape is eccentricity. As eccentricity increases, the secondary reflector crushes to half of the focal distance. The radius increase to catch the same amount of radius, but on the other hand, the area of the surface decrease at the same field radius, and the same trend is also followed by the installation height at the fixed aim point. Moreover, the ground

image will be smaller due to lower error amplification. Nevertheless, the maximum acceptance angle at the receiver aperture is higher, so a lower concentration ratio of the CPC can be achieved.
The values of the CPC geometry obtained by the simplified surrounded configuration for 6 different eccentricities are listed in Table 3.8.

e [-]	**1.5**	**2**	**2.5**	**3**	**3.5**	**4**
$\mathbf{R_{cpc}}$ **[m]**	18.2	11.2	9.2	8.4	8.0	8.1
$\mathbf{CR_{cpc,3D}}$ **[-]**	6.92	4.15	2.90	2.35	1.80	1.75

Table 3.8: Simplified surrounded field configuration CPC geometry at eccentricity varying from 1.5 to 4. Solar field parameters as Table 3.1.

It's interesting to notice that at eccentricity equal to 4, although the $CR_{cpc,3D}$ is still decreasing, the inlet radius value settles. This can be considered as a good threshold for the hyperboloid shape simulation range since the thermal efficiency will continue to decrease due to lower $CR_{cpc,3D}$ and constant inlet radius.
Moreover, at the same design power, a bigger eccentricity will cause a bigger field due to a non-negligible secondary reflector shadow effect.
The annual field optimization is performed for every configuration of Table 3.8, and the results are presented in Figure 3.29.

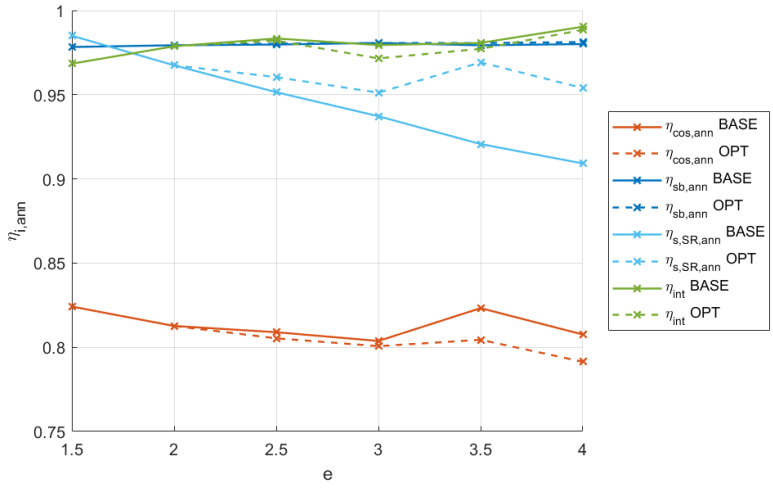

Figure 3.29: Base and annual shadow optimized field configuration at eccentricity from 1.5 to 4. CPC geometry as Table 3.8. Solar field parameters as Table 3.1.

From Figure 3.29, it's noticeable how the shadow hyperboloid efficiency sensibly increases in the optimized configuration, especially for high eccentricity. On the other hand, farther heliostats are selected and for that reason the cosine and the intercept efficiency slightly reduce.
The annual optical efficiency, as presented in Table 3.9, can be increased up to 2%.

$\eta_{\mathbf{opt,ann}}$ [%]	**e [-]**					
	1.5	**2**	**2.5**	**3**	**3.5**	**4**
BASE conf.	69.41	68.01	66.93	65.30	65.70	64.3
OPT conf.	69.41	68.44	67.85	67.10	66.50	64.71

Table 3.9: Annual optical efficiency for simplified surrounded field configuration (BASE) and annual shadow optimized one (OPT). CPC geometry as Table 3.8. Solar field parameters as Table 3.1.

Furthermore, in the optimized configuration, as shown in Figure 3.30, the secondary reflector area is reduced, due to the selection of farther heliostats, following the ratio decrease of the hyperboloid area over the field one presented in the previous chapter.

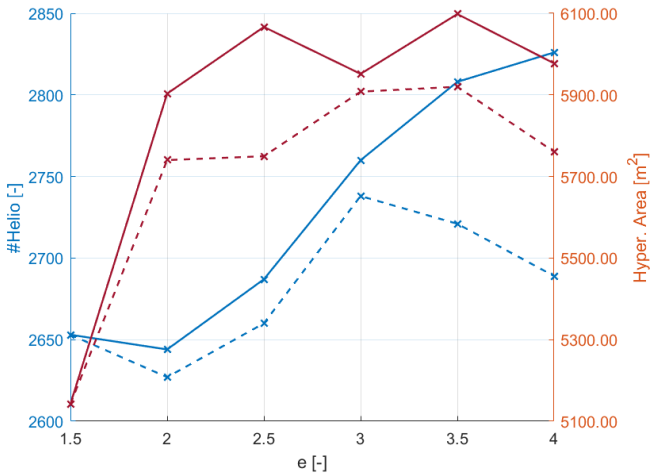

Figure 3.30: Heliostats number and hyperboloid area for the simplified surrounded configuration (BASE) and annual shadow optimized one (OPT). CPC geometry as Table 3.8. Solar field parameters as Table 3.1.

At high eccentricity values, the hyperboloid shadow almost cancels the annual optical performance of the nearest heliostats. Being deleted, their power, almost zero, is replaced just by a few other heliostats. So, the overall final optimized heliostats count is reduced. The previous results are influenced by the CPC geometry selected. As shown in Figure 3.31, the CPC radius and mainly the concentration ratio of the surrounded simplified configuration are blocking the selection of possible new outer heliostats.

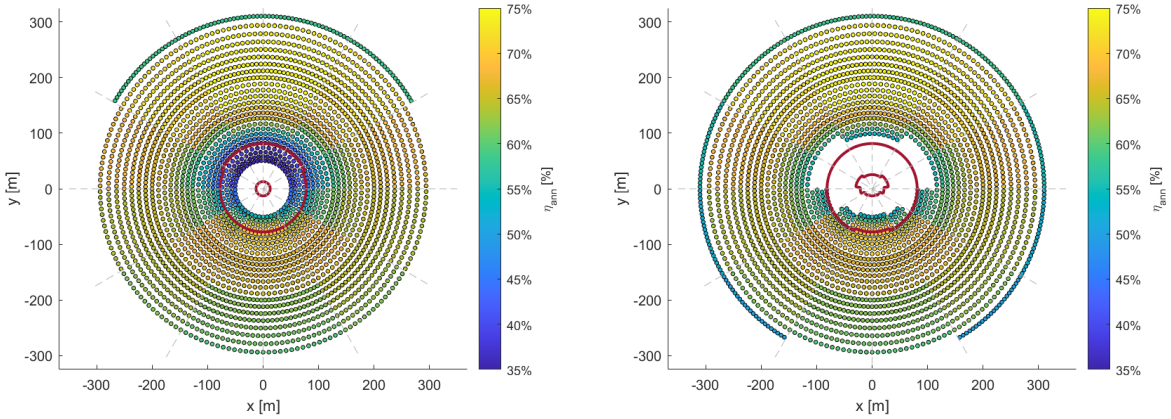

(a) Base configuration.

(b) Optimized configuration.

Figure 3.31: Annual field performance for the base and optimized configuration. Eccentricity equal to 4. CPC geometry as Table 3.8. Solar field parameters as Table 3.1.

3.9. Annual system optimization

It's clear that exist an optimum of every of the pre-mentioned configuration that maximizes the annual efficiency of the field. As summarized in Figure 3.32, the best solution will be a compromise between the CPC geometry and the field shape. A smoother CPC will increase the cosine and intercept performances of the field while, on the other hand, worsening the thermal performance.

Moreover, at higher eccentricity, the annual shadow optimization brings an important role in increasing the system performance and it's again governed by the CPC geometry.

So, in order to find the best configuration, an optimization methodology was built.

For every eccentricity, the starting value for the CPC geometry was considered equal to the one given by the simplified surrounded circular configuration.

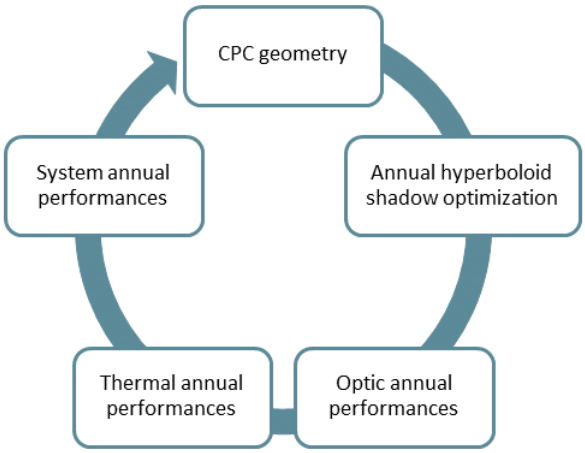

Figure 3.32: Methodology concept for the heliostats field optimization.

Then the base tertiary concentrator geometry is varied, reducing and increasing the starting values of both $CR_{cpc,3D}$ and inlet radius by a selected interval dimension. A 3x3 matrix is then created, where each row corresponds to an inlet CPC radius, R, and each column to a CR, as shown in Figure 3.33.
The center position of the matrix is occupied by the base configuration, found in the simplified surrounded field creation.

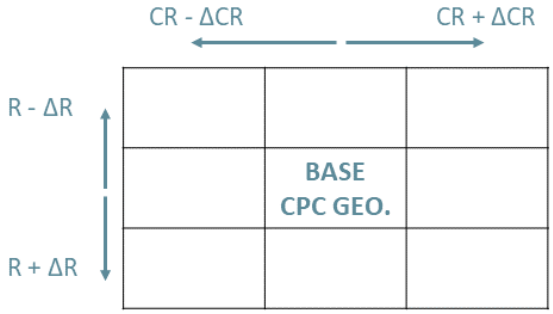

Figure 3.33: Starting matrix for the optimization procedure. The middle cell is occupied by the values found in the simplify surrounded configuration.

The inlet radius value of each CPC geometry is constrained between the minimum allowed by thermal flux limit on the receiver aperture and the maximum one identified by a zero thermal efficiency. Moreover, the CPC concentration ratio cannot go below 1. If a cell departs from these limits, its simulation won't be performed.
For every configuration, the annual optimization is carried out and the best efficient one

is selected. The matrix is then translated with the center in the best geometry found and new possible arrangements are identified.

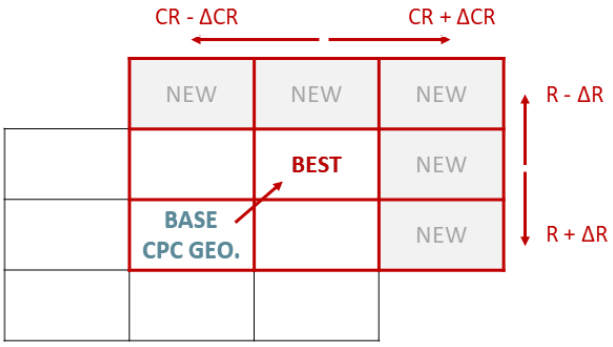

Figure 3.34: Iteration matrix for the optimization procedure.

If the new best configuration varies both in terms of inlet radius and CR, five new possible geometries are found and evaluated at the second iteration, as shown in Figure 3.34. If one of the two CPC geometry parameters doesn't change in the new configuration with respect to the base one, just three new possible designs are performed. The optimization continues till the annual best system efficient configuration is found in the center of a N-iteration matrix, as shown in Figure 3.35.

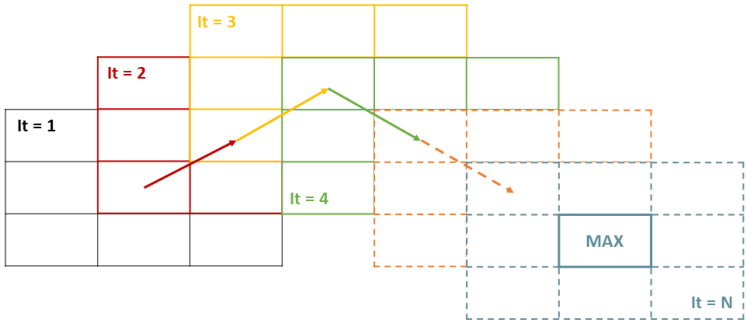

Figure 3.35: Overall iteration matrices for the optimization procedure.

The optimization procedure was performed for two different aim point heights and with a fixed receiver temperature equal to 750 °C. The final results are presented in the following pages. However, the methodology presented is a simplification since a local maximum can immediately stop the optimization process. Nevertheless, it is expected that the best-performing configuration will be close to the circular surrounded field one. On the other hand, performing every possible CPC geometry can sensibly increase the computational time.

Aim Point = 100 m

e [-]	Conf.	R_{cpc} [m]	$CR_{cpc,3D}$ [-]	$\eta_{sys,des}$ [%]	$\eta_{opt,ann}$ [%]	$\eta_{sys,ann}$ [%]	#Helio [-]	Area SR [m²]
1.5	BASE	18.2	6.90	61.96	69.42	53.82	2644	5340.37
	OPT	15.7	6.17	63.55	68.67	56.44	2685	5290.92
2	BASE	11.2	4.15	67.76	68.02	58.19	2644	6363.03
	OPT	10.2	3.65	66.92	68.45	59.32	2685	5619.07
2.5	BASE	9.2	2.90	66.64	66.93	57.51	2687	6656.96
	OPT	8.7	2.65	66.67	67.85	58.68	2692	5853.10
3	BASE	8.4	2.35	64.77	65.30	55.94	2760	6935.82
	OPT	7.9	2.10	65.52	67.11	57.74	2724	6030.26
3.5	BASE	8.0	1.80	61.82	65.70	54.76	2808	6112.48
	OPT	7.5	1.55	62.92	66.50	55.09	2754	6047.85
4	BASE	8.1	1.75	61.12	64.32	52.86	2826	6282.91
	OPT	7.1	1.75	65.20	64.71	55.63	2740	6379.76

Table 3.10: Base and optimized configuration main parameters results at aim point equal to 100 m. e is the eccentricity. $\eta_{sys,ann}$ is the product between $\eta_{opt,ann}$ and $\eta_{th,ann}$. T_{rec} equal to 750 °C. Solar field parameters as Table 3.1.

e [-]	Conf.	ρ_{helio} [%]	$\eta_{cos,ann}$ [%]	$\eta_{sb,ann}$ [%]	$\eta_{s,SR,ann}$ [%]	ρ_{SR} [%]	$\eta_{int,ann}$ [%]	$\eta_{th,ann}$ [%]
1.5	BASE	95.00	82.42	97.83	98.50	95.00	96.84	77.53
	OPT	95.00	82.43	97.89	98.48	95.00	95.75	82.19
2	BASE	95.00	81.27	97.94	96.75	95.00	97.88	85.56
	OPT	95.00	82.07	97.96	97.40	95.00	96.85	86.67
2.5	BASE	95.00	80.90	97.98	95.15	95.00	98.34	85.93
	OPT	95.00	81.26	98.00	97.04	95.00	97.28	86.48
3	BASE	95.00	80.38	98.07	93.72	95.00	97.95	85.65
	OPT	95.00	80.76	98.01	96.85	95.00	97.00	86.05
3.5	BASE	95.00	82.33	97.93	92.07	95.00	98.07	83.34
	OPT	95.00	80.74	98.04	96.49	95.00	96.36	85.26
4	BASE	95.00	80.76	98.00	90.92	95.00	99.04	82.17
	OPT	95.00	79.28	98.12	94.84	95.00	97.18	85.97

Table 3.11: Base and optimized configuration efficiencies at aim point equal to 100 m. e is the eccentricity. T_{rec} equal to 750 °C. Solar field parameters as Table 3.1.

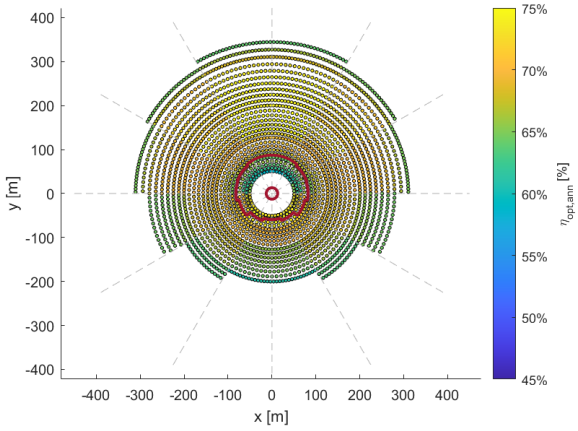

(a) Base configuration, e = 2

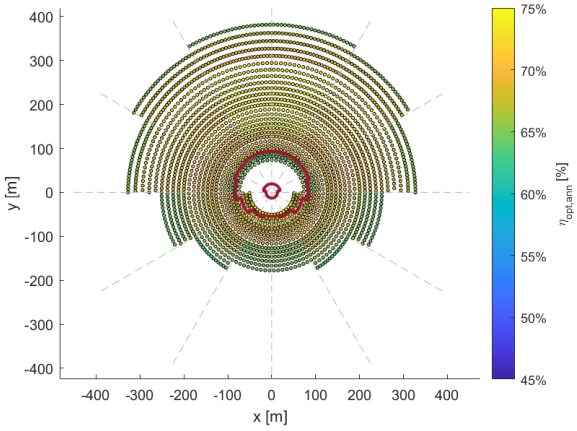

(b) Opt. configuration, e = 2

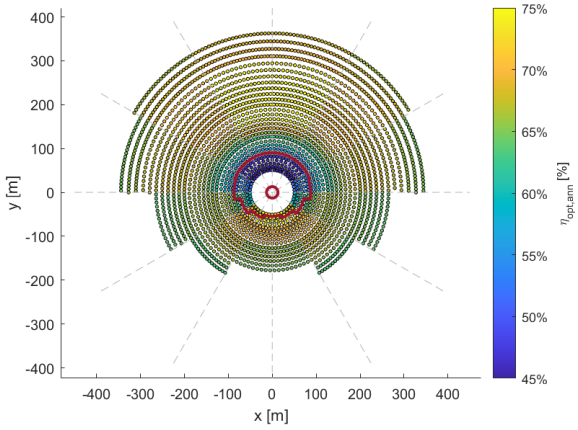

(c) Base configuration, e = 3

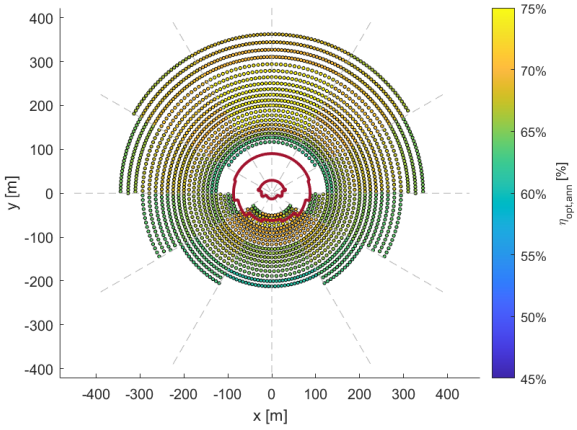

(d) Opt. configuration, e = 3

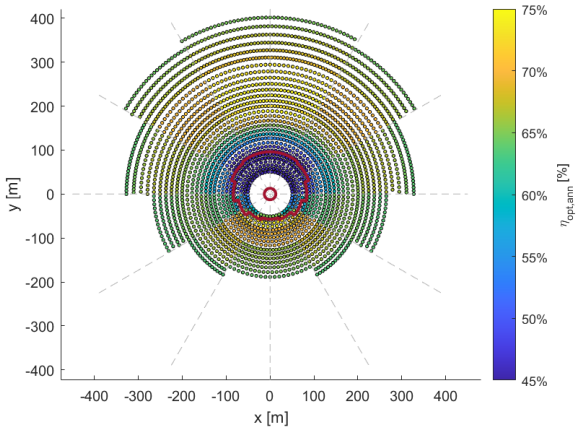

(e) Base configuration, e = 4

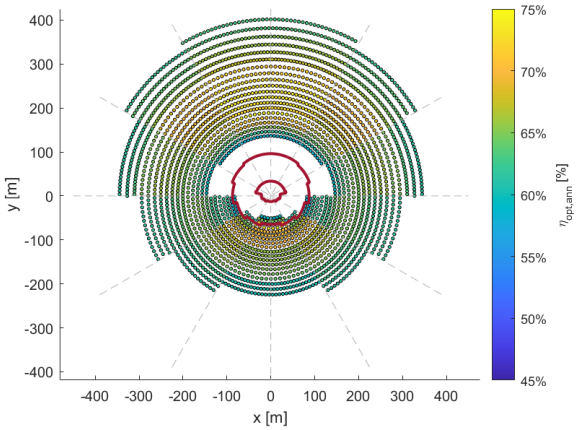

(f) Opt. configuration, e = 4

Figure 3.36: Solar field shape for base and optimized configuration at eccentricity values equal to 2, 3 and 4. Aim point equal to 100 m. e is the eccentricity. Solar field parameters as Table 3.1.

Aim Point = 120 m

e [-]	Conf.	R_{cpc} [m]	$CR_{cpc,3D}$ [-]	$\eta_{sys,des}$ [%]	$\eta_{opt,ann}$ [%]	$\eta_{sys,ann}$ [%]	#Helio [-]	Area SR [m²]
1.5	BASE	18.6	8.50	66.02	70.69	57.12	2580	6856.03
	OPT	16.1	7.75	66.66	69.85	58.90	2626	6779.35
2	BASE	11.4	4.90	70.68	69.31	60.36	2644	7810.86
	OPT	10.4	4.40	69.95	69.22	61.07	2557	7238.35
2.5	BASE	9.3	3.35	69.01	67.88	59.45	2641	8167.97
	OPT	8.8	3.10	69.47	68.56	60.32	2616	7255.57
3	BASE	8.4	2.75	65.88	65.08	57.02	2755	8291.90
	OPT	7.9	2.50	68.60	67.63	59.49	2654	7243.36
3.5	BASE	7.9	2.10	64.69	66.09	56.83	2781	7288.18
	OPT	7.4	1.85	65.75	66.97	57.93	2708	7064.37
4	BASE	7.8	1.80	62.09	65.25	54.96	2817	6886.31
	OPT	7.3	1.55	64.64	66.88	56.22	2703	6785.61

Table 3.12: Base and optimized configuration main parameters results at aim point equal to 120 m. e is the eccentricity. $\eta_{sys,ann}$ is the product between $\eta_{opt,ann}$ and $\eta_{th,ann}$. T_{rec} equal to 750 °C. Solar field parameters as Table 3.1.

e [-]	Conf.	ρ_{helio} [%]	$\eta_{cos,ann}$ [%]	$\eta_{sb,ann}$ [%]	$\eta_{s,SR,ann}$ [%]	ρ_{SR} [%]	$\eta_{int,ann}$ [%]	$\eta_{th,ann}$ [%]
1.5	BASE	95.00	83.86	97.73	98.31	95.00	97.21	80.81
	OPT	95.00	84.19	97.76	98.29	95.00	95.67	84.33
2	BASE	95.00	82.84	97.84	96.42	95.00	98.27	87.08
	OPT	95.00	83.42	97.86	96.87	95.00	96.99	88.23
2.5	BASE	95.00	82.54	97.88	94.55	95.00	98.46	87.56
	OPT	95.00	82.75	97.89	95.97	95.00	97.72	87.97
3	BASE	95.00	82.29	97.93	92.86	95.00	96.38	87.60
	OPT	95.00	91.97	97.97	95.80	95.00	97.40	87.96
3.5	BASE	95.00	83.37	97.82	91.27	95.00	98.38	86.00
	OPT	95.00	82.39	97.99	95.99	95.00	96.30	87.38
4	BASE	95.00	83.84	97.83	89.70	95.00	98.26	84.23
	OPT	95.00	81.96	98.03	96.07	95.00	96.16	85.97

Table 3.13: Base and optimized configuration efficiencies at aim point equal to 120 m. e is the eccentricity. T_{rec} equal to 750 °C. Solar field parameters as Table 3.1.

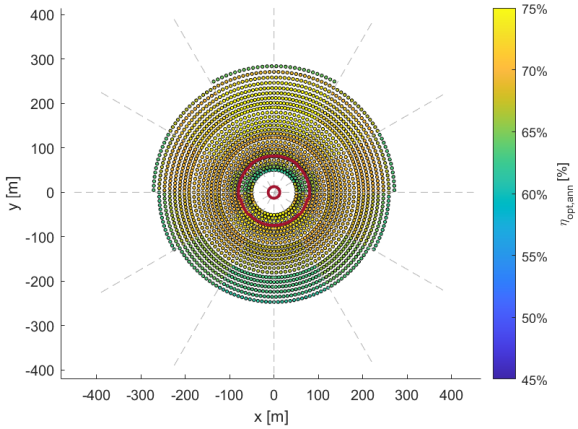

(a) Base configuration, e = 2

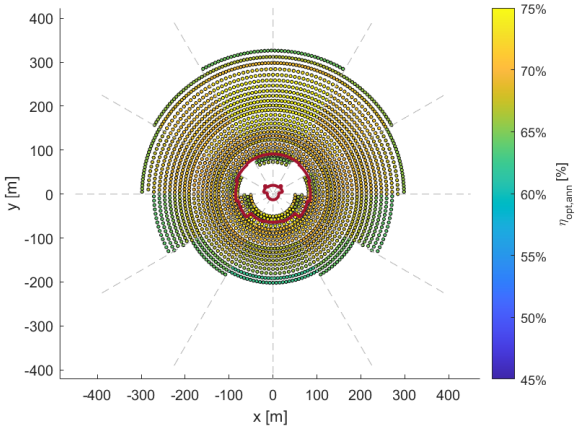

(b) Opt. configuration, e = 2

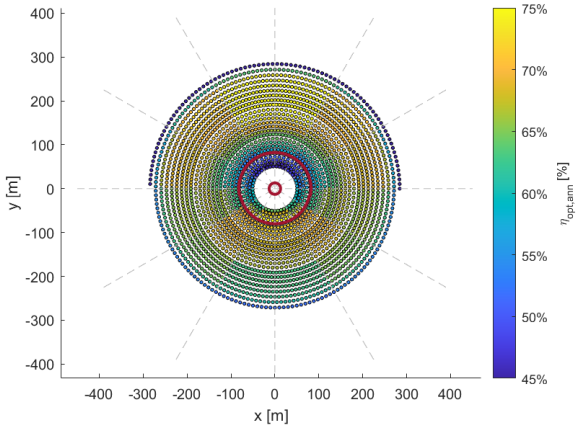

(c) Base configuration, e = 3

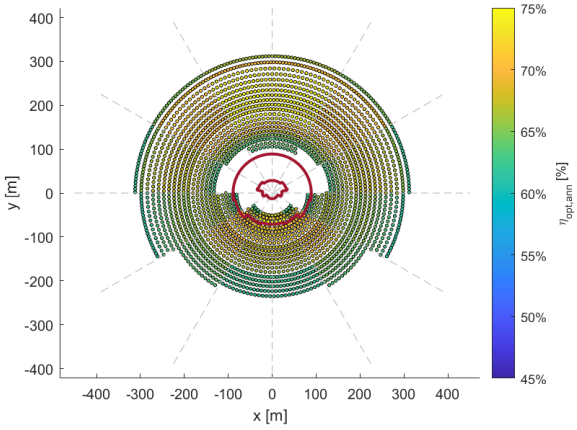

(d) Opt. configuration, e = 3

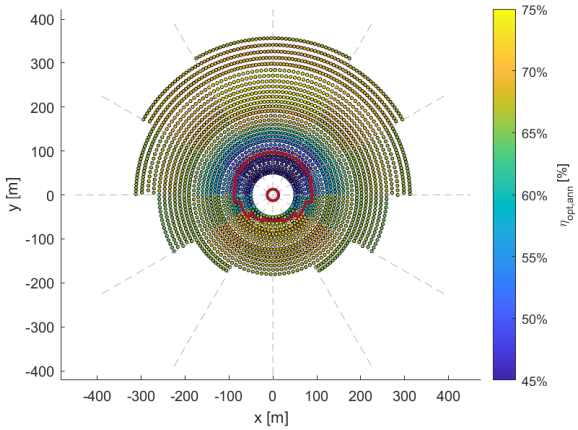

(e) Base configuration, e = 4

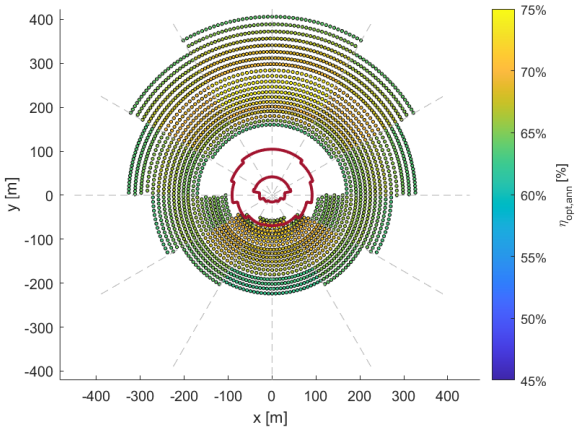

(f) Opt. configuration, e = 4

Figure 3.37: Solar field shape for base and optimized configuration at eccentricity values equal to 2, 3 and 4. Aim point equal to 120 m. e is the eccentricity. Solar field parameters as Table 3.1.

The best heliostats field configuration is found at eccentricity equal to 2, in both aim point simulations. For tower height equal to 100 m, the annual optical efficiency of the optimized configuration settles down to 68.45%, with an annual thermal efficiency of 86.87%. The overall solar field performance increases by 1.90% relative to the base configuration. At the aim point equal to 120 m, the increased cosine and thermal performances, caused by a higher concentration ratio, boost the overall solar field efficiency to a value of 61.07%. These results are in line of what was presented by Segal et al. in the first beam down optical analysis for a circular field, in which the best eccentricity value is found between 1.7 and 2.2 [43].
Starting from the base configuration the CPC inlet radius reduces in every simulation, as a trade-off between thermal and intercept performances. The CR of the CPC follows the same trend as a balance between optimized hyperboloid shadow, cosine, and intercept efficiency.
So, the optimization tries to find a balance between the optical field performances increased by lower $CR_{cpc,3D}$ and boosted thermal potential caused by the reduced CPC inlet radius.
At low eccentricity, the optimized CPC geometry differs a lot from the base configuration one. Error amplification causes too big ground image and although the $CR_{cpc,3D}$ obtained is higher with respect to bigger eccentricity values, the optimization sensibly reduces the intercept factor aiming at better thermal performances. For example at eccentricity equal to 1.5 and aim point equal to 100 m, the optimized CPC inlet radius reduces to 2.5 m. The thermal efficiency is boosted by 6% relative with a slight decrease of the intercept efficiency, that pass from 96.84% to 95.75%, at almost constant other efficiency factors. The optimization is completely thermal driven as confirmed by a 1% relative annual optical efficiency decrease.
At higher eccentricity, the optimization is again mostly thermal driven. The hyperboloid shadow performances, at aim point equal to 100 m, reach a value of 90% in the base configuration at eccentricity equal to 4. The field is optimized by selecting farther heliostats so to settle down this value around 95%. The CPC inlet radius is reduced as a trade-off of decreased intercept and boosted thermal performances. Nevertheless, the field optical performance is almost constant while the thermal efficiency increase by 4% relative to the base case. The overall annual efficiency attains the highest variation from the base configuration, with a 5% relative increase with respect to the base case.

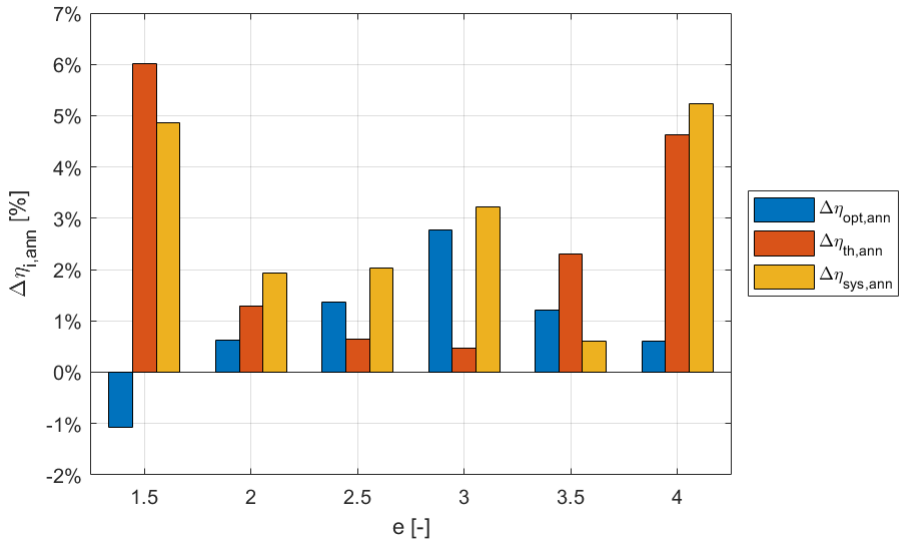

Figure 3.38: Relative percentage increase in the optimized configuration for optical, thermal and system annual efficiencies. Aim point equal to 120 m. $\eta_{sys,ann}$ is the product between $\eta_{opt,ann}$ and $\eta_{th,ann}$.

At eccentricity equal to 3, the optimization is almost field-driven. The CPC geometry slightly changes and so do the thermal performances. On the other hand, the field optical efficiency is boosted, passing from 65.30% to 67.11% at an aim point equal to 100 m, mainly driven by a 3.5% relative SR shadow efficiency increase.
In every configuration, the annual field optimization reduces the hyperboloid area. As presented in the first chapter, the selection of farther heliostats reduced the ratio of SR area over field one. Moreover the heliostats number is reduced.
The highest variation is obtained at eccentricity equal to 4 and aim point equal to 100 m, with a reduction of around 1100 m^2. The inner part of the field is sensibly affected by the hyperboloid shadow attaining annual optical performances around 40%, as shown in Figure 3.36 and Figure 3.37. Furthermore, the SR area is bigger at a higher aim point. Error amplification and lower field radius over aim point ratio increases the hyperboloid radius, so its extension.
The number of heliostats slightly increases in the optimized configuration at low eccentricity governed by a lower intercept factor so to boost the thermal performance. On the other hand, the shadow optimization at high eccentricity sensibly reduced the number of the mirror caused by the removal of low-performing heliostats in the inner field part.
The shadowing and blocking efficiency attains in every configuration at values around 97%, caused by the DELSOL3 correlation utilized for radial spacing.
At the higher aim point, the error amplification causes a slightly higher ground image

size. Nevertheless, the $CR_{cpc,3D}$ increases and compensates for the decreased thermal performance. Higher cosine and thermal capabilities boost the annual solar field efficiency that passes from 59.32% at aim point equal to 100 m and eccentricity equal to 2 to 61.07% at aim point equal to 120 m.
Results for the best field configuration found at aim point equal to 100 m and 120 m, namely the one with eccentricity equal to 2, are presented in Table 3.14.

AP [m]	R_{cpc} [m]	$CR_{cpc,3D}$ [-]	$\eta_{opt,ann}$ [%]	$\eta_{sys,ann}$ [%]	#Helio [-]	Area SR [m^2]	CR_{tot} [-]
100	10.2	3,65	68.45	59.32	2685	4447.24	749.6
120	10.4	4.40	69.95	61.07	2557	6083.18	827.8

Table 3.14: CPC geometry and main field parameteres results for the optimized configuration.

3.10. Techno-economic analysis

In this section, a techno-economic model will be presented in order to assess the Levelized Cost Of Heat (LCOH). The aim is to justify also in terms of economic parameters, and not only efficiency ones, the best field design found.
The analysis will be simplified since no information were found regarding the secondary reflector tower cost. Concerning solar tower application, there is no receiver, nor piping equipment, mounted at the top of the tower. In beam-down application, the secondary reflector installation is made only by the mirror's facets mounted generally on steel support, or as will be presented in the next chapter, in a sandwich configuration, in which both upward and downward facing surfaces are composed by a silver glass mirror structure in order to reflect the upward sun radiation.
No scientific articles were found regarding the specific weight of solar tower receiver and piping facilities, useful to compare the two different optics. So, the tower cost is considered equal to the one found for a solar tower, but in this case, the installation height is taken equal to the one attained by the hyperboloid vertex point, so the sum of the lower focus, half of the focal distance and the semi-minor axis.
Furthermore, the same specific cost of the heliostats is considered for the secondary reflector mirror. No tracking system is installed on the hyperboloid mirror facets, but the cost can be comparable due to higher installation complexity.
The LCOH evaluated considers constant annual energy production over the plant lifetime and is based on a before-tax-revenues approach, so no tax and no financing are considered. The Operation and Maintenance (O&M) are assumed constant along the plant lifetime chosen. With these assumption the LCOH can be evaluated as Equation 3.24 [44].

$$LCOH = \frac{I \cdot FCR}{E} + \frac{O\&M}{E} \tag{3.24}$$

Where:

- I is the overnight investment.
- FCR is the Fixed Charge Rate.
- E is the annual thermal energy output.
- $O\&M$ are the Operation and Maintenance cost.

The FCR expresses the amount of revenue that must be annually collected in order to cover the investment cost considering risk and inflation rates. If no tax scenario is considered, the FCR is equal to the Uniform Capital Recovery Factor (UCRF) evaluated as Equation 3.25.

$$FCR = UCRF = \frac{d(1+d)^N}{(1+d)^N - 1} \tag{3.25}$$

Where N is the lifetime period, assumed equal to 25 years, and d is the discount rate, equal to 9%. The O&M cost for CSP application are in the range of 0.018-0.036 €/kW_{th} [2]. In this work it is assumed an O&M cost of 0.023 €/kW_{th}, slightly higher than the lower boundary due to increase optic complexity.

Lifetime	25 years [2]
Discount rate	9 % [2]
O&M	0.023 €/kWh_{th} [2]
EPC & Cont.	40% of the investment [4]
DNI	7 kWh/day/m^2 [35]
Field cost	9100 €/acre
Tower cost	$2.73 \cdot 10^6\ e^{0.0113\ TH}$ €
Receiver cost	113 (1+10%) €/kW_{th} [33]
Heliostat cost	132 €/m^2

Table 3.15: Beam down optic investment assumptions. Field, tower and heliostat cost from SolarPILOT default values.

For the evaluation of the annual efficiencies presented in the previous section, a clear sky approach was utilized. In order to compare the results with the literature, the same clear sky system annual performance are considered, but the energy produced will be given by an averaged annual DNI of 7 kWh/day/m^2 and 365 days of annual operation.
The Engineering, Procurement, and Construction cost (EPC) and possible contingency are assumed equal to 40% of the overnight investment [4]. Furthermore, the receiver cost was increased by a 10% factor in order to take into account the presence of a CPC, since no cost information was found about it. However, the concentration ratio and the inlet radius can sensibly affect the reflected area of the component at different eccentricities. Nevertheless, its cost investment share cannot be too high, otherwise, its installation will not be justified.
The LCOH results for the simulated eccentricity and aim point height are presented in Figure 3.39.

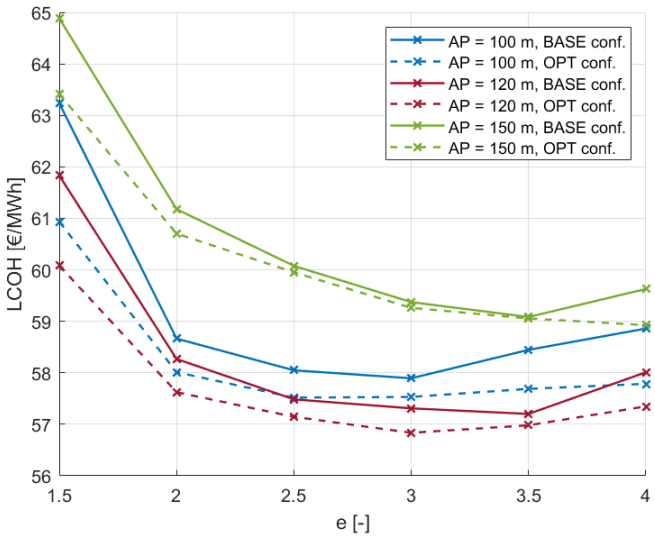

Figure 3.39: LCOH results for simplified surrounded field configuration (BASE) and annual optimized one (OPT) at aim point equal to 100, 120 and 150 m. Economic parameters as Table 3.15.

The best techno-economic configuration is found for eccentricity equal to 3 and an aim point of 120 m. The eccentricity value of 2 and the same aim point height, namely the best field configuration found in terms of annual performance, is affected by higher tower costs. The tower height at the best techno-economic configuration decreases from 94 m to 85 m. Furthermore, the slight increase of the heliostats number is compensated by a diminish on the hyperboloid area (10% relative) caused by the shadow optimization.
At aim point equal to 150 m, the tower cost increase does not justify the better field

performances and the LCOH is the highest at every eccentricities.
The annual thermal energy produced by the best techno-economic optimization is 100.85 TWh_{th}. These results are in line of what was presented by Ali Hussaini et al. for a $50MW_{th}$ solar tower in Nigeria (latitude of 12.4°). They found a LCOH around 36 €/MWh_{th}, but the design DNI was taken equal to 670 kW/m^{th} and so an higher reflective area is attained with an annual thermal generation of 150.77 TWh_{th}, assuming an annual averaged DNI of 5.5 $kWh/day/m^2$ and aim point equal to 100 m [2]. Moreover, also the mean DNI annual system efficiencies are comparable, 59.49% obtained by the beam down optimization and 54.80% for the solar tower. Nevertheless, the lower DNI design value considered for the solar tower application can sensibly reduce the annual performances.
As shown by Figure 3.40, the overall investment cost is mainly split by the receiver, tower, heliostats, and EPC cost. The hyperboloid surface area is sensibly small with respect to the field reflected ones and so is its investment cost share.

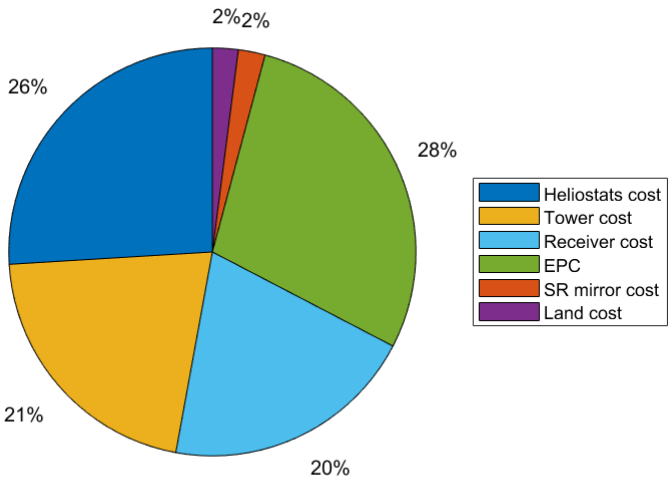

Figure 3.40: Specific cost share pie chart for the optimized configuration at aim point equal to 120 m and eccentricity equal to 3.

4 | SR thermal model

Concerning the solar tower system, the secondary reflector introduces another loss both in terms of reflectivity and shadow effect. Furthermore, the thermal load on the hyperboloid cannot be neglected. As figured in Figure 4.1, the heat flux can reach levels up to 18 kW/m^2. The simulation was performed utilizing SolTRACE with a DNI of design of 1 kW/m^2 and design solar angle. Furthermore, it was considered the best setup found both in system efficiency and techno-economic consideration, respectively the ones at aim point equal to 120 m and eccentricity equal to 2 and 3.

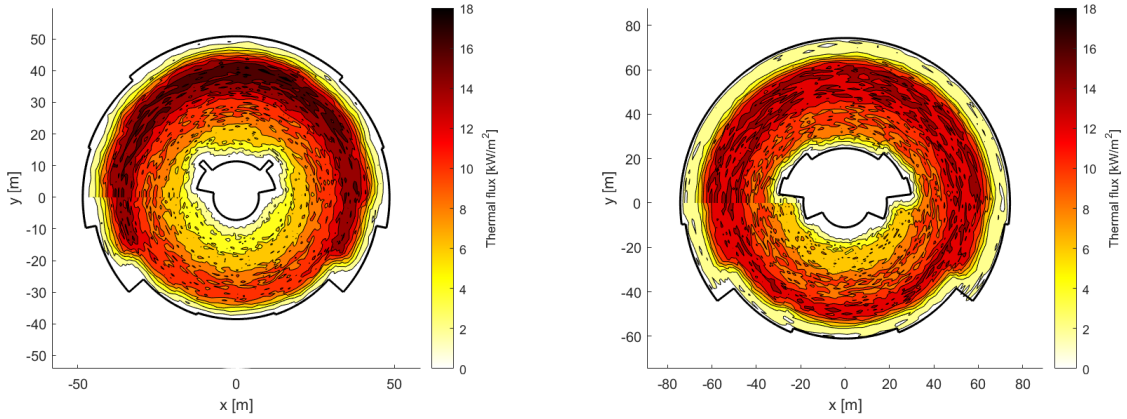

(a) Eccentricity equal to 2

(b) Eccentricity equal to 3

Figure 4.1: Secondary reflector heliostats radiation heat flux for optimized configuration and aim point equal to 120 m.

At eccentricity equal to 2 the secondary reflector installation height is higher and the surface is more concave, so its energy density in the center part. Moreover, the shadow optimization is less dominant since the SR is smaller and so the best field cosine part is preserved.
At eccentricity equal to 3, the most performing cosine part of the field is finned out and so the decreased flux in the inner hyperboloid part. Moreover, the heat flux distribution is more uniform due to lower installation height.

In this chapter, a methodology to assess the temperature level on the SR will be presented considering different possible construction procedures, namely a sandwich, aluminum upward-facing surface with and without a fin, and the last few considerations are made on a possible refrigeration system design.
Segal et. al. proposed a complete and detailed analysis for the beam down system at the Weizmann Institute of Science and the same approach will be followed here with some simplification [5].
All the considerations that will be made in the following sections are related to 1 m^2 of surface, namely a square of 1x1 m. However, this is a simplification, since the heat transfer coefficient is strictly dependent on the characteristic length considered but results can be useful in the first thermal analysis of the secondary reflector.

4.1. Secondary reflector model

Highly reflective surfaces are generally made by a thin silver film covered by glass in order to avoid the fouling degradation effect. An example of solar film is the one proposed by $3M^{TM}$, called Solar Mirror Film 1100. With a thickness of 4.6 microns and a reflectivity of 94% at air mass equal to 1.5, suits very well for the section approach presented in the previous chapter.
The glass cover needs to be highly transmitting in order to limit the reflective losses of the system. The type of glass utilized by the Weizmann Institute of science is the SCHOOT Borofloat 33 [5]. As shown in Figure 4.2, it can be modeled as a semi-transparent grey body across most of the spectrum, while an opaque grey body in the other.

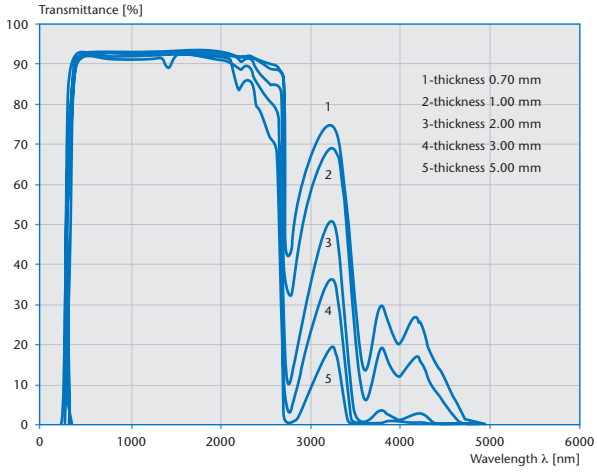

Figure 4.2: SCHOOT Borofloat 33 trasmissivity spectrum [41].

The downwards facing part of the hyperboloid is then completed as the union glass-silver facets. Moreover, the maximum operating temperature is imposed by the silver surfaces, 65 °C, since the glass one is 450 °C [17][41].
The upwards part of the secondary reflector, on the other hand, has to dissipate the high thermal flux coming from the heliostats field and the direct sun radiation.
Two different configurations were individuated by the Weizmann Institute, a sandwich configuration, in which two reflective sides are stick one to each other, or a finned one, in order to increase the heat transfer area on the upper part of the hyperboloid, as shown in Figure 4.3.

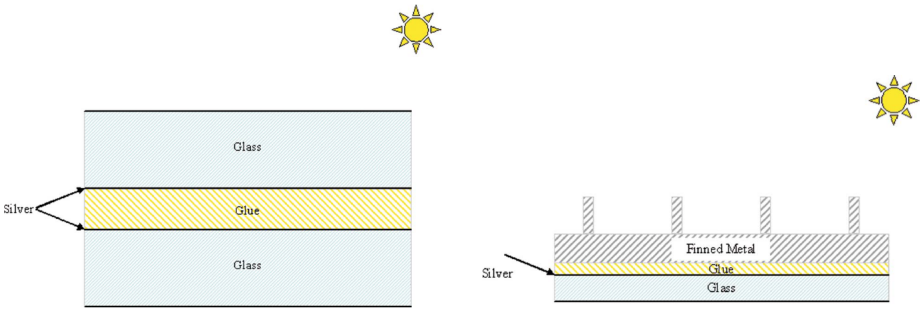

(a) Sandwich configuration (b) Finned configuration

Figure 4.3: Possible secondary reflector configuration individuated at Weizmann Institute of Science [5].

Furthermore, two other configurations were added to this work. If the metal utilized for the upward-facing surface is of a highly reflective type, like aluminium, and fins are not installed, the solution can be comparable to the one of the sandwich type.
Moreover the latter configuration can be further improved with the installation of dry cooling technology. A heat contribution is withdrawn from the upward-facing surface to limit the silver temperature.
The nature of the heat transfer is of a convective, conductive, and radiative type. The first one is between the secondary reflector and the surrounding environment. The second one takes place in between the various surfaces, while the radiative one includes the incoming heliostat radiation from the bottom and the sun one, plus the emission and absorption between the surface, the sky, and the ground.
For simplicity, the hyperboloid is treated as a horizontal flat surface with a unitary view factor on both sides, respectively with the ground and the sky. The presence of the heliostats is neglected for simplicity, or better considered in the incoming reflected radiation and the ground emission.
Nevertheless, the horizontal assumption is conservative, especially for the diminished nat-

ural convection on the downward-facing side since for inclined surface the Nusselt correlation is proportional to $Ra^{1/4}$, while for flat downward plates is $Ra^{1/5}$, where Ra is the Rayleigh number [28].
The gravity effect is limited in both situations. The first one is driven by the cosine of the surface inclination while the second one is almost blocked.
Moreover, the radiative net flux is higher, since the bottom part is facing the incoming heliostats reflected radiation.
In the following analysis will be used a 1D model. For simplicity, the tangential heat transfer is neglected and it's assumed that the incident radiation is perpendicular to the secondary reflector surface [5]. The latter is a reasonable assumption since the incidence ray direction is limited in the inner part of the field, namely the most performing one.
Convection heat transfer can be also of a forced type caused by the presence of the wind.

4.2. Physical properties

In the sandwich configuration, the system is composed of two adherent silver modules covered on both sides by glass material. The properties of these two materials are taken from the datasheet of the two components anticipated before, the SCHOOT Borofloat 33 glass and the silver film by 3M^{TM}.
For the finned configuration is it assumed that the upward-facing surface is made out of aluminium, both for the fin extension and its surface support.
If fins are not present, only the aluminium horizontal surface will be considered.

Silver-Glass module

Following the Fresnel refraction law and the Snell law, the reflectivity of a smooth transparent surface facing air for normal incoming radiation can be evaluated as Equation 4.1 [18].

$$r_g = \left(\frac{n_g - 1}{n_g + 1}\right)^2 \tag{4.1}$$

Where n_g is the refractive index of the glass and it's considered constant among the spectrum. For simplicity, also the thermal conductivity is considered constant equal to the one listed in Table 4.1.
As anticipated before, this type of glass can be modeled as a nearly perfect transparent grey body in almost all the solar spectrum, precisely in a wavelength range between 325

nm and 2500 nm, while the transmissivity then falls to zero for a longer wavelength. The silver surface is assumed as an opaque grey body in the entire spectrum.
The effective contribution given in the two bands is evaluated considering the band emission factor for a black body at 5777 K, namely the sun temperature. It was found that 93.10% of the incoming solar radiation will be transmitted and absorbed by the glass, while the surface results are opaque for the remaining interval.

Property	Value	Description
s_g	5 mm	Glass width
n_g	1.4714	Glass refractive Index
${\tau_g}^T$	0.92	Glass trasmissivity in the Transpartent band
${\rho_g}^O$	0.08	Glass reflectivity in the Opaque band
ρ_s	0.94	Silver reflectivity
k_g	1.2 W/mK	Glass thermal conductivity at 90 °C

Table 4.1: Glass and Silver radiation properties [41][17].

The effective radiative properties of the glass can be predicted by an analytical ray-trace approach. As shown in Figure 4.4, a unitary ray is approaching the glass surface. A part of it will be reflected while the $(1 - r_g)$ contributes transmitted. The ray path continues along the glass width till the silver film is met. In this zone, again, a part of it will be reflected, while the other transmitted and so absorbed by the silver film.

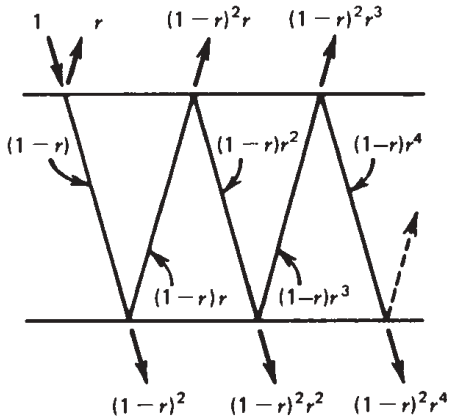

Figure 4.4: Analytical ray tracing approach [18]

In Figure 4.4, it's assumed perfect transmissivity property, so the ray energy along the glass width is governed only by the reflection. In the real model, namely the one considered

in this work, the final contribution will be the reflected one multiplied by the material transmittance. The absorbance property of the glass in the glass transparent band can then be evaluated thanks to Equation 4.2.

$$\alpha_g^T = \frac{(1-\tau_g)(1-r_g)(1+\rho_s\tau_g)}{1-r_g\rho_s\tau_g^2} \tag{4.2}$$

Since is difficult to associate the absorption contribution at every point along with the glass thickness, it is assumed that half of the contribution acts on the outer surface while the other half at the silver surface.
The silver absorbance property in the glass transparent band can then be performed as the non-reflected part of the radiation at the lower glass side.

$$\alpha_s^T = \frac{\tau_g(1-\rho_s)(1-r_g)}{1-r_g\rho_s\tau_g^2} \tag{4.3}$$

Glue

In every configuration, the upward and downward facing surfaces are stick one to each. The glue is considered to have a constant thermal conductivity of 0.4 W/mK and a 0.2 mm thickness [5].

Metal

In the finned configuration, the upward-facing hyperboloid surface is assumed made out of aluminum and also its support. The thermal conductivity is assumed constant equal to 239 W/mK [27].
The fins metal support thickness, namely the horizontal surface, is considered equal to 4 mm. Furthermore, it is assumed a grey body behavior in the entire wavelength spectrum. The hemispherical emissivity of metals is a function of the temperature and resistivity, Bartl et al. found out that the emissivity is linearly temperature correlated as Equation 4.4 [3].

$$\varepsilon(T) = 8.3\ 10^5\ T + 3.2\ 10^{-3} \tag{4.4}$$

Thanks to grey body Kirchhoff law, the hemispherical absorptivity is equal to the emissivity and the reflectivity will be $1-\varepsilon(T)$. The absorbed radiation is again split equally at the two nodes.

Air

The cinematic viscosity ν_a, the thermal conductivity k_a, and the Prandtl number Pr_a of dry air are considered quadratic curves fitted from NBS database [5].

$$\nu_a(T) = 7.239 \times 10^{-6} - 1.295 \times 10^{-8}T + 1.489 \times 10^{-10}T^2 \tag{4.5}$$

$$k_a(T) = 8.086 \times 10^{-5} + 9.715 \times 10^{-5}T - 3.314 \times 10^{-8}T^2 \tag{4.6}$$

$$Pr_a(T) = 8.271 \times 10^{-1} - 5.514 \times 10^{-4}T + 5.143 \times 10^{-7}T^2 \tag{4.7}$$

The ground and sky emission is considered as a black body one at a temperature equal to the ambient one (30 °C).

4.3. Energy Balance

The overall heat transfer is of radiative, convective, and conductive type. Every contribution will be deeply analyzed in the following subsections.
Four nodes are identified in every configuration. In the sandwich one, the two outer glass surfaces and the two silver ones. In the finned or not finned configuration, are the outer downward facing glass surface, the silver surface, the inner metal surface stick to the glue medium, and the upward facing aluminum support surface.
The temperature solution is then performed with the *fsolve* function in Matlab by solving the heat transfer balance at each of the four nodes.

4.3.1. Radiative heat transfer

The radiative heat transfer takes place between the silver-glass module and the surrounding ambient. In the glass transparent band, the net contribution on the glass surface is equal to the absorbed incidence radiation and the emission in that spectrum. However, the latter factor is negligible since the emissivity is close to zero in the considered wavelength range.
Moreover, as anticipated before, the mirror width is not negligible and so its absorption contribution is divided half on the outer surface and half on the silver surface.
On the other hand, in the glass transparent band, the silver surface it's opaque and so its net contribution it's pure of absorption and emission type. The latter can again be neglected due to its high reflectivity value.
Furthermore, in the opaque glass spectrum, the net contribution on the outer glass surface

is given by the difference between the absorption of the incident radiation and emission as a grey body. The net radiative contribution on the silver surface is zero.
The overall heat flux net contribution at glass surface in the entire spectrum is evaluated as equation below.

$$q_{net,g}^{rad} = \frac{1}{2}\alpha_g^T q_{inc} F^T + \left[(1-\rho_g^O)q_{inc} - (1-\rho_g^O)\sigma_{SB}T_g^4\right](1-F^T) \tag{4.8}$$

Where the superscript T and O refer respectively to the transparent and opaque glass spectrum. q_{inc} is the incoming radiation that takes into account the sun or heliostats one and the sky or ground black body emission. F is the transparent emission band factor. Plus sign refers to absorbed contribution while minus to released one.
On the other hand, the net heat flux contribution on the silver surface is evaluated as Equation 4.9.

$$q_{net,s}^{rad} = \left(\frac{1}{2}\alpha_g^T + \alpha_s^T\right) q_{inc} F^T \tag{4.9}$$

4.3.2. Conduction

The conductive heat flux follows the Fourier law expressed as equation below.

$$q_{cond} = -k\nabla T \tag{4.10}$$

Where k is the thermal conductivity. Nevertheless, since the heat transfer is simplified as a 1D model, the temperature will vary only along the sandwich or metal configuration width.
Furthermore is reasonable to assume linear distribution due to very thin materials and so Equation 4.10 can be simplified as Equation 4.11.

$$q_{cond} = -k\Delta T/d \tag{4.11}$$

Where d is the thickness of the material considered and k is the thermal conductivity.

4.3.3. Convection

Convective heat transfer can be of a free or forced type. The first is related to gravity-driven film on the surface, in nearly stagnant air. The second one dominates in presence of wind or forced cooling technologies.

The strength of natural convection is mainly governed by buoyancy expressed by the Grashof number Gr_L while the forced convection is characterized by the Reynolds number Re_L, with L a characteristic length. When $Gr_L/Re_L^2 \ll 1$, the forced convection dominates and the opposite for $Gr_L/Re_L^2 \gg 1$.
If the two dimensionless numbers are comparable we have a mixed convection process. In this case, the heat transfer coefficient can be roughly estimated as the maximum one between both. The error is often less than 25% with the maximum deviation at Gr_L/Re_L^2 close to unity [38].

Free Convection

The free convection is strictly dependent on the plate orientation and inclination. As anticipated before, it will be assumed that the control surface considered is flat and horizontal.
For upwards hot plates the boundary layer becomes unstable and separates at a relatively low Grashof number. The convective heat transfer can be evaluated from the Nusselt correlation of Equation 4.12.

$$\overline{Nu}_L = 0.14\ Ra_L^{1/3} \tag{4.12}$$

With the Rayleigh number interval of $10^7 < Ra_L < 10^{11}$. L is the characteristic length of the phenomena and in this case, the choice is indifferent because both Nu_L and $Ra_L^{1/3}$ are proportional to L, so the heat transfer coefficient is independent of L.
On the other hand, for downward-facing hot plate, the free convection phenomena are stable and the heat transfer coefficient can be evaluated from Equation 4.13.

$$\overline{Nu}_L = 0.58\ Ra_L^{1/5} \tag{4.13}$$

L is this case is the plate width and the correlation is valid for $10^6 < Ra_L < 10^{11}$ [28].

Forced Convection

Forced convection appears in presence of a velocity field around the geometry considered. In this case, the heat transfer is related to the Reynolds and Prandtl number.
The velocity field can be either turbulent or laminar and assumed parallel to the surface considered. The threshold can be set to Re_L equal to 5×10^5.
For laminar flow, the heat transfer coefficient can be evaluated from Equation 4.14, while

for turbulent flow from Equation 4.15.

$$\overline{Nu}_L = 0.664\ Pr^{1/5} Re_L^{1/2} \tag{4.14}$$

Valid for $Re_L \leq 5 \times 10^5$ and $0.6 \leq Pr \leq 10$.

$$\overline{Nu}_L = 0.036\ Pr^{0.43} \left(Re_L^{0.8} - 9200\right) \tag{4.15}$$

Valid for $2 \times 10^5 \leq Re_L < 5.5 \times 10^6$ and $0.7 \leq Pr \leq 380$.
In both correlations, L is the length in the velocity direction.

4.3.4. Finned configuration

The fins radiative heat transfer is neglected for simplicity. As anticipated before it is further assumed grey body behaviour of aluminium in the entire spectrum, so the radiative net trasfer is composed by the absorption, the emission and the reflection of the horizontal metal surface.
The free convection relation is evaluated as Equation 4.16, where the characteristic length is the fin height H [5],

$$\overline{Nu}_H = 0.56\ Ra_H^{1/4} \tag{4.16}$$

For simplicity, the film temperature is evaluated as the reciprocal of the mean temperature between the ambient and the horizontal surface one.
The forced convection can still be evaluated with Equation 4.14 and Equation 4.15.
Furthermore, in this type of configuration two different surfaces participate in the convective dissipation, namely the aluminium horizontal support and the fin extension.
The convective heat loss from a fin can be evaluated as Equation 4.17.

$$\dot{Q}_f = Ah(T_w - T_{amb})\eta \tag{4.17}$$

Where A is the fin convective area, h the averaged heat transfer coefficient, and η the fin efficiency. The latter parameter represents the ratio between the heat dissipated by the fin and the one released by an iso-thermal fin at the support wall temperature.

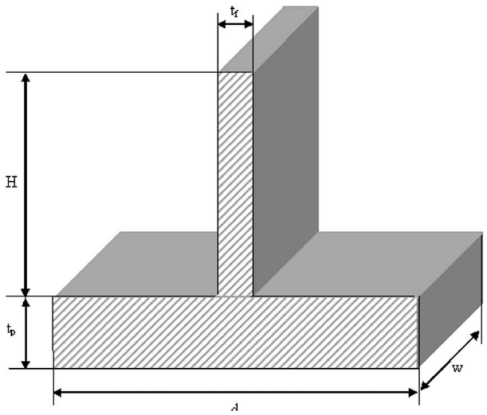

Figure 4.5: Fin geometric parameters [5].

Equation 4.17 holds for the fin profile in which the temperature difference between the wall temperature and the ambient one is much higher than the temperature difference in the fin transversal direction. This condition is verified when the Biot number $Bi_{fin} = \frac{h(A/P)}{k}$ is much less than 1, with P the fin wetted perimeter.
It is further assumed that the dissipation from the thin lateral surface and from the fin tip is neglected due to the small heat transfer area. By saying that the differential equation solution for a non-isothermal fin with adiabatic tip holds and the efficiency is evaluated as Equation 4.18.

$$\eta = tanh(mH)/mH \tag{4.18}$$

Where H is the fin height and m is defined as:

$$m = \sqrt{\frac{2h}{kt_f}} \tag{4.19}$$

With k the thermal conductivity of the fin.
The overall heat transfer coefficient, for both horizontal and vertical surfaces, can be evaluated as Equation 4.20.

$$h = \frac{Q_{conv}}{Lw(T_w - T_{amb})} = \frac{1}{d}[2Hh_v\eta + (d - t_f)h_h] \tag{4.20}$$

Where the subscripts v and h represent respectively the vertical and horizontal surfaces. An important characteristic in designing finned surfaces is the product mH. By looking at the fin efficiency, the heat transfer cannot be sensibly increased for mH higher than

3 [28]. In this sense, the fin height is limited by the latter threshold in the worst-case condition, namely at zero wind velocity. The values found was equal to 50 cm.
For non-finned configuration, the heat transfer coefficient will be simply the one of the horizontal surfaces.

4.3.5. Cooled configuration

The fourth possible configuration is the installation of a dry cooling or a similar refrigeration technology able to withdraw a heat contribution from the upward-facing surface to limit the silver temperature.
The refrigerant power needed is evaluated considering a silver surface temperature equal to 65 °C. So the non-linear equation system is solved again for the three remaining temperature unknowns and the refrigerant heat contribution withdraw from the outer upward-facing surface in the metal configuration without fins.
Nevertheless, this solution is a simplification since the upward-facing surface radiative and convective heat transfer have to be properly recalculated due to the presence of possible refrigerant tube bundles.
However, the results obtained can be considered as a first good first thermal analysis for a m^2 of hyperboloid surface considering also possible different refrigeration systems.

4.4. Results

The silver temperature obtained in sandwich layout, in metal layout without a fin, and with are represented in Figure 4.6a, 4.6b and 4.6c. The refrigerant power needed per meter square of surface to keep the silver temperature under its maximum operating limit at the design point is presented in Figure 4.6d.
All the configurations were analyzed for a range of wind velocities from 0 to 10 m/s.
The Gr/Re^2 factor is plotted for the downward-facing surface.

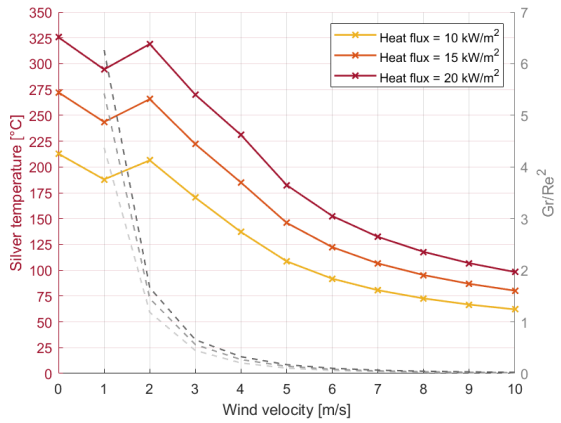

(a) Sandwich configuration

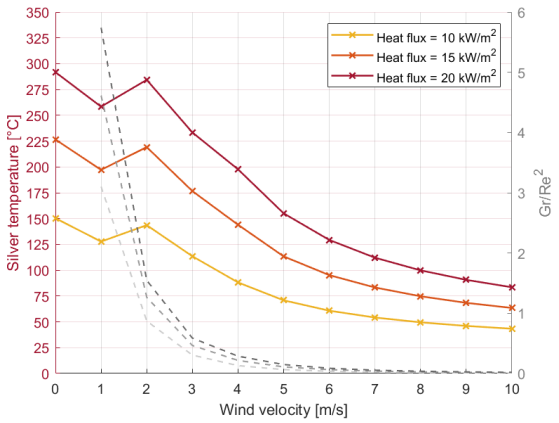

(b) Metal configuration w/o fin

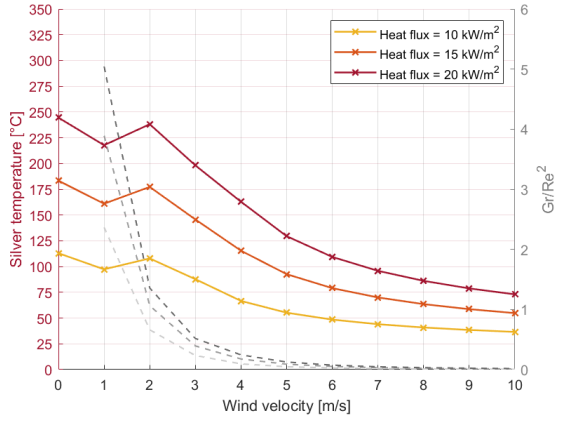

(c) Metal configuration w/ fin

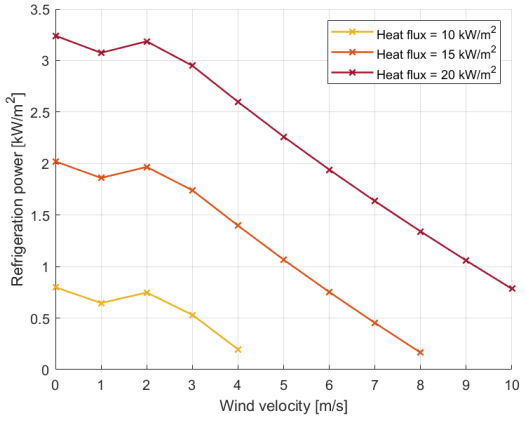

(d) Dry cooler refrigerant power

Figure 4.6: Silver temperature and dry cooler refrigerant power for four different secondary reflector configuration.

It can be noticed how, for heat flux over 10 kW/m^2 and stagnant air, any configuration is valuable to limit the silver temperature except using refrigeration equipment.
The glass absorbance set to a value equal to 9%, while the silver one is almost 5%.
Taking the example of the sandwich configuration, at a velocity equal to zero, the convective heat transfer is of a free type. Increasing the wind velocity, at the downward-facing surface, the convection starts to be mixed due to comparable Gr/Re^2 factor and the forced convection dominates. At the upward surfaces, the favorable buoyancy effect continues to dominates till wind velocity is equal to 4 m/s. This justifies the non-flat silver temperature behavior at low velocity.
The Rayleigh number in every configuration is in the order of 10^{10}, so the Nu correlations boundaries are respected.
The forced convection is of a laminar type till velocity of 9 m/s and then turns into a turbulent one. Furthermore, the temperature difference between the two outer surfaces of the hyperboloid is in the range of 5-10 K due to the conductivity effect.
The metal configuration performs better than the sandwich one in both cases, namely with and without fins. Due to the high reflectivity and conductivity of aluminum, the upward-facing surface dissipation is favor both in terms of radiative and convective heat transfer.
The fin appears to be oversized at high wind velocity, reaching values of mL close to 5 and so the fin efficiency that passes from 38% at stagnant air to 21% at wind velocity of 10 m/s.
If the incident heat flux on the meter square of surface considered doesn't limit the silver temperature to its maximum operating one, a refrigeration system is needed. As shown in Figure 4.6d, in the metal configuration without a fin, stagnant air and heat flux equal to 20 kW/m^2, the heat withdrawn from the upper surface is around 3.25 kW/m^2. As wind temperature increases, the refrigeration power decreases due to better convective transfer dissipation.
The results are influenced by the characteristic length considered, namely 1 m. Nevertheless, considering a characteristic length of 50 m, the relative error on the results is lower than 10% on the silver temperature. So, the analysis can be considered as a good first value in analyzing the secondary reflector behavior. For every m^2 at a given heat flux and wind velocity, one of the possible four configurations has to be considered to limit the silver temperature.

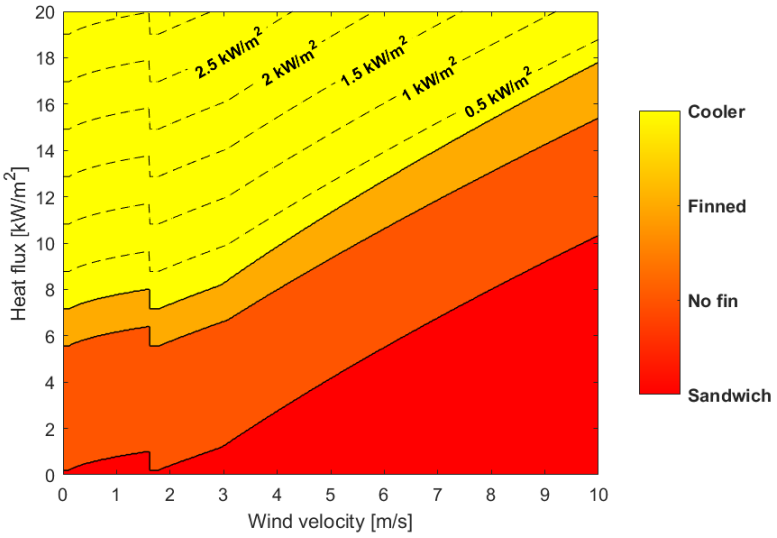

Figure 4.7: Secondary reflector possible configuration to limit the silver temperature at 65 °C. Dashed isoline represent the refrigeration power.

If the silver temperature is limited to 65 °C, most of the secondary reflector needs to be cooled down by a chiller.
At higher eccentricity, the flux distribution is more uniform and the area percentage to be cooled can reach up to 45% at silver limiting temperature of 65 °C, as shown in Figure 4.8.

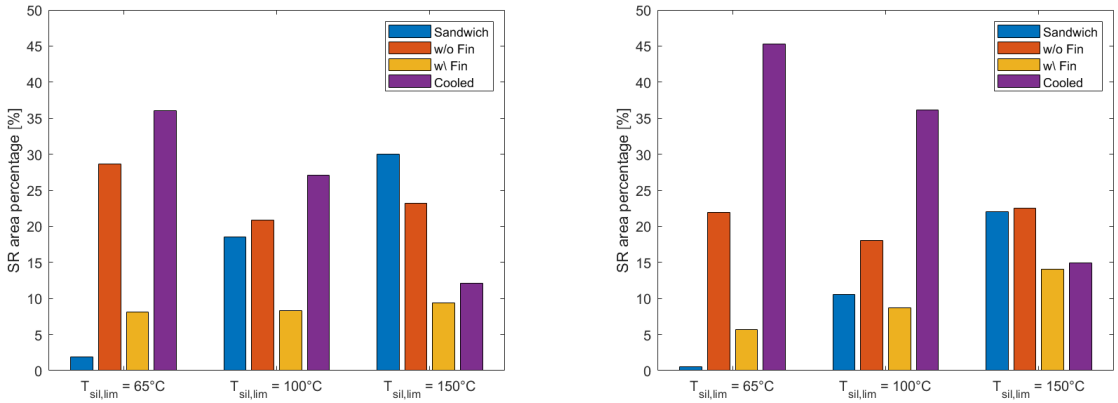

(a) e = 2, aim point = 120 m

(b) e = 3, aim point = 120 m

Figure 4.8: Configuration area percentage coverage for 3 possible silver limiting temperature. Wind velocity equal to 2 m/s.

At $T_{sil,lim}$ of 150 °C, in both configuration, almost 50% of the secondary reflector area can be made out of sandwich or metal pattern. The choice will be based on techno-economic and structural consideration.
As shown in Table 4.2, at higher eccentricity the refrigerant power increases, also caused by a slightly bigger hyperboloid. The refrigerant power can be sensibly reduced up to 2.23 MW at design condition, and wind velocity of 2 m/s, if the limiting silver temperature is pushed to 150 °C.

$\dot{\mathbf{Q}}_{\mathbf{refr}}$ [MW]	$T_{sil,lim}$		
	65 °C	**100 °C**	**150 °C**
e = 2	4.54	4.18	2.63
e = 3	5.38	4.99	2.74

Table 4.2: Refrigerant power in order to keep the silver temperature under its limiting condition. Wind velocity equal to 2 m/s.

Nevertheless, the model presented does not consider the horizontal flux dissipation. The SR surface flux can be homogenized and sensibly reduced the cooling power needed per meter square. Moreover, the glass transmittance and absorbance properties were simplified considering grey body behavior in almost the entire spectrum.
The BD design needs to be accompanied by thermal analysis of the secondary reflector. In this sense, a lower design power solar field can possibly reduce the thermal load on the hyperboloid and allows for simple, not cooled configurations.

Conclusions

Nowadays, just a few Beam-Down systems are installed all over the world. The configuration needs still to reach its learning rate in order to be competitive in the CSP market. All the existing solar field makes use of a circular surrounded heliostats field pattern and, moreover, their power is limited to 17 MW_{th} (Yumen, China).
This works aim at generalized the Beam-Down solar field creation, considering the presence of a Compound Parabolic Concentrator (CPC) and the Secondary Reflector (SR) shadow derating factor. In this sense, a 50 MW_{th} point focus Beam-Down optimized solar field at a given latitude is presented.
The overall optic and geometric characteristics were firstly analyzed making use of a random light point distribution and optical error. The system was then coupled with a CPC aiming at boosting the receiver's thermal performance. The latter is completely defined by two geometric parameters, the inlet radius, and the maximum acceptance angle. The higher is the latter, the lower will be the CPC Concentration Ratio ($CR_{cpc,3D}$).
The optic theory was then applied to a real heliostat's solar field. The mirrors field pattern considered was a radial staggered one and it was implemented in Matlab following the *campo* code presented by Collado. The shadowing and blocking performance were assessed thanks to the Sassi methodology.
To unconstrain the hyperboloid shape from the normal circular model, the solar field was divided into sections of equal azimuth extension, so a sliced SR shape is created.
Then, the hyperboloid shadow was added, concerning solar tower application, and it was found that the best cosine solar field part was strongly affected by the presence of an SR. In this sense, it was found that possible farthermost heliostats, less shaded, can replace worst-performing ones, increasing the annual optical performance up to 3%.
Nevertheless, the heliostats selection is sensibly influenced by the CPC geometry. Farther mirrors selection are affected by higher receiver incidence angle and ground image size. So an optimum system configuration (heliostats field plus CPC geometry) must exist as a trade-off between optical and thermal performances.
Starting from a simplified surrounded field configuration, a first guessing value of the CPC inlet radius and $CR_{cpc,3D}$ is found. Furthermore, the CPC geometry is varied in order to

maximize the annual system performances. The receiver temperature was assumed equal to 750 °C, namely the current limiting value for particles receiver application. The optimization was performed at different eccentricity and aim point values.
System efficiency results were compared also on a techno-economic point of view, and the best BD optimized configuration in terms of LCOH was found at eccentricity equal to 3 and an aim point of 120 m. In this case, the optimization is mainly optical driven, caused by a 3.5% relative percentage increase in the annual shadow hyperboloid efficiency concerning the surrounded field configuration. The field shape becomes slightly asymmetric, and North-oriented, resulting in an annual optical efficiency of 65.08% and a thermal efficiency of 87.96%.
The CPC inlet radius settles down to a value of 7.9 m and the $CR_{cpc,3D}$ is 2.50.
Furthermore, the number of the mirror reduces from 2755 to 2654 and the same trend is followed by the SR area which decreases by 12% relative. The annual energy produced is 100.85 TWh_{th} at averaged annual DNI of 7 kWh/day/m^2. The LCOH settles down at value of 57 €/MWh_{th}.
These results are comparable of what was presented by Ali Hussaini et al. for a 50MW_{th} solar tower in Nigeria (latitude of 12.4° N). They found a LCOH around 36 €/MWh_{th}, but the design DNI was taken equal to 670 kW/m^{th} and so an higher reflective area is attained with an annual thermal generation of 150.77 TWh_{th}, assuming an annual averaged DNI of 5.5 kWh/day/m^2 and aim point equal to 100 m [2]. Moreover, also the mean DNI annual system efficiencies are comparable, 59.49% obtained by the beam down optimization and 54.80% for the solar tower. Nevertheless, the lower DNI design value considered for the solar tower application can sensibly reduce the annual performances.

Furthermore, a 1D SR thermal model for the temperature distribution along the hyperboloid was presented in order to evaluate whether it is necessary to install a refrigerant system to keep temperatures to the values allowed by the specifications of each material. Different SR configurations were studied, namely the sandwich, the finned or not one, and the possibility of dry cooling technology.
The radiative properties of the glass silver surface were assessed by making use of an analytical ray-trace approach. Both materials were considered to act as a grey body, in almost the entire solar spectrum.
The convective loss was differentiated between natural and forced one, making use of the Gr/Re^2 factor. The characteristic length was assumed equal to 1x1 m in order to generalize the analysis.
At the best techno-economic configuration, if the silver temperature is limited to 65 °C, 45% of the hyperboloid surface needs to be cooled down. If the silver temperature limit

can be increased up to 150 °C, this value reduces to 14%. In the latter case, the fin configuration occupies another 14%, the not finned one the 22.5 %, and in the remaining part a sandwich configuration can be utilized.
The overall refrigeration heat settles down at 5.38 MW at a silver temperature of 65 °C, to 2.74 MW at 150 °C.

Future work

The optic of a Beam-Down needs still to be fully comprehended. In the last years, the number of scientific papers published has proved the research community's interest in this particular CSP application. The trend is confirmed by the first commercial BD power plant installed in China.
The model presented lacks of accurate analysis in the receiver thermal behaviour and CPC optic. In this sense, a suitable configuration of particle receivers needs still to be directly associated and the thermal model deeply assessed. Moreover, an accurate approach for the CPC transmissivity efficiency can be accompanied in order to improve the accuracy of the intercept efficiency calculation.
The heliostats field was considered made of rectangular flat mirrors. The use of a parabolic geometry can increase the intercept efficiency due to a reduced aberration effect. Moreover, the mirror size needs to be optimized as a trade-off between performance and cost increase.
Valuable results in terms of system efficiency can then be obtained by selecting a proper solar site and analyzing the real DNI distribution throughout the year.
The system can then be coupled with direct thermal storage and a bottom sCO_2 power cycle. The latter can favor high conversion efficiency, thanks to boosted receiver temperature compared to the molten salt technology. The system optimization can then follow a cost of sell maximization approach, so to minimize the LCOE.
Moreover, scaling up beam down solar system needs to take into account the thermo-mechanical stress on the hyperboloid surface. In this sense, a 3D thermal model needs to be considered in order to properly analyze the heat flux distribution. The design power will then be a compromise between the refrigeration heat, material utilized and energy produced.
Lastly, the cost of the tower needs still a proper value since no receiver is mounted on top as for solar tower application. On the other hand, the wind loads can strongly decrease the structural and optical performance.

Bibliography

[1] Concentrating solar power: clean power on demand 24/7. Technical report, The World Bank, 2020.

[2] Z. Ali Hussaini, P. King, and C. Sansom. Numerical simulation and design of multi-tower concentrated solar power fields. *Sustainability*, 2020.

[3] J. Bartl and M. Baranek. Emissivity of aluminium and its importance for radiometric measurement. *Measurement of Physical Quantities*, 2004.

[4] A. Bejan, G. Tsatsarosin, and M. Moran. *Thermal Design Optimization*. Wiley, 1996.

[5] R. Ben-Zvi, A. Segal, and M. Epstein. Beam-down mirror: Thermal and stress analyses. *ASME. J. Sol. Energy Eng.*, 131, 2009.

[6] P. Bendt, A. Rabl, H. Gaul, and K. Reed. Optical analysis and optimization of line focus solar collectors. 1979.

[7] S. M. Besarati and D. Y. Goswami. A computationally efficient method for the design of the heliostat field for solar power tower plant. *Renewable Energy*, 69:226–232, 2014.

[8] M. Binotti, G. Manzolini, and G. Zhu. An alternative methodology to treat solar radiation data for the optical efficiency estimate of different types of collectors. *Solar Energy*, 110:807–817, 2014.

[9] A. Bonanos. Error analysis for concentrated solar collectors. Technical report, AIP, 2012. Journal of Renewable and Sustainable Energy.

[10] N. Calvet, M. Martins, and B. Grange. The masdar institute solar platform: A new research facility in the uae for development of csp components and thermal energy storage systems. Technical report, AIP, 2016. AIP Conference Proceedings 1734.

[11] CNRS. On dense granular flows. *The European Physical Journal*, 2004.

[12] F. Collado. Quick evaluation of the annual heliostat field efficiency. *Solar Energy*, pages 379–384, 2008.

[13] F. J. Collado and J. Guallar. Campo: Generation of regular heliostats fields. *Renewable Energy*, 46:49–59, 2012.

[14] F. J. Collado and J. Guallar. Improved heliostat field design for solar tower plants. *AIP Conference Proceedings*, 1850, 2017.

[15] CSPFOCUS. Yumen xinneng 50mw molten salt tower csp project, 2019. URL `http://www.cspfocus.cn/en/report/detail_39.htm`.

[16] M. Diago, P. Calvet, and P. R. Armstrong. Net power maximization from a faceted beam-down solar concentrator. *Solar Energy*, 204:476–488.

[17] R. E. Division. 3m solar mirror film 1100. Technical report, 3M, 2012.

[18] J. A. Duffie and W. A. Beckam. *Solar Engineering of Thermal Processes*. WILEY, 2013.

[19] A. Giostri. *Transient effects in linear concentrating solar thermal power plant*. PhD thesis, Politecnico di Milano, 2014.

[20] IEA. Concentrated solar power (csp), 2021. URL `https://www.iea.org/reports/concentrated-solar-power-csp`.

[21] K. Jiang, X. Du, Y. Kong, C. Xu, and X. Ju. A comprehensive review on solid particle receivers of concentrated solar power. *Renewable and Sustainable Energy Reviews*, 116, 2019.

[22] B. Kistler. A user's manual for DELSOL3: A computer code for calculating the optical performance and optimal system design for solar thermal central receiver plants. Technical report, Sandia National Laboratories, 1986.

[23] T. Kodama, N. Gokon, K. Matsubara, K. Yoshida, S. Koikari, Y. Nagase, and K. Nakamura. Flux measurement of a new beam-down solar concentrating system in miyazaki for demonstration of thermochemical water splitting reactors. *Energy Procedia*, pages 1990–1998, 2014.

[24] H. Lee. The geometric-optics relation between surface slope error and reflected ray error in solar concentrators. *Solar Energy*, pages 299–307, 2014.

[25] E. Leonardi. Detailed analysis of the solar power collected in a beam-down central receiver system. *Solar Energy*, pages 734–745, 2012.

[26] C. Li, R. Zhai, and Y. Yang. Optimization of a heliostat field layout on annual basis using a hybrid algorithm combining particle swarm optimization algorithm and genetic algorithm. *energies*, 2017.

[27] J. Li and B. Yu. *In The Fundamentals and Sustainable Advances in Natural Gas Science and Eng*, volume 1. Gulf Professional Publishing, 2022. ISBN 9780128244951.

[28] J. H. Lienhard. *A Heat Transfer Textbook*. Phlogiston Press, 2 edition, 2012.

[29] LIFEGATE. Stem, quando la sabbia cattura i raggi del sole per produrre energia, 2017. URL `https://www.lifegate.it/stem-sabbia-energia-sole-energia`.

[30] K. Lovegrove and W. Stein. *Concentrating Solar Power Technology*. Elsevier, 2020.

[31] Magaldi. Concentrated solar power-STEM. URL `https://www.magaldi.com/en/products-solutions/csp-concentrating-solar-power`.

[32] N. Matsapey, J. Faucheu, and D. Delafosse. Design of a gonio-spectro-photometer for optical characterization of gonio-apparent materials. *Measurement Science and Technology*, 2013.

[33] M. Mehos, C. Turchi, J. Vidal, M. Wagner, Z. Ma, C. Ho, W. Kolb, C. Andraka, and A. Kruizenga. Concentrating solar power gen3 demonstration roadmap. Technical report, National Renewable Energy Laboratory, 2017.

[34] R. Merchàn, M. Santos, A. Medina, and A. Calvo Hernàndez. High temperature central tower plants for concentrated solar power: 2021 overview. *Renewable and Sustainable Energy Reviews*, 155, 2022.

[35] NREL. Solar resource maps and data. URL `https://www.nrel.gov/gis/solar-resource-maps.html`.

[36] NREL. Yumen xinneng / xinchen - 50mw beam-down csp project. URL `https://solarpaces.nrel.gov/project/yumen-xinneng-xinchen-50mw-beam-down`.

[37] A. S. Pidaparthi. Heliostat cost reduction for power tower plants. Master's thesis, Stellenbosch University, 2017.

[38] W. M. Rohsenow, J. P. Hartnett, and Y. I. Cho. *Handbook of Heat Transfer*. McGraw-Hill, 3 edition, 1998. ISBN 0070535558.

[39] D. Saldivia, J. Bilbao, and R. A. Taylor. Optical analysis and optimization of a beam-down receiver for advanced cycle concentrating solar thermal plants. *Applied Thermal Engineering*, 2021.

[40] G. Sassi. Some notes on shadow and blockage effect. *Solar Energy*, 31:331–333, 1983.

[41] SCHOTT. Schott borofloat 33: The versatile floated borosilicate glass. Technical report.

[42] A. Segal. Solar energy at high temperatures; researches at the weizmann institute of science, israel; 25 years of success. Technical report, EDP Sciences, 2016. Renewable Energy Enviromental Sustainability.

[43] A. Segal and M. Epstein. The optics of the solar tower reflector. *Solar Energy*, pages 229–241, 2000.

[44] W. Short, D. J. Packey, and T. Holt. A manual for the economic evaluation of energy efficiency and renewable energy technologies. Technical report, NREL, 1995.

[45] M. Tian, Y. Su, H. Zheng, G. Pei, G. Li, and S. Riffat. A review on the recent research progress in the compound parabolic concentrator (cpc) for solar energy applications. *Renewable and Sustainable Energy Reviews*, 82:1272–1296, 2018.

[46] M. J. Wagner and T. Wendelin. Solarpilot: A power tower solar field layout and characterization tool. *Solar Energy*, 171:185–196, 2018.

[47] X. Wei, Z. Lu, W. Yu, and W. Xu. Ray tracing and simulation for the beam-down solar concentrator. *Renewable Energy*, pages 161–167, 2013.

[48] T. Wendelin, A. Dobos, and A. Lewandowski. Soltrace: A ray-tracing code for complex solar optical systems. Technical report, NREL, 2013.

[49] X. Xie, M. Ni, J. Yan, H. Dong, and K. Cen. Optical and thermal performance of a novel solar particle receiver. *AIP Conference Proceedings*, 2126, 2019.

[50] A. Zeghoudi, M. Debbache, and A. Hamidat. Contribution to minimizing the cosine loss in a thermodynamic solar tower power plant by a change in the target position. *European Journal of Electrical Engineering*, 19:367–374, 2017.

[51] W. Zhao, Z. Sun, and Z. T. Alwahabi. Emissivity and absorption function measurements of al2o3 and sic particles at elevated temperature for the utilization in concentrated solar receivers. *Solar Energy*, 207:183–191, 2020.

[52] H. Zheng. *Solar Energy Desalination Technology*. Elsevier, 2017.

A | Appendix A

The Sassi methodology utilized for the evaluation of the shadowing and blocking performance for every heliostat will be here presented.
Let's consider a generic i-heliostat and a k-heliostat interfering for shadowing and blocking. The center of the i-heliostat lies in a cartesian XY plane at the point $[0, 0]$, while the generic center P of the k-heliostat lies into a 3D space with relative coordinates $[x_p, y_p, z_p]$, as presented in Figure A.1

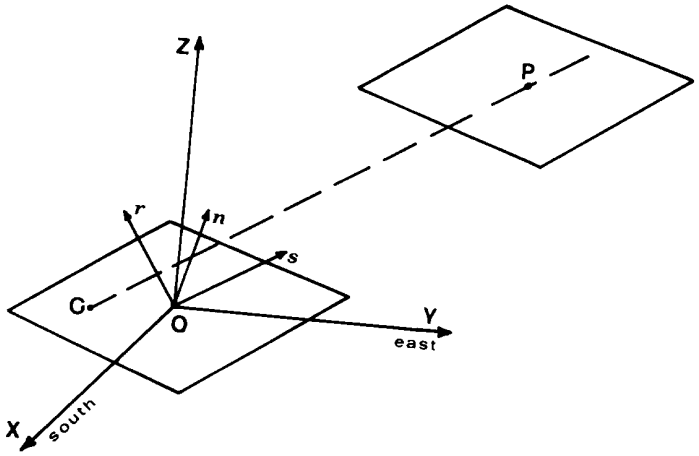

Figure A.1: Generic i-heliostat centered in the XY plane and the center P of the k-heliostat [40].

Let's consider the shadowing case and so the generic sun versor $\overrightarrow{\mathbf{s}}$ defined by $[s_x, s_y, s_z]$ pointing the i-heliostat. The same consideration can be made for blocking performance considering the reflected vector of the i-heliostat.
The straight line passing through P with direction defined by $\overrightarrow{\mathbf{s}}$ can be evaluated by Equation A.1.

$$\frac{x - x_p}{s_x} = \frac{y - y_p}{s_y} = \frac{z - z_p}{s_z} \tag{A.1}$$

The i-heliostat lies on a plane specified by its normal vector $\overrightarrow{\mathbf{n}}$ as Equation A.2.

$$n_x \cdot x + n_y \cdot y + n_z \cdot z = 0 \tag{A.2}$$

The solution of equation Equation A.1 and Equation A.2 gives the projection of point P into the i-heliostat plane.
The projected point and the heliostat plane can be then translated into a XY plane where the edges of the heliostat are parallel to the Cartesian axis, and the new coordinate $[x_e, y_e]$ and $z_e = 0$ of the point P are evaluated as Equation A.3.

$$\begin{aligned} x_e = \{&[n_x (s_x n_y - s_y n_x) / \Omega - n_y] x_p + [n_y (s_x n_y - s_y n_x) / \Omega + n_x] y_p \\ &+ n_z (s_x n_y - s_y n_x) z_p / \Omega\} / \Phi \end{aligned}$$

$$y_e = [-s_z n_x x_p - s_z n_y y_p + (s_x n_x + s_y n_y) z_p] / (\Omega \Phi) \tag{A.3}$$

Where $\Omega = \overrightarrow{\mathbf{s}} \cdot \overrightarrow{\mathbf{n}}$ and $\Phi = \sqrt{n_x^2 + n_y^2}$.

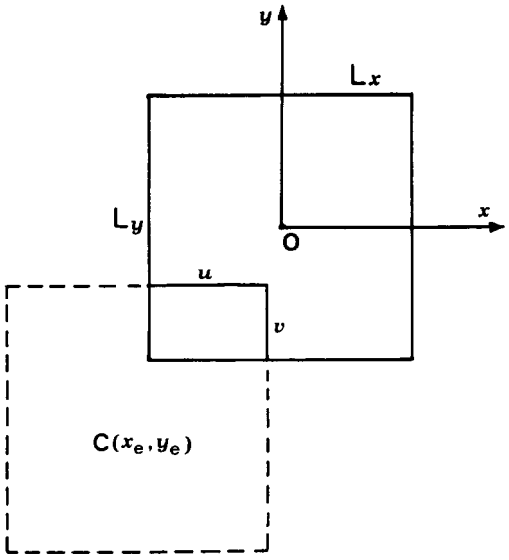

Figure A.2: Projection of k-heliostat on i-heliostat surface assuming same normal vector for both mirror [40].

The main assumption of the Sassi method is that the two heliostats have the same normal vector. By saying that the k-heliostat interfere for shadowing if the condition of Equation A.4 are both fulfilled.
In a solar field, this is a reasonable assumption since interfering mirrors lie in the neighborhood of the analyzed heliostat.

$$| x_e | < WM; \qquad | y_e | < HM; \tag{A.4}$$

Where WM is the heliostat width and HM is the height.

Four different zones of overlapping are then identified as shown in Figure A.3.

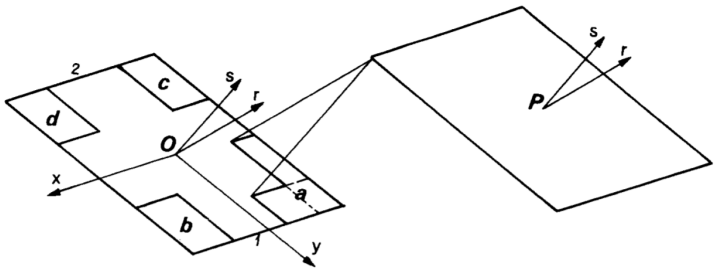

Figure A.3: Four different sort of overlapping [40]

Let's now define the variable u and v as Equation A.5, and divide the heliostat edges 1 and 2 (Figure A.3) into n equidistant interval.

$$u = WM - | x_e |; \qquad v = HM - | y_e | \tag{A.5}$$

In order to quantify the part of the i-heliostat surface covered by the k-heliostat a function F is defined, which for every discretization of side 1 and side 2, assume the value of v if the k-mirror overlap the interval, or value 0 if not. For the four different projection shown in Figure A.3, F is evaluated as Equation A.6.

$$F(j,k) = v \begin{cases} for & 1 \leq j \leq u/d & case\ a \\ for & \frac{WM-u}{d} \leq j \leq n & case\ b \\ for & n+1 \leq j \leq n+1+u/d & case\ c \\ for & n+1+\frac{WM-u}{d} \leq j \leq 2n & case\ d \end{cases} \tag{A.6}$$

Where $d = WM/n$ is the width of each interval and j, varies from 1 to $2n$.

k denoted the heliostat considered, so the column dimension of F will be the number of interfering heliostat considered.
By saying that the highest overlapping height $R(j)$ for each interval will be the maximum of the F rows wise, as expressed by Equation A.8.

$$R(j) = max(F(j,k)) \tag{A.7}$$

With k varying from 1 to the total K interfering heliostats.
Finally, the overlapping area fraction O_f is given by Figure A.2

$$O_f = \frac{\sum_1^{2n} R(j)}{n \cdot HM} \tag{A.8}$$

So the shadowing efficiency η_{sb} will be equal to $1 - O_f$.
All the equations presented are referred to the case of shadowing. The same procedure can be repeated for blocking performance, considering the aiming vector $\overrightarrow{\mathbf{a}}$ of the i-heliostat instead of $\overrightarrow{\mathbf{s}}$.
Overall, in the quantification of the covered area, for each interval the highest overlapping peak $v(j)$ has to be selected between blocking or shadowing.
Another important assumption of the procedure is that the heliostat side 1 and 2 are divided into n steps, so the maximum overlapping height in every j interval can be only $HM/2$. However, this is a reasonable assumption in the range of solar angle simulated in solar field application, considering a reasonable radial and azimuth distance between heliostats.

B | Appendix B

The solar position is evaluated utilizing spherical geometric relationship of the earth and sun. Given a solar site with Latitude L, Julian day of the year D, and an solar hour of a day H, the azimuth Az and elevation of the sun can be evaluated as set of Equation B.1 [18].

$$\begin{aligned} El &= \arcsin\left(\cos L \cdot \cos\delta \cdot \cos\omega + \sin\delta \cdot \sin L\right) \\ Az &= sgn(\omega)\left|\arccos\left(\sin El \cdot \sin L - \sin\delta\right) / \left(\cos El \cdot \cos L\right)\right| \end{aligned} \tag{B.1}$$

Where:

$$\omega = 15\pi\left(H - 12\right)/180; \qquad \delta = \frac{23.45\pi}{180}\sin\left(2\pi\frac{284 + D}{365}\right)$$

All the angles, have to be expressed in radiants. The Azimuth varies between $\pm 180°$, positive clockwise, starting from the South, as shown in Figure B.1 for a latitude of 25°.

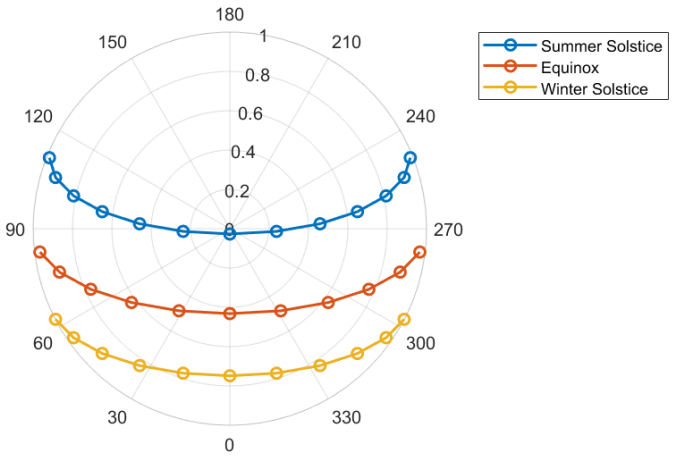

Figure B.1: Sun position polar plot for four intermediate annual angles. Latitude equal to 25°.

Where w express the hour angle, so the angular displacement of the sun from the local meridian due to rotation of the earth and it's equal to 15° every solar hour.
δ is the declination angle, namely the angular position of the sun at solar noon with respect to the equator [18].
The solar vector $\vec{\mathbf{s}}$ in a XYZ plane with X pointing East, Y to North and Z to the Zenith, can the be evaluated as Equation B.2.

$$\vec{\mathbf{s}} = (-\cos El \ \sin Az, \ \cos El \ \cos Az, \ -\sin El) \tag{B.2}$$

List of Figures

List of Tables